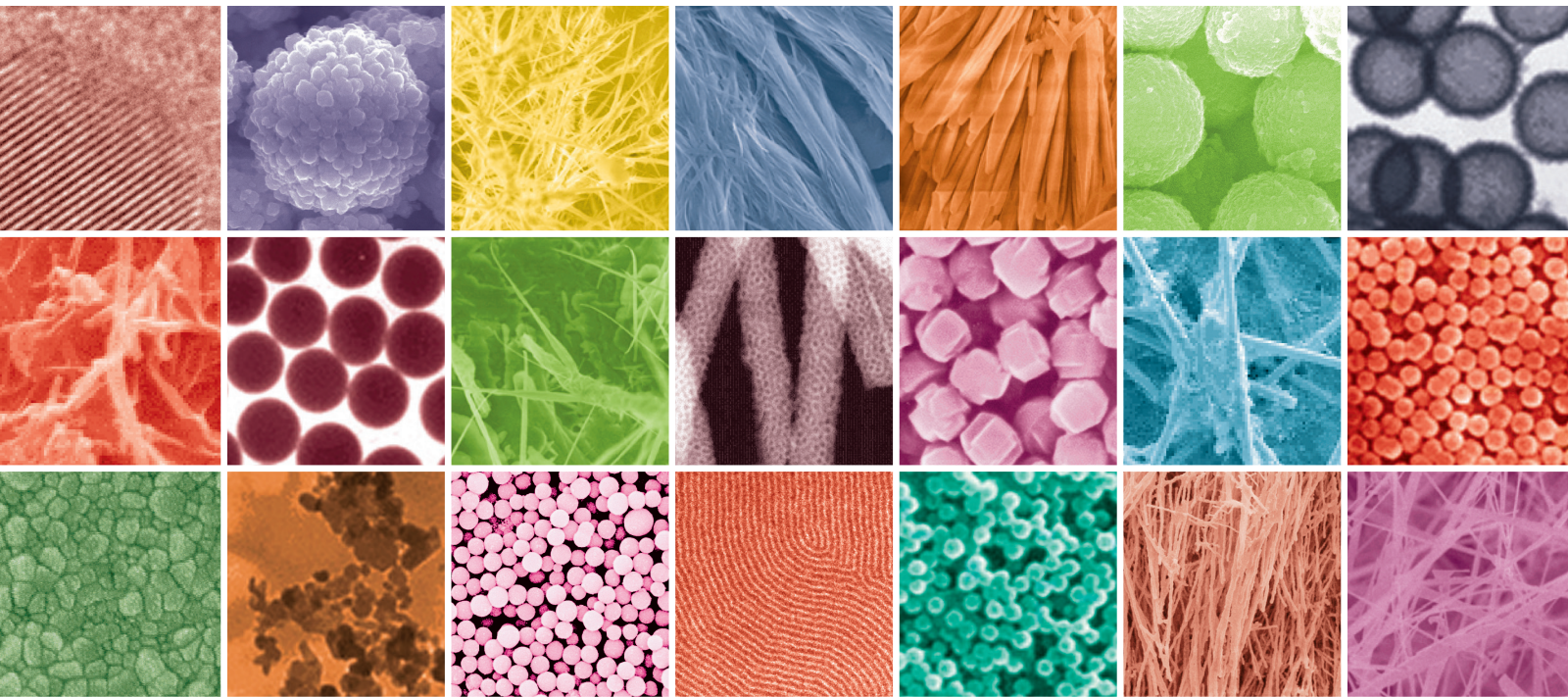


Plasmonics and Nanophotonics

Guest Editors: Tong Zhang, Xuefeng Liu, Qin Chen, Jing Chen,
and Haider Butt





Plasmonics and Nanophotonics

Journal of Nanomaterials

Plasmonics and Nanophotonics

Guest Editors: Tong Zhang, Xuefeng Liu, Qin Chen, Jing Chen,
and Haider Butt



Copyright © 2014 Hindawi Publishing Corporation. All rights reserved.

This is a special issue published in "Journal of Nanomaterials." All articles are open access articles distributed under the Creative Commons Attribution License, which permits unrestricted use, distribution, and reproduction in any medium, provided the original work is properly cited.

Editorial Board

Katerina Aifantis, Greece
Nageh K. Allam, USA
Margarida Amaral, Portugal
Xuedong Bai, China
Enrico Bergamaschi, Italy
Theodorian Borca-Tasciuc, USA
C. Jeffrey Brinker, USA
Christian Brosseau, France
Xuebo Cao, China
Sang-Hee Cho, Republic of Korea
Shafiq Chowdhury, USA
Cui Chunxiang, China
Miguel A. Correa-Duarte, Spain
Shadi A. Dayeh, USA
Ali Eftekhari, USA
Claude Estournes, France
Alan Fuchs, USA
Lian Gao, China
Russell E. Gorga, USA
Hongchen Chen Gu, China
Mustafa O. Guler, Turkey
John Zhanhu Guo, USA
Smrati Gupta, Germany
Michael Harris, USA
Zhongkui Hong, USA
Michael Z. Hu, USA
David Hui, USA
Y.-K. Jeong, Republic of Korea
Sheng-Rui Jian, Taiwan
Wanqin Jin, China
Rakesh K. Joshi, India
Zhenhui Kang, China

Fathallah Karimzadeh, Iran
Do Kyung Kim, Republic of Korea
Kin Tak Lau, Australia
Burtrand Lee, USA
Benxia Li, China
Jun Li, Singapore
Shijun Liao, China
Gong Ru Lin, Taiwan
J.-Y. Liu, USA
Jun Liu, USA
Tianxi Liu, China
Songwei Lu, USA
Daniel Lu, China
Jue Lu, USA
Ed Ma, USA
Gaurav Mago, USA
Sanjay R. Mathur, Germany
Nobuhiro Matsushita, Japan
A. McCormick, USA
Vikas Mittal, UAE
Weihai Ni, Germany
Sherine Obare, USA
Edward Andrew Payzant, USA
Kui-Qing Peng, China
Anukorn Phuruangrat, Thailand
Ugur Serincan, Turkey
Huaiyu Shao, Japan
Donglu Shi, USA
Suprakas Sinha Ray, South Africa
Vladimir Sivakov, Germany
Marinella Striccoli, Italy
Bohua Sun, South Africa

Saikat Talapatra, USA
Nairong Tao, China
Titipun Thongtem, Thailand
Somchai Thongtem, Thailand
Valeri P. Tolstoy, Russia
Tsung-Yen Tsai, Taiwan
Takuya Tsuzuki, Australia
Raquel Verdejo, Spain
Mat U. Wahit, Malaysia
Shiren Wang, USA
Yong Wang, USA
Cheng Wang, China
Zhenbo Wang, China
Jinquan Wei, China
Ching Ping Wong, USA
Xingcai Wu, China
Guodong Xia, Hong Kong
Zhi Li Xiao, USA
Ping Xiao, UK
Shuangxi Xing, China
Yangchuan Xing, USA
N. Xu, China
Doron Yadlovker, Israel
Ying-Kui Yang, China
Khaled Youssef, USA
Kui Yu, Canada
Haibo Zeng, China
Tianyou Zhai, Japan
Renyun Zhang, Sweden
Yanbao Zhao, China
Lianxi Zheng, Singapore
Chunyi Zhi, Japan

Contents

Plasmonics and Nanophotonics, Tong Zhang, Xuefeng Liu, Qin Chen, Jing Chen, and Haider Butt
Volume 2014, Article ID 746195, 1 page

Development and Application of Surface Plasmon Polaritons on Optical Amplification,
Tong Zhang and Feng Shan
Volume 2014, Article ID 495381, 16 pages

Transmissive/Reflective Structural Color Filters: Theory and Applications, Yan Yu, Long Wen,
Shichao Song, and Qin Chen
Volume 2014, Article ID 212637, 17 pages

Optical Amplification at 1525 nm in BaYF₅: 20% Yb³⁺, 2% Er³⁺ Nanocrystals Doped SU-8 Polymer Waveguide, Pengcheng Zhao, Meiling Zhang, Tianjiao Wang, Xinyang Liu, Xuesong Zhai, Guanshi Qin, Weiping Qin, Fei Wang, and Daming Zhang
Volume 2014, Article ID 153028, 6 pages

Applications of Silver Nanowires on Transparent Conducting Film and Electrode of Electrochemical Capacitor, Yuan-Jun Song, Jing Chen, Jing-Yuan Wu, and Tong Zhang
Volume 2014, Article ID 193201, 7 pages

Partial Polarization in Interfered Plasmon Fields, P. Martínez Vara, M. A. Torres Rodríguez, S. I. De Los Santos-Garcia, J. Muñoz López, and G. Martínez-Niconoff
Volume 2014, Article ID 602374, 5 pages

Large-Scale Synthesis of Silver Nanoparticles by Aqueous Reduction for Low-Temperature Sintering Bonding, Qiu Xiliang, Cao Yang, Lin Tiesong, He Peng, Wang Jun, Liu Ping, and Gu Xiaolong
Volume 2014, Article ID 594873, 8 pages

Variable Optical Attenuator Based on Long-Range Surface Plasmon Polariton Multimode Interference Coupler, Xiaoqiang Sun, Ying Xie, Tong Liu, Changming Chen, Fei Wang, and Daming Zhang
Volume 2014, Article ID 394976, 9 pages

Si₃N₄-SiC_p Composites Reinforced by *In Situ* Co-Catalyzed Generated Si₃N₄ Nanofibers, Juntong Huang, Zhaohui Huang, Shaowei Zhang, Minghao Fang, and Yan'gai Liu
Volume 2014, Article ID 752378, 6 pages

Editorial

Plasmonics and Nanophotonics

Tong Zhang,¹ Xuefeng Liu,² Qin Chen,³ Jing Chen,⁴ and Haider Butt⁵

¹ School of Electronic Science and Engineering, Southeast University, Nanjing 210096, China

² Research Institute of Nano-Resolution Optics, Nanjing University of Science and Technology, Nanjing 210094, China

³ Key Laboratory of Nanodevices and Applications, Suzhou Institute of Nano-Tech and Nano-Bionics, Chinese Academy of Sciences, Suzhou 215123, China

⁴ MOE Key Laboratory of Weak-Light Nonlinear Photonics, School of Physics, Nankai University, Tianjin 300071, China

⁵ School of Mechanical Engineering, University of Birmingham, Birmingham B15 2TT, UK

Correspondence should be addressed to Tong Zhang; tzhang@seu.edu.cn

Received 26 June 2014; Accepted 26 June 2014; Published 3 August 2014

Copyright © 2014 Tong Zhang et al. This is an open access article distributed under the Creative Commons Attribution License, which permits unrestricted use, distribution, and reproduction in any medium, provided the original work is properly cited.

Nanostructures have attracted considerable attention for many new fantastic applications owing to their remarkable physical properties. Most recent work has demonstrated that various material properties can be modified when the materials scale down to nanometers. Interacting with electromagnetic waves, nanomaterials show exciting and interesting phenomena such as subwavelength waveguiding and modulation, light tripping and filtering, and ultraresolution imaging. Although complete control of nanomaterial fabrication remains a challenge, various advanced techniques have been proposed to achieve sub-10 nm patterning. On this basis, desired radiation can be realized by manipulating the nanostructures. These nanostructures, especially the plasmonic nanostructures supporting surface plasmon polaritons, show great potentials in many application fields. For these reasons, this research field, especially plasmonics and nanophotonics, has been experiencing an explosive growth.

In this special issue, we have a series of contributed papers that are focusing on the recent development of the fundamental physics, fabrication, devices, and applications in the field of plasmonics and nanophotonics. First, T. Zhang and F. Shan reviewed the development and application of surface plasmon polaritons on optical amplification. Y. Yu et al. performed a literature survey on the recent advances in theory and applications of transmissive/reflective structural color filters. Then some of the research papers illustrated the research on the synthesis and application of nanostructures: Q. Xiliang et al. reported a successful large-scale

synthesis of silver nanoparticles by aqueous reduction for low-temperature sintering bonding; Y.-J. Song et al. demonstrated that silver nanowires can be applied to transparent conducting film and electrode of electrochemical capacitor; J. Huang et al. studied the Si_3N_4 -SiCp composites reinforced by in situ cocatalyzed generated Si_3N_4 nanofibers. In the meantime, some of the papers covered the optical waveguide and its functional device: P. Zhao et al. studied the $\text{BaYF}_5: 20\% \text{Yb}^{3+}, 2\% \text{Er}^{3+}$ nanocrystals doped SU-8 polymer waveguide and spotlighted its optical amplification at 1525 nm; X. Sun et al. demonstrated a variable optical attenuator based on long-range surface plasmon polariton multimode interference coupler. Finally, P. M. Vara et al. investigated the partial polarization in interfered plasmon fields.

Acknowledgments

The editors would like to thank all the authors for their contribution to the literatures on plasmonics and nanophotonics. We also thank the reviewers for their time and valuable comments in the peer review process of the manuscripts submitted to the issue.

Tong Zhang
Xuefeng Liu
Qin Chen
Jing Chen
Haider Butt

Review Article

Development and Application of Surface Plasmon Polaritons on Optical Amplification

Tong Zhang^{1,2} and Feng Shan^{1,2}

¹ School of Electronic Science and Engineering, Southeast University, Key Laboratory of Micro-Inertial Instrument and Advanced Navigation Technology, Ministry of Education, Nanjing, Jiangsu 210096, China

² Suzhou Key Laboratory of Metal Nano-Optoelectronic Technology, Suzhou Research Institute of Southeast University, Suzhou, Jiangsu 215123, China

Correspondence should be addressed to Tong Zhang; tzhang@seu.edu.cn

Received 28 February 2014; Accepted 15 May 2014; Published 24 July 2014

Academic Editor: Xuefeng Liu

Copyright © 2014 T. Zhang and F. Shan. This is an open access article distributed under the Creative Commons Attribution License, which permits unrestricted use, distribution, and reproduction in any medium, provided the original work is properly cited.

Propagation of surface plasmon polaritons (SPPs) along the interface between a metal and a dielectric has attracted significant attention due to its unique optical properties, which has inspired a plethora of fascinating applications in photonics and optoelectronics. However, SPPs suffer from large attenuation because of the ohmic losses in the metal layer. It has become the main bottom-neck problem for the development of high performance plasmonic devices. This limitation can be overcome by providing the material adjacent to the metal with optical gain. In this paper, a review of gain compensation to SPPs is presented. We focus on the spontaneous radiation amplification and simulated radiation amplification. The ohmic loss of metal was greatly improved by introducing optical gain. Then we introduce several gain mediums of dye doped, quantum dots, erbium ion, and semiconductor to compensate optical loss of SPPs. Using gain medium mentioned above can compensate losses and achieve many potential applications, for example, laser, amplifier, and LRSPP discussed.

1. Introduction

Surface plasmon polaritons (SPPs) are transverse magnetic (TM) polarized optical surface waves formed through the interaction of photons with free electrons at the surface of metals, typically at visible or infrared wavelengths [1]. This mode has fields that peak at the metal dielectric interfaces, decaying exponentially into the dielectric background. Various metallic structures have been investigated over time [2, 3], leading to potentially interesting applications across many fields including fields such as spectroscopy [4], nanophotonics [5], imaging [6], biosensing [7, 8], and circuitry [9]. In a large part, the rapidly growing interest in SPPs was driven by the eagerness to understand and control the behavior of light on the nanometer scale and enabled by the significant improvements in micro- and nanofabrication that have appeared in the past several decades. The presence of SPPs in metallic nanostructures linked with a variety of distinctive optical performances, such as extraordinary

light transmission, huge field enhancement, and negative refraction [4].

Although SPPs waveguides are of the inherent virtue of the subwavelength scale confinement, the propagation length is not long due to the ohmic loss in metals. One of the main limitations in using SPPs for device design is the intrinsic damping of SPPs arising from the loss in the metal. Interband transitions absorption can be reduced by careful selection of the operating wavelength and reducing free electron scattering by improving fabrication techniques; however, it cannot be eliminated completely [10].

SPPs practical applications are limited due to their exceeding loss. Many efforts [11–14] have been made to increase the transmission length and simultaneously assure the subwavelength confinement. Gain compensation approach is proposed by investigator to add optical gain. The compensation of SPPs establishes the foundation for lots of amusing and helpful applications, which has motivated much of the study on it.

The characters of SPPs supported by all kinds of metallic structures are notably different from their traditional counterparts in form and character. Following the introduction, the remainder of this paper is structured as follows: Section 2 will describe two aspects of compensation way, fluorescence enhancement and laser amplification. In Section 3, the gain mediums including dyes, quantum dots (QDs), Er ions, and semiconductors are discussed. A range of emerging applications of gain SPPs are discussed in Section 4. Finally, in Section 5 conclusions are provided.

2. The Ways of SPPs Gain Compensation

As the significance of loss has become more important to the SPPs, a multispect effort to mitigate loss has been studied. One can readily classify the variety of approaches to deal with the losses into several categories. The first one is to engineer the shape and size of plasmonic structures with the goal of reducing the fraction of energy confined inside the metal leading to the decrease of the loss. The second one is to choose suitable noble materials such as highly doped semiconductors, intermetallics, and graphene. The third one is to introduce optical gain into the plasmonic structure to compensate the loss. The optical gain, however, not only can compensate the loss, but also can realize amplification. In this section, two kinds of optical amplification mechanisms of SPPs including spontaneous radiation and simulated radiation are discussed.

2.1. Spontaneous Radiation Amplification. In the past decades, many efforts have been devoted to spontaneous radiation-based study [15] with advanced sensitivity by using plasmon enhanced fluorescence [16–18]. In SPPs coupled fluorescence emission, fluorescence emitted by gain medium via SPPs is studied. The outcoupling of fluorescence that is trapped in SPPs to radiation is reported [19–21] to provide efficient means for SPPs signal enhancement.

Sudarkin and Demkovich [22] first reported the SPPs gain compensation of fluorescence enhancement, whose structure contained a silver film sandwiched between a glass prism and a gain medium. Then a similar structure over a wider range of parameters was investigated by Poltz et al. [23]. Recently, increasing efforts have been devoted to the compensation for the SPPs fluorescence enhancement by using gain media to achieve loss compensation [24–30]. Noginov et al. [31] have studied SPPs excited by emission of optically pumped R6G molecules and by direct scattering of pumping light in a polymeric film in the attenuated total reflection setup. As shown in Figure 1, SPPs are confined to the proximity of metal dielectric interface and decay exponentially in both media. In the experiments, increasing the pumping intensity, the character of the SPPs emission excited via optically pumped dye molecules has changed dramatically. The emission spectra considerably narrowed in comparison to those at low pumping.

Besides, SPPs propagation with net positive gain over microscopic distances directs proof by Gather et al. [32]. The schematic illustration of the long range surface plasmon

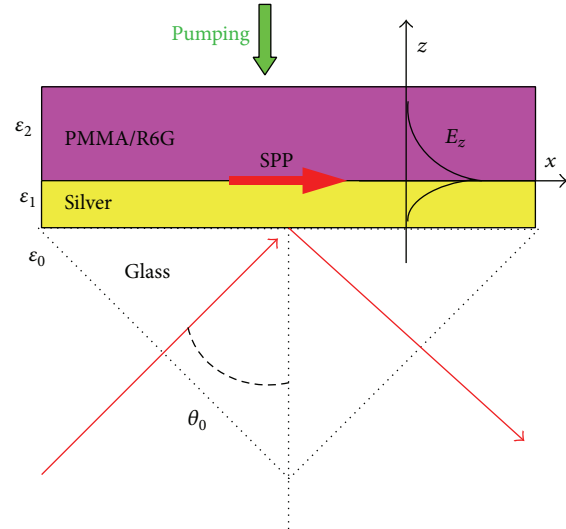


FIGURE 1: Schematic of experimental sample.

polariton (LRSPP) waveguides is shown in Figure 2(a). The device is composed of a Si substrate layer over a 20 nm thick transparent polymer layer with a refractive index of 1.55 and an Au layer with the thickness of 4 nm. A gain material layer with 1 nm thickness and an additional 20 nm thick transparent polymer layer complete the structure. The end-fire coupled light to the LRSPP mode of waveguides using a low numerical aperture optical fiber to measure the propagation loss of the waveguide at the relevant wavelengths and image the decay of the scattered light intensity along the direction of the light propagation. A waveguide which did not include the gain material layer was measured first. As can be seen from Figure 2(b), the losses at wavelengths higher than 600 nm are below the gain that can be obtained with PPV in this region of the spectrum. However, the propagation loss increases speedily at shorter wavelengths because of the Au surface plasmon resonance. The propagation losses are mostly ascribed to absorption and scattering in the metal film. Propagation loss measurements for waveguides containing a layer of gain material were also discussed in Figure 2(b).

The foregoing researches have discussed SPPs gain on the basis of fluorescence enhancement of gain medium stimulated emission. These works paved the way toward the development of kinds of devices exploiting SPPs amplification. Gain medium excitation provides larger enhancement of the fluorescence excitation and thus allows for a stronger increase in the SPPs signal. Due to the introduction of spontaneous radiation to SPPs, lots of potential applications were developed.

2.2. Simulated Radiation Amplification. Aside from spontaneous radiation amplification, simulated radiation amplification is also used to compensate the SPPs loss, which emerges during the propagation. SPPs are capable of closely localizing light, but up to now ohmic losses at optical frequencies have impeded the realization of nanometer scale lasers [10, 33].

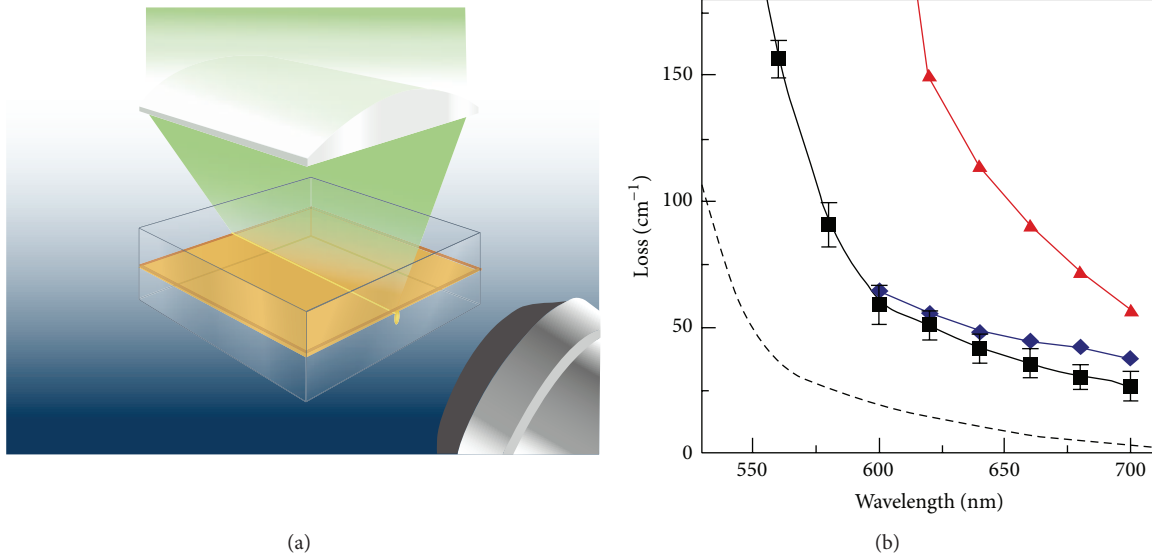


FIGURE 2: (a) Schematic of LRSPP waveguides containing a fluorescent polymer blend to provide optical gain and illustration of the gain measurement configuration; (b) Measurement and optimization of the propagation loss in 4 nm thick gold LRSPP waveguides. Propagation loss for different plasmonic waveguides as a function of wavelength for a structure without gain material (black squares), with a gain layer that was partly index matched (red triangles, nominal $\Delta n = 0.03$) and fully index matched (blue diamonds). Error bars represent uncertainty of the fit to the exponential decay and are representative for all data sets. The dashed line represents a theoretical loss estimate (neglecting scattering) for the structure without gain material.

Through amplifying the radiation by simulated emission, SPPs signal amplification can be achieved. The resonant cavity is used to stimulate more light emission with the same phase by reflecting the light back and forth in metal nanostructures in order to generate the initial SPPs around the nanoscale metal dielectric interface. Oulton et al. [34] first theoretically foretold that such losses could be deeply reduced while maintaining ultrasmall modes in a hybrid plasmonic waveguide. Based on this, Oulton et al. [33] reported the experimental demonstration of nanometer scale plasmonic lasers, generating optical modes a hundred times smaller than the diffraction limit. The coupling between the plasmonic and waveguide modes across the gap enables energy storage in nonmetallic regions. This structure allows SPPs to travel over larger distances with strong mode confinement. Lately, many works focusing on optoelectronic devices and circuits constructed by resonance cavities for SPPs enhancement were studied [35, 36]. One of the cavities for nanowires (NWs) offered great surface smoothness and crystalline structures, which guaranteed low waveguiding losses for plasmonic [37, 38] mode.

The loss compensation ability of the hybrid plasmonic waveguide which is composed of a CdSe nanobelt (NB) kept from a silver surface by an Al_2O_3 layer was investigated experimentally by Liu et al. [39]. An optical pump probe technique was used to probe signals and the ultrahigh optical gain with gain coefficient exceeding 6755 cm^{-1} was achieved. The important thing is that the loss compensation works in the comparatively wide spectral band regime and requires nanolasing operating at single mode. It can be seen from [39] that all wavelengths in the probe signal are equally

amplified through the stimulated emission, demonstrating the broadband performance of the loss compensation subject. Internal gain measurements as a function of the pump intensity for probe signals show obvious loss compensation, achieving maximum gain of 8.8 dB.

Wu et al. [40] reported a NWs laser that offers subdiffraction limited beam size and spatially separated plasmon cavity modes. The scheme is illustrated in Figure 3(a). An Ag NW is side coupled to a CdSe NW to form an X-shaped structure (Figure 3(c)). The lasing action is investigated under 532 nm wavelength laser pulses (5 ns pulse width, 2 kHz repetition rate). They mainly focused on the left segment of the CdSe NW (Figure 3(b)) and the emission scattered from each end-facet was collected by the selected area spectral measurement system. By near field coupling a long CdSe NW and a 100 nm diameter Ag NW, they demonstrate a hybrid photon plasmon NW laser that offers subdiffraction limited beam size and spatially separated plasmon modes. The laser operates around 723 nm wavelength at room temperature and offers far field accessible pure plasmon cavity modes on a $3.7 \mu\text{m}$ long Ag NW with a beam size of $0.008 \lambda^2$. They also show that the hybrid photon plasmon NW laser can be modulated by solely modifying the propagation loss of the plasmon modes in the Ag NW. When the pumping fluence increases from 27 to $97 \mu\text{J cm}^{-2}$, the emission output experiences a lasing spectrum shown in Figure 3(d).

Semiconductor nanostructures have major potential to be used as a critical component in compact optical devices at the nanoscale. The Fabry-Perot type of SPPs of laser amplification by nanostructure has been realized. It provides a lot of chances for the assembly of nanoscale electronic and

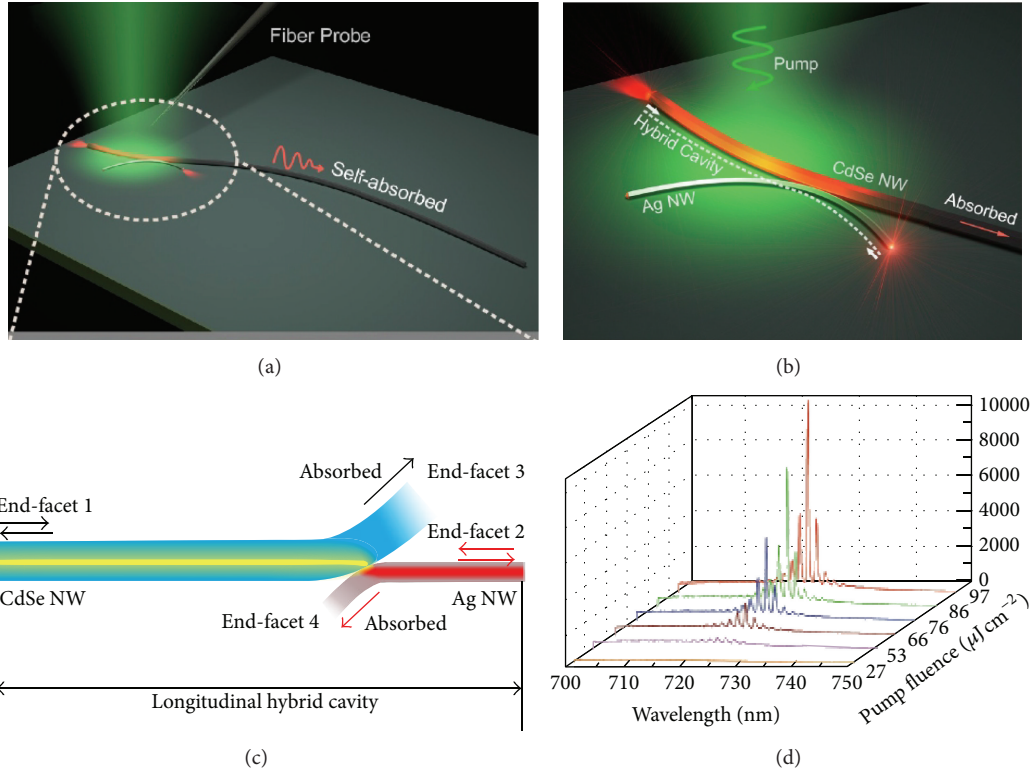


FIGURE 3: Schematic illustration of a hybrid photon-plasmon NW laser. (a) The hybrid photon-plasmon NW laser is composed of an Ag NW and an ultralong CdSe NW coupled into X-shape using a fiber probe for micromanipulation. The right segment of CdSe NW serves as a distributed absorber without reflection. (b) Closed-up view of the coupling area indicating the coupled hybrid cavity (marked by the dashed line), which serves as the hybrid photon-plasmon lasing cavity. (c) Cavity formation in the X-structure. (d) Lasing spectra collected from the Ag end-facet under pump fluences of 27–97 $\mu\text{J cm}^{-2}$.

optoelectronic devices. What is more, these nanostructures demonstrate new and enhanced features crucial to several fields of technology.

3. Type of Gain Material

One of the attractive characters of plasmonic waveguides is their capacity to confine light lower than the traditional diffraction limit. However, the increase of mode confinement usually comes at the price of large propagation loss. SPPs propagating between metal and dielectric interface sustain propagation losses over several hundred cm^{-1} at visible wavelengths. The decrease of optical loss is of rather importance in metallic structures depending on surface plasma waves, for example, transmitting electromagnetic energy [2], realizing negative refraction [41]. Despite many improvements that can be achieved by means of the optimization of the geometry and materials and by reducing structural defectives, the optical losses are caused by the physical performances of the metal and can only be dealt with by introducing optical gain into the structure [22]. Adopting this project, a reduction in the loss of propagating plasmons using dye doped [32, 42], QDs [43, 44], Er ions [45, 46], or semiconductor [47] has been reported recently.

Generally, dyes are emitted in the visible and low ($<1 \mu\text{m}$) near infrared spectral range and have broad emission lines.

The development of stimulated radiation at wavelengths above $1 \mu\text{m}$ is still a challenge due to the fact that polymer hosts usually suffer from absorption by vibrations of the C–H bond in the near infrared wavelength region. The QDs nanostructures with the radius in the range from 1 to 10 nm are synthesized by colloidal chemistry. In this case, the emission wavelength can be easily tuned by controlling the material of the dots and their sizes. They can be easily embedded in polymer matrices using a common solvent. Compared to the other two gain media discussed above, Er ion doped polymers have the advantages of emitting in the corresponding spectral ranges as well as producing emission within the 1310 nm and 1550 nm windows, which are important for telecommunication applications. Although several studies have applied gain medium to compensate for the optical loss of strongly confined SPPs, semiconductors tend to be the choice of materials for losses in excess of 1000 cm^{-1} . At infrared wavelengths, the loss of maximally confined hybrid SPPs is on the order of 1000 cm^{-1} , which is well within the gain range of a variety of common compound semiconductors. However, strong gain effects, such as gain guiding, could provide additional design freedoms for future devices.

3.1. Dyes. The coupling of fluorescence of dye with SPPs was subject to investigation [24, 30], and recently it found

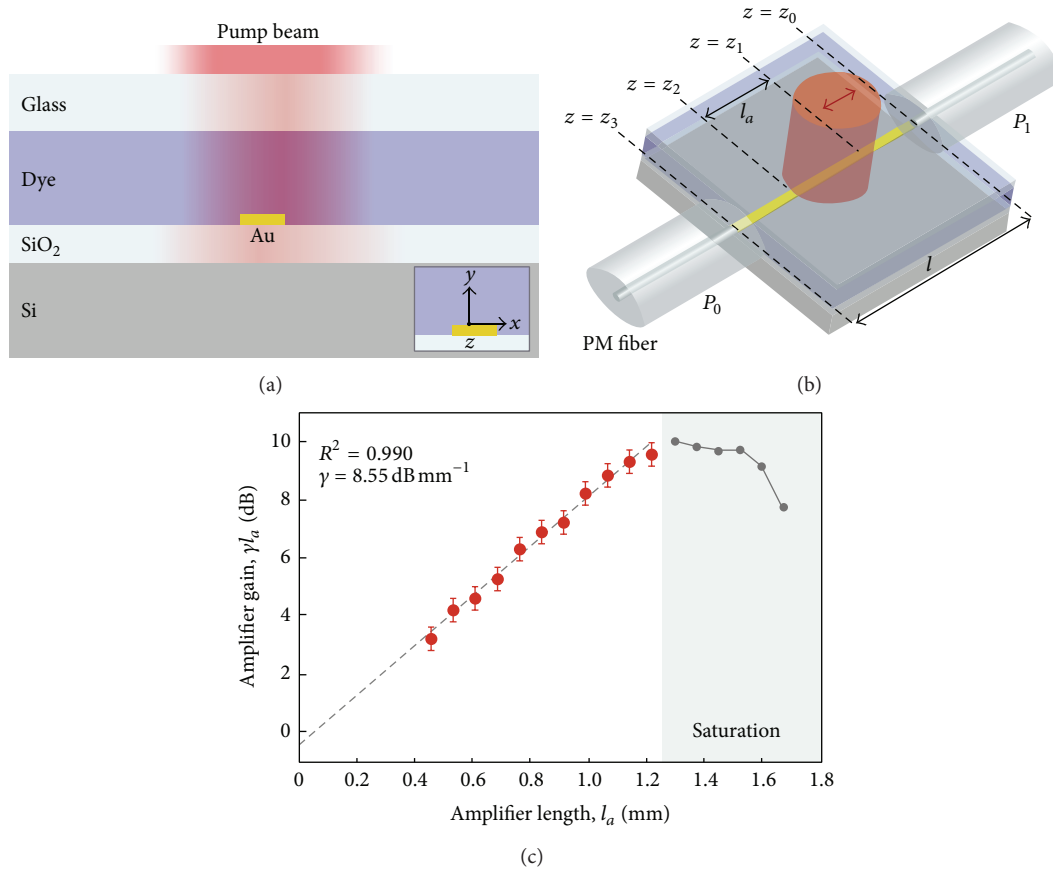


FIGURE 4: (a) Cross-sectional view of active structure. The gain medium is in the form of a laser dye in solution. Inset: coordinate system with the z -direction coming out of the page. (b) Pump and probe signal coupling arrangements used for amplification experiments. Pump polarization, indicated by the red arrow, is parallel to the waveguide length (z -axis). A probe signal is coupled in and out of the structure by means of end-fire coupling using polarization-maintaining (PM) fibers. (c) Measurements of amplifier gain versus amplifier length. A linear fit to the unsaturated data yields an LRSPP mode power gain of $\gamma = 20 \text{ dB cm}^{-1}$.

applications in fields such as plasmonic lasers [25] and surface plasmon enhanced fluorescence spectroscopy biosensors [26]. Fluorescence trapped in SPPs to far field radiation by adopting various methods [19–21] was reported to provide efficient means for collecting of enhanced SPPs signal. Dye has been considered as gain media for SPPs structure as proposed by Plotz et al. [23] in 1979 and has subsequently been reported by others. Avrutsky [48] demonstrated that dyes as a medium with strong gain are able to increase propagation length in silver films. Seidel et al. [49] experimentally demonstrated optically pumping a dye solution and using a prism coupling method by stimulated emission at 633 nm of SPPs in silver films. In recent works, the dielectric gain material consisted of dyes embedded into a polymer. Such a multicomponent material has the advantages of joining the active performances of the dyes with the technological feasibility of polymers. So de Leon and Berini [42] suggested a silver planar film surrounded by CYTOP and Rhodamine has been studied, demonstrating theoretically that for high enough powers and dye concentration amplification in the visible range is possible. The same dye dispersed in PMMA was investigated as a medium able to provide gain equal to

420 cm^{-1} invested by Noginov et al. [31]. In these conditions, using the attenuated total reflection setup can compensate the losses of a silver film at 594 nm by nanocomposite. Then, the same authors [50] used a similar system to demonstrate stimulated emission of SPPs in the polymer film. Recently, Gather et al. [32] chose a fluorescent polymer made by the dispersion of PFS in MDMO-PPV obtaining a net optical gain of 8 cm^{-1} at 600 nm in the SPPs. de Leon and Berini [25] first provided direct measurement of gain in propagating SPPs using the LRSPP supported by a symmetric metal stripe waveguide that incorporated optically pumped dye molecules as the gain medium. A cross-sectional view of the waveguide structure is shown in Figure 4(a). The gold stripe, which was 20 nm thick and 1 mm wide, lay on a 15 nm thick SiO_2 layer thermally grown on a silicon substrate and covered by a gain layer 100 nm thick consisting of optically pumped IR140 dye molecules. The dye was pumped at $\lambda_p = 808 \text{ nm}$ and the LRSPP was probed at $\lambda_e = 882 \text{ nm}$ close to the peak absorption and emission of the dye, respectively. The arrangement used for pumping and probing is depicted in Figure 4(c). The pump light was normally incident onto the top side of the structure linearly polarized along the

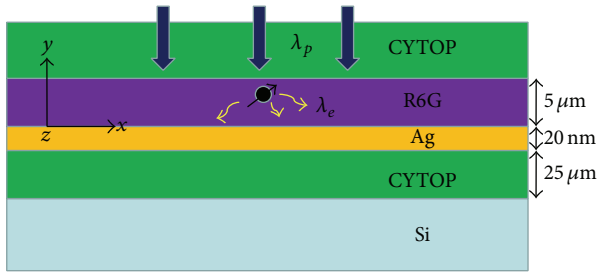


FIGURE 5: The SPP waveguide structure considered in the work.

z -axis (8 ns FWHM pulses, repetition rate of 10 Hz). Gain measurements were obtained as a function of the amplifier length l_a , as shown in Figure 4(c), from which the slope yields an LRSPP mode power gain of $\gamma = 20 \text{ dB cm}^{-1}$.

The same workers [42] considered another structure shown in Figure 5. It is made up with a silver film of 20 nm thick extending infinitely over the xz -plane. A lossless 25 μm thick dielectric CYTOP constitutes bottom cladding, sitting on a semi-infinite silicon substrate. The top surface is covered by R6G dye molecules in a mixture of ethanol and methanol. The dye solution is covered by a 5 μm thick semi-infinite CYTOP. A monochromatic pump signal of wavelength $\lambda_p = 532 \text{ nm}$ (near the peak absorption of R6G) is excited from the top of dye molecules. SPPs mode amplification is studied with the peak emission wavelength $\lambda_e = 560 \text{ nm}$ of the dye. The silver film in the vicinity normalized to the irradiance $I_p(y)$ of the incoming pump signal. The vertical dashed lines outline the silver film. The lower cladding thickness was used to reduce the resonant coupling to the slab mode. Owing to field reflection throughout the structure the irradiance follows a standing wave pattern in the dye. The population inversion is enhanced in those regions, achieving 2.5-fold maxima.

In general, the emission wavelength reported for dyes doped polymer is lower than 1000 nm, which falls within the telecommunication window. Dyes molecules as gain medium exciting the SPPs on the metal surface were presented as a mean of achieving SPPs compensation. A higher gain medium would be required because ohmic losses in metal at visible wavelengths are much greater than those at infrared wavelengths. Fluorescence emitted by dyes medium near the metallic surface couples with the SPPs. This process is efficient and collects emission with optical elements. The coupling between fluorescence emission of dyes and SPPs will have a broad range of applications.

3.2. QDs. SPPs ohmic losses in metallic nanostructure are the primary obstruction in acquiring excellent optical performance for photonic applications. Some measures have been proposed to polish up these losses including adopting gain media and parametric processes [51–59]. For dye gain media, Chénais and Forget [60] reported net modal gains achieve 100 cm^{-1} in slab waveguide geometries in the visible range. Substantially greater material gain is usually referred to the QDs. For example, values up to $\approx 10^5 \text{ cm}^{-1}$ have been reported for saturation material gain in 1.3 μm

emitting InGaAs QDs [61]. Compared with other organic dyes, QDs display more excellent photochemical stability in fluorescence applications. The surface modified QDs exhibit outstanding dispersibility in water, saline buffers, and in various pH conditions for more than 7 months. Moreover, the emission wavelength can be easily tuned by controlling the size or the base material. In this way optical amplification has already been demonstrated in dielectric waveguides with the QDs dispersed in it [62]. Besides, Surez et al. [63] mixed CdSe and CdTe QDs in PMMA, and the optimum conditions for waveguiding were obtained. Indeed, amplification of SPP using QDs PMMA nanocomposites has already been studied [43, 64]. PbS QDs are proposed as a method to provide gain in a dielectric load SPPs waveguide [64]. This structure consists of a dielectric strip deposited on a metal film, being possible to improve waveguiding characteristics by choosing parameters reasonably [14]. Then, a 32% compensation of SPP was demonstrated under the similar structure working at 876 nm [43]. Garcia et al. [44] obtained a 33% loss reduction in a dielectric loaded SPPs waveguide corresponding to 143 cm^{-1} of optical gain, using QDs doped PMMA ridges.

Bolger et al. [65] reported PMMA films of below 1 μm thickness were spin coated onto the Au structures (Figure 6(a)). The polymer films were doped with PbS QDs and used as an amplifying medium. A 633 nm He-Ne laser (3 mW) was directed at the incoupling grating (G1) and excited the QDs photoluminescence at around 1160 nm that is coupled to the SPPs at the Au/polymer interface. According to the SPP intensity dependencies on the pump power for several sets of the in/outcoupling gratings with different distances between them, the dependence of the signal SPPs propagation length on the pump intensity can be reconstructed (Figure 6(b)). The propagation length increases at low pump intensities reaching the maximum of approximately a 30% increase at about 1 W/cm^2 .

Grandidier et al. [64] investigated propagation assisted by stimulated emission in a polymer strip loaded plasmonic waveguide doped with QDs. They achieve 27% increase of the propagation length at telecom wavelength corresponding to a 160 cm^{-1} optical gain coefficient. PbS QDs were inserted in a PMMA polymer strip waveguide fabricated on $40 \pm 3 \text{ nm}$ thick gold films (Figure 7(a)). Figure 7(c) shows the QDs spontaneous emission intensity versus pump power. As expected from spontaneous decay, this signal linearly increases with pump power.

Radko et al. [43] investigated a four-layer structure composed of a quartz substrate, a 50 nm thick gold film, a thin layer of PMMA which embedded PbS QDs, and air (Figure 8(a)). They demonstrated an optical gain of $\sim 200 \text{ cm}^{-1}$ for the mode under consideration, which corresponds to $\sim 32\%$ compensation of SPP loss. PbS QDs exhibited a fluorescence emission peak at 876 nm and were pumped at 532 nm with a continuous waveform laser beam focused on a spot with diameter $d \sim 13.8 \mu\text{m}$ (Figure 8(b)).

It is hoped that SPPs propagation lengths can be greatly increased with the gain medium which provide optical gain. To this end, a gain medium composed of polymer and QDs compound is presented with the aim of proposing a

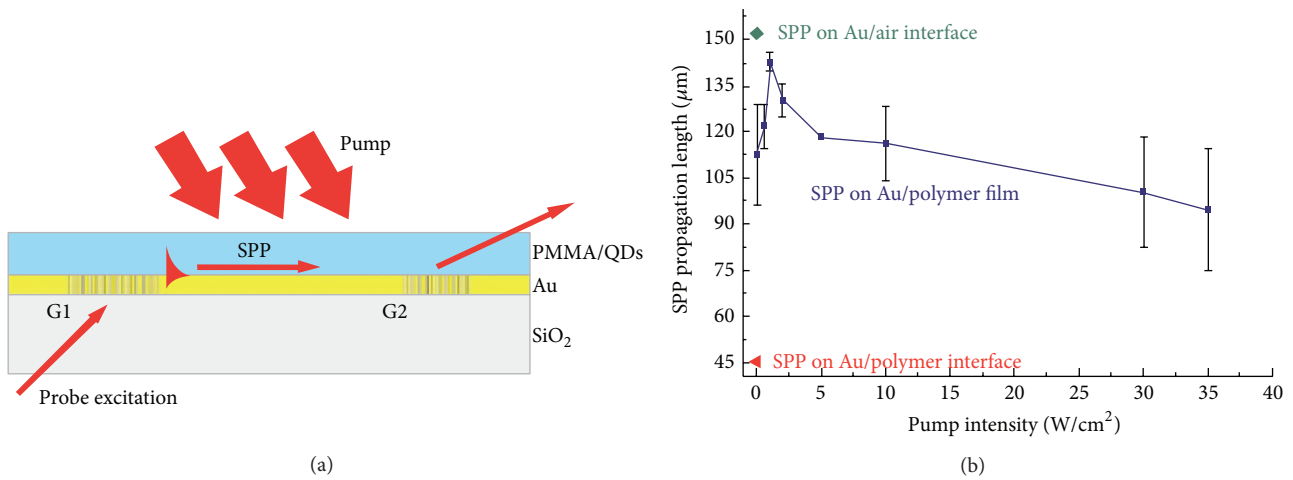


FIGURE 6: (a) Experimental setup for the optical measurements: a He-Ne laser light is coupled to SPPs on the G1 grating and excites signal SPPs via QD fluorescence. The amplifying medium is continuously pumped with a second He-Ne laser. The signal from the decoupling grating (G2) is collected into an optical fiber connected to the spectrometer. (b) The dependence of the propagation length of the signal SPPs on the pump intensity. The SPP propagation lengths on Au/semi-infinite polymer and Au/air interfaces are also shown.

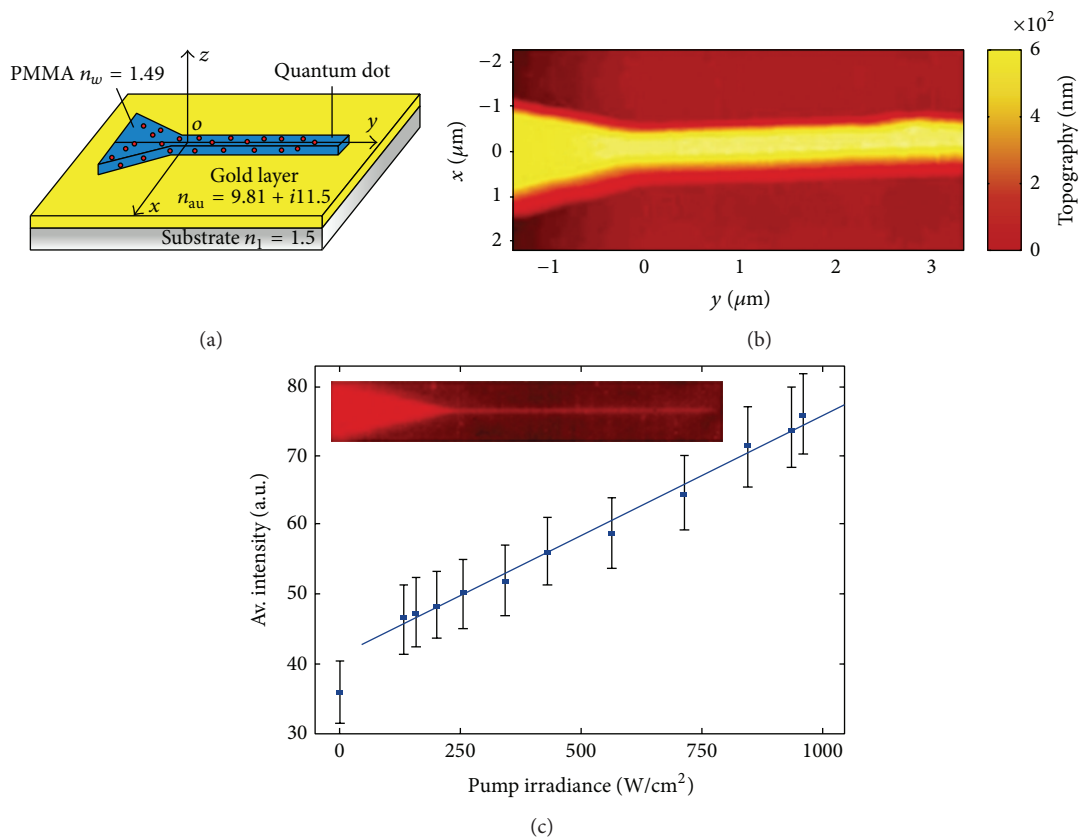


FIGURE 7: (a) Device configuration: a PMMA strip confines the plasmon at the gold/polymer interface. An additional tapering structure is designed to efficiently excite the SPP guided mode with an external infrared laser. The effective indices used in the numerical simulations are indicated on the figure. (b) Atomic force microscopy image of the DLSPW. The dimensions of the waveguide are 600 nm height, 400 nm width, and 65 μm length. (c) Averaged spontaneous emission intensity for increasing pump powers (dots, standard deviation indicated) with a linear regression (blue line). The inset shows a homogeneous emission inside the waveguide since an extended illumination was used.

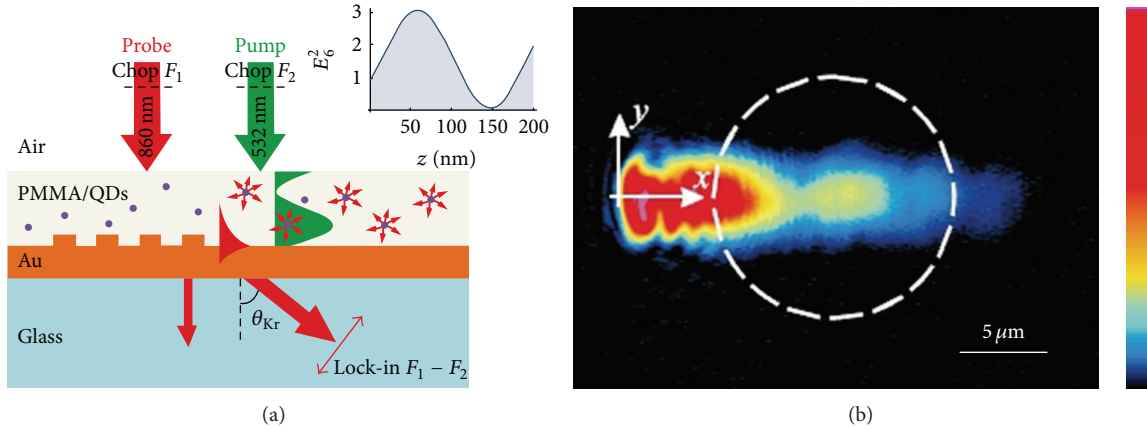


FIGURE 8: (a) Experimental configuration: thin PMMA film doped with PbS QDs on top of a 50 nm thick gold film. Excitation of a probe SPP beam ($\lambda = 860$ nm) is achieved through a grating. Inset shows a calculated distribution of the intensity of the pump beam ($\lambda = 532$ nm) inside the PMMA layer. (b) Leakage-radiation microscopy image of a probe SPP beam. The dashed circle shows the position where the pump beam is focused.

technologically feasible material which can tune the amplified wavelength by altering the nanostructure. Hence, wavelength tunability of the stimulated radiation (400 nm~2 μ m) can be achieved by changing the material and the size of the QDs.

3.3. Erbium Ion. Rare earth elements have potential optoelectronic applications due to their performance of photoluminescence and electroluminescence embedded in a solid state matrix [66]. Visible emissions of the Er ions in wide band gap semiconductors were intensively investigated. Er ions played an important role in optical communication systems operating at 1500 nm. At a certain temperature the Er emission spectrum was fixed for a given material because of the absorption and emission spectra of Er determined by Boltzmann distributions [67]. Many applications of materials doped Er ions depend mainly on the exact line shape of the emission. It would be very interesting if the Er emission spectrum could be externally modified. Previously, the energy transfer between the Er ions and the SPPs at the interface of metal and silica had been demonstrated by Kalkman et al. [46]. He also reported that emission spectra close to optical communication wavelength could be modified by grating structures due to SPPs reradiated into far field [67]. Then, Wang and Zhou [68] proposed a double grating configuration that greatly strengthened the emission of Er ions. The emission efficiency of the Er ions at 1550 nm increased more than ten times than other emission wavelengths within the 1500 nm communication windows, since the maximum density of the states of the SPPs was localized at the edge of the band edges [69–71]. Wang also proposed a silicon optical amplifier based on SPPs enhancement. The gain coefficient of the Si: SiEr-metal-silicon structure increased 24% at 1540 nm and the loss sharply reduced compared with a conventional stack structure [72]. In addition, the luminescence intensity of Er ions can be enhanced, when they are localized or close to nanoparticles (NPs), which is termed as SPPs enhanced luminescence [17, 73]. Christensen et al. [74] demonstrated the upconversion luminescence of Er ions doped materials in

the $\text{TiO}_2:\text{Er}^{3+}$ system when Au NPs were in close vicinity to the Er ions.

Verhagen et al. [75] studied the field enhancement and found that it was ascribed to the excitation of both propagating and localized surface plasmon resonances in arrays of square and annular apertures in an Au film. The measurement geometry was schematically depicted in Figure 9(a). The Er ions can convert infrared radiation with a free space wavelength of 1480 nm to emission at shorter wavelengths through an upconversion process. A level diagram of the 4f energy levels in Er^{3+} was shown in Figure 9(b).

Ambati et al. [45] reported a direct experimental evidence of stimulated emission of SPPs at telecom wavelengths (1532 nm) with Er doped by glass as a gain medium. They observed an increase in the propagation length of signal SPPs when Er ions were excited optically using pump SPPs. The experimental setup was developed to accommodate the optical pumping of Er doped with glass by using LRSP mode guided by the same metal strip shown in Figure 10(a). A laser diode with nominal wavelength of 1480 nm was used as the pump and a different laser diode at 1532 nm signal was used as the signal. However, in continuous wave mode, a maximum signal enhancement of ~50% (1.73 dB) was recorded at a higher pump power of 266 mW (Figure 10(b)).

Lots of researchers studied that the Er ions were excited in wide band gap semiconductors because Er ions played an important role in optical communication system operating at 1500 nm. In addition, at a certain temperature the Er emission spectrum was fixed for a given material because of the absorption and emission spectra of Er determined by Boltzmann distributions. As a result, there was a significant promise of the SPPs-assisted Er ions light emission.

3.4. Semiconductor. Due to the outstanding properties, resonance cavities with semiconductor as optics compensation have attracted growing interests in constructing nanoscale photonic and optoelectronic devices and circuits [35, 36]. Generally, a semiconductor cavity with the round trip gain,

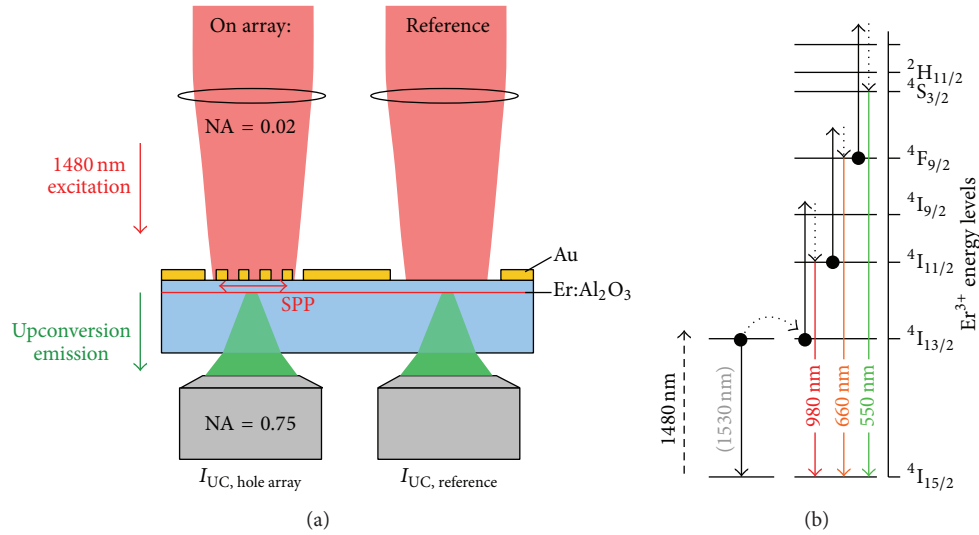


FIGURE 9: (a) Schematic depiction of the measurement geometry. The sample is illuminated with 1480 nm pump light, and upconversion luminescence from Er ions implanted in the sapphire substrate is collected through the substrate. (b) Er^{3+} 4f level diagram indicating the upconversion mechanism that leads to the population of Er^{3+} levels emitting at wavelengths of 980, 660, and 550 nm under 1480 nm excitation.

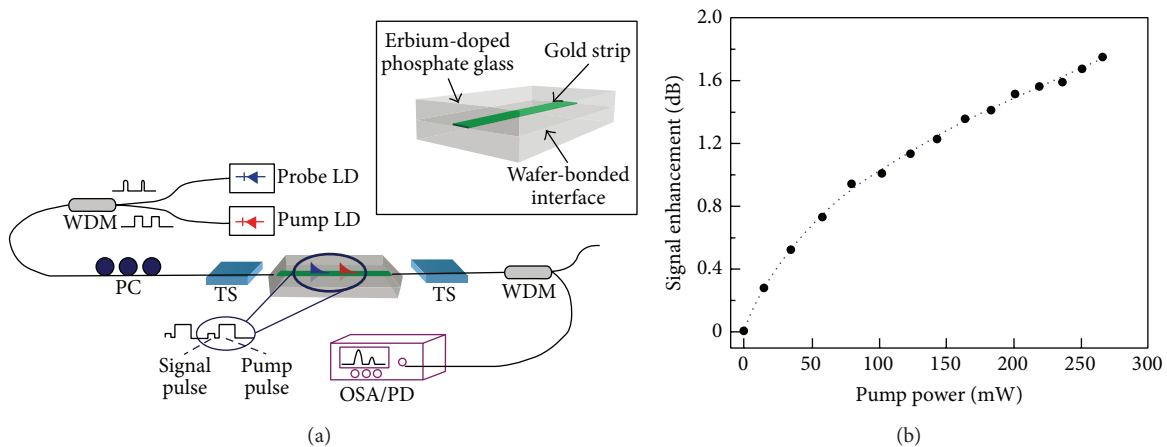


FIGURE 10: (a) Experimental configuration for inducing stimulated emission of SPPs, (b) enhancement of the signal as a function of pump power in continuous mode.

sustained by a certain feedback such as end-face reflection, can compensate round trip losses. Typically, the semiconductor cavity of this kind was formed by end-face reflection [76–79] or ring resonance [80, 81]. Hill et al. [82] introduced a metalized, etched semiconductor heterostructure as shown in Figure 11(a). SPPs between the two metal planes were weakly confined by a small index variation along the heterostructure's growth direction leading to that guided wave propagation paralleled to the plane of the substrate. The thinnest heterostructure reported in this work was just 90 nm thick resulting in SPPs smaller than the diffraction limit in one dimension. A Fabry-Perot SPPs resonator consisted of the end-facets of the metalized structure.

Another device reported by Oulton and coworkers [33] also used a Fabry-Perot cavity, but with plasmonic confinement in two dimensions perpendicular to wave propagation.

The laser cavity consists of a semiconductor nanowire put on a flat metal film with a thin nanoscale insulating gap, as shown in Figure 12(b). Remarkably, the mode of the NW and the SPPs of the metal surface hybridized into a deep subwavelength mode propagating along the wire's axis. Here, a small amount of feedback was provided by the end-facets of the NW forming a cavity.

Ma et al. [83] reported another kind of semiconductor cavity operating at room temperature with $\lambda/20$ optical confinement (Figure 13). A 45 nm thick CdS nanosquare atop a silver surface separated by a 5 nm thick magnesium fluoride gap layer provided the subdiffraction limited mode confinement and low metal loss. Surprisingly, although the high index material is only 45 nm thick, the SPPs of this system carry high momentum even higher than light waves in bulk CdS or plasmonic NW lasers. This leads to strong

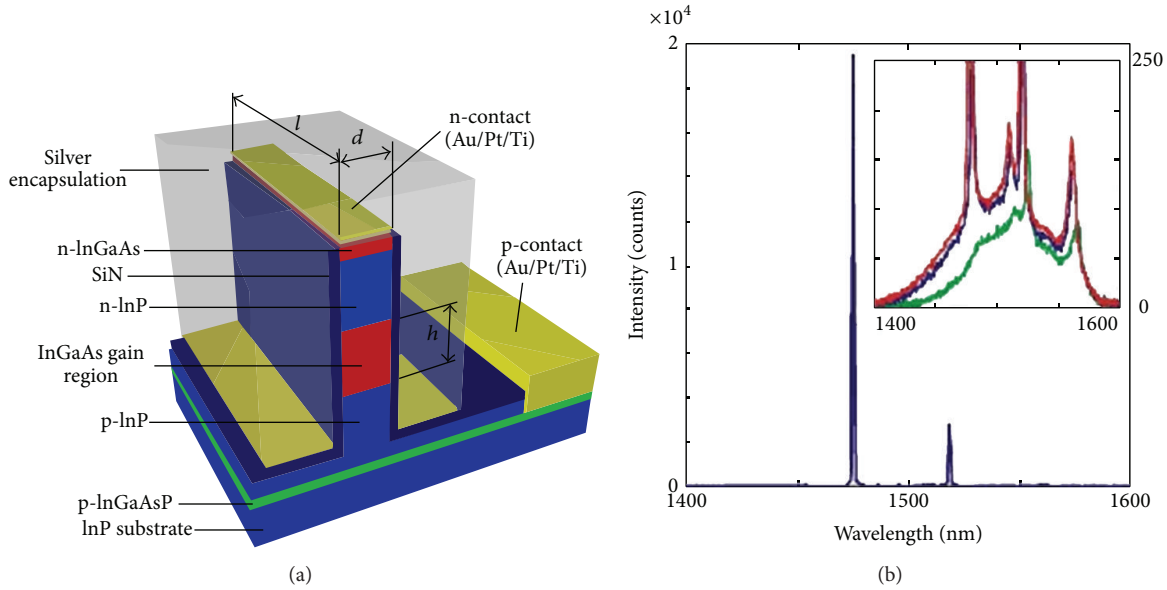


FIGURE 11: (a) Schematic showing the device layer structure. (b) Spectra and near field patterns showing lasing in devices. Above threshold emission spectrum for 3-micron-long device with semiconductor core width of $d \sim 130$ nm (± 20 nm), with pump current of $180 \mu\text{A}$ at 78 K. Inset: emission spectra, for 20 (green), 40 (blue), and 60 (red) μA , all at 78 K.

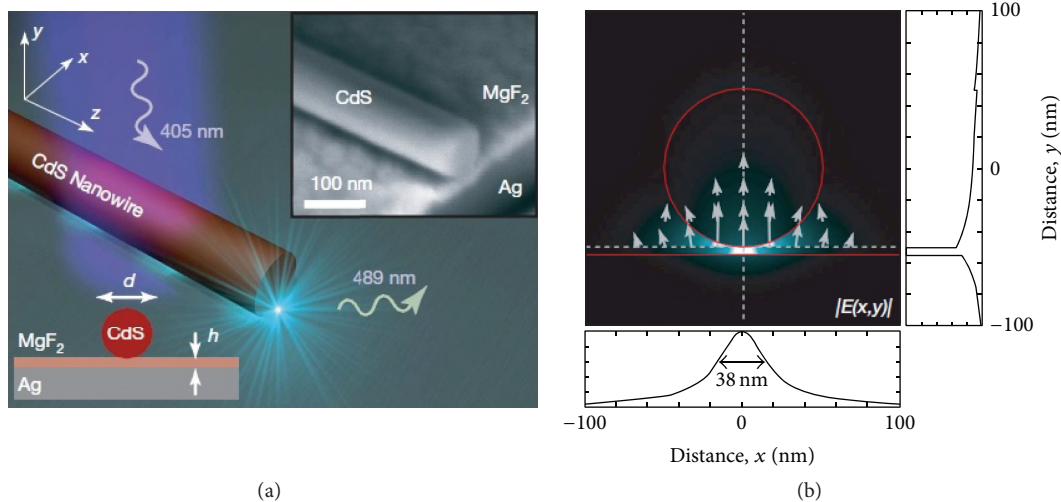


FIGURE 12: (a) The plasmonic laser consists of a CdS semiconductor nanowire on top of a silver substrate separated by a nanoscale MgF_2 layer of thickness h . This structure supports a new type of plasmonic mode, the mode size of which can be a hundred times smaller than a diffraction-limited spot. The inset shows a scanning electron microscope image of a typical plasmonic laser, which has been sliced perpendicular to the nanowire's axis to show the underlying layers. (b) The stimulated electric field distribution and direction $|E(x, y)|$ of a hybrid plasmonic mode at a wavelength of 489 nm, corresponding to the CdS I_2 exciton line. The cross-sectional field plots (along the broken lines in the field map) illustrate the strong overall confinement in the gap region between the nanowire and metal surface with sufficient modal overlap in the semiconductor to facilitate gain.

feedback through total internal reflection of surface plasmons at the cavity boundaries.

The interaction between SPPs and semiconductors at nanoscale is becoming the research focus in the fundamental physics. The amplification based on semiconductor nanostructure has been experimentally demonstrated. Three characters (small size, high refractive index, and free

standing nanocavity emit) make semiconductor nanostructure attractive for potential application in optoelectronics. A further side of this theme is the overcoming of large propagation losses in nanoscale plasmon mode waveguides, creating nanolasers from these waveguides. These lasers will be very important for complex optoelectronics systems in future.

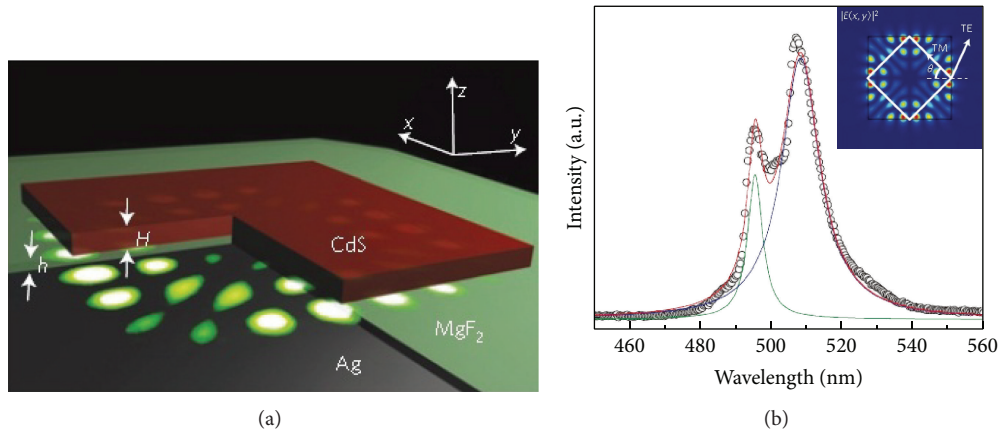


FIGURE 13: (a) Schematic diagram of the room-temperature plasmon laser showing a thin CdS square atop a silver substrate separated by a 5 nm MgF_2 gap, where the most intense electric fields of the device reside. (b) The spontaneous emission spectrum at a peak pump intensity of $1,960 \text{ MW cm}^{-2}$ shows obvious cavity modes despite being below the threshold, which indicates the excellent cavity feedback. The inset shows electric-field-intensity distribution of a TM mode in the x and y directions.

4. Applications of SPPs under Gain Compensation

SPPs, which are electromagnetic waves strongly confined in the direction perpendicular to the metal surface, have the unique ability to concentrate and guide light in subwavelength scale [2, 84]. This certainly provides an abundant basis for studies of light matter interaction at the nanoscale. However, the strong SPPs optical losses are impeded largely for many practical applications, and loss compensation with optical gain will in many cases be feasible when it comes to the design of functional devices.

4.1. Lasers. The construction of a plasmonic laser is similar to that of a conventional laser. SPPs are directly generated on a metal nanostructure and amplified by an adjacent dielectric medium incorporating gain, while a feedback mechanism allows SPPs to resonate. The gain medium amplifies SPPs by stimulating emission of radiation generating coherently amplified light that is bound to the metal dielectric interface and typically cannot escape without coupling optics. The involvement of electrons in the SPPs adds momentum to light, confining it closely to the metal. This confinement effect is used by plasmonic lasers to deliver strong optical energy well below the diffraction barrier on extremely fast time scales. Bergman and Stockman proposed the coupling of energy directly into SPPs by emission for fast and efficient light generation at the nanoscale in 2003 [85]. But their concept was not carried out experimentally until 2009 [33, 82, 86, 87]. There have also been recent works on the amplification and laser action of SPPs. Room-temperature operation has been reported for LRSPP exhibiting low confinement [32, 88, 89] and for tightly confined hybrid SPPs [90]. Meanwhile, the work of Hill and coworkers continued to pioneer electrically injected plasmon lasers [91, 92]. The laser action which can directly generate SPPs has been adapted to commercial lasers. For example, metallic nanostructures have been positioned on the facets of commercial quantum cascade lasers leading

to the strong nanofocusing applied in antennas [93] and the control of beam directionality used as arrays of slits and gratings [94–96].

4.2. Amplifiers. Substantial efforts have been applied to study the amplification of SPPs [25, 32, 49, 65, 97–99] targeting to mitigate or even eliminate their large intrinsic losses in order to enable full potential applications in SPPs. Indeed, the direct observation of SPPs amplification in confined waveguide geometries is elusive. Kéna-Cohen et al. [100] reported the direct observation of plasmonic amplification in confined and lithographically defined SPPs waveguides of varying length. At the highest pump powers, they found that the SPPs loss was completely compensated by the optically pumped organic gain medium and resulted in a substantial net gain of 93 dB/mm for the best amplifier. de Leon and Berini [101] measured the amplified spontaneous emission in a LRSPP amplifier at a near infrared wavelength and found an effective input noise power of photons per mode. Then, they also presented a theoretical and numerical study of the noise properties of high gain planar SPPs amplifiers combined with dipolar gain media [102]. On this basis, they showed a theoretical study of gain and noise in a LRSPP amplifier which consisted of a symmetric thin metal film with an optically pumped gain medium [103]. The amplifier structure was shown in Figure 14. It consisted of a 20 nm thick gold film deposited on a semi-infinite SiO_2 substrate and covered by a gain medium in the form of optically pumped LDS821 dye molecules. A semi-infinite SiO_2 within a 1 mm thick layer was covered on the dye. The structure was pumped from the top using monochromatic light with a wavelength of $\lambda_p = 532 \text{ nm}$ which was close to the dye's peak absorption. The amplification of SPPs sets up the foundation for many interesting, useful, and compelling applications; for instance, SPP amplifiers can be used as components integrated with plasmonic elements, biosensors, or circuitry to compensate for losses or otherwise brilliance characteristics.

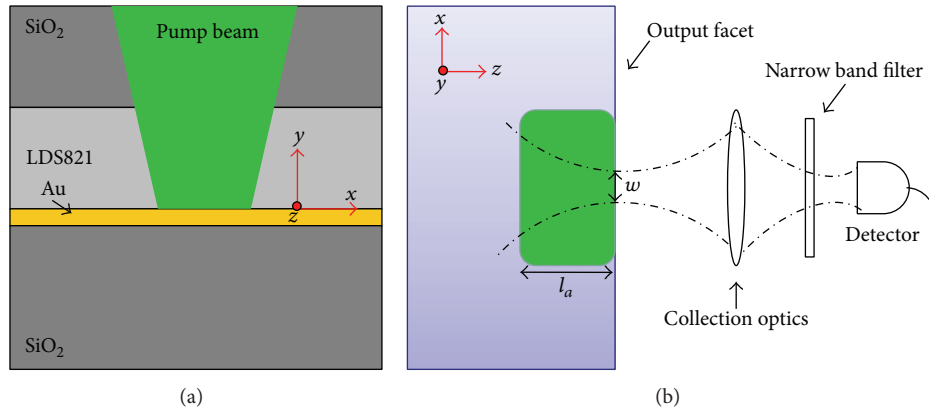


FIGURE 14: LRSP amplifier structure: (a) front cross-sectional view. (b) Top view and detection system.

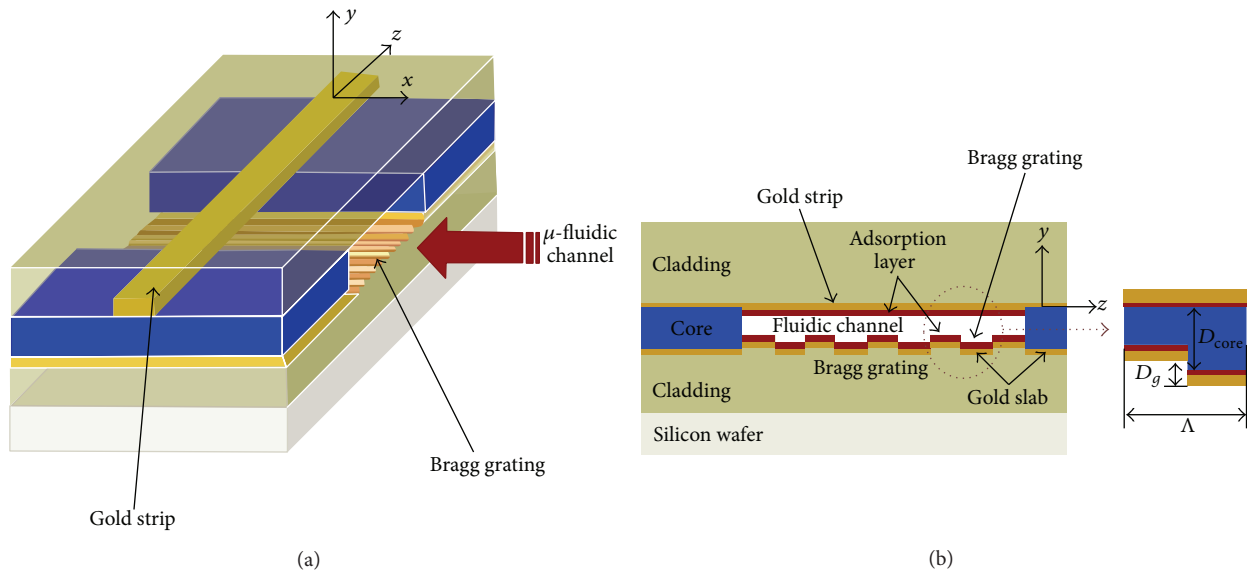


FIGURE 15: (a) A schematic of LRSP waveguide sensor, (b) cross-sectional views of the sensor structure.

4.3. LRSP Waveguide. In recent years, the LRSP excited at the interfaces of metal thin films embedded in a gain medium have generated significant research interest. In terms of potential uses of SPPs waveguides, the strength of the limitation is an urgent issue. Theoretical and experimental [104, 105] studies have demonstrated that a long range mode can be propagated in single polarization over a distance of several μm in a simple structure composed of a thin metal strip embedded in dielectric materials. For LRSP waveguides, single polarization operation and the high precision can be achieved in patterning the waveguide core layer contributing to high performance of LRSP based quantum optical circuits. Fabrication of active and passive optical components, including Y-splitters, directional couplers, switch, attenuators, sensor, and Mach-Zehnder wavelength filters, has been demonstrated by several groups [105–109] (Figure 15).

5. Conclusion

The presence of SPPs in metallic nanostructures relates to a variety of unique optical effects. But in many cases, optical losses greatly limit the applicability of plasmonic technologies as a means of realizing. This obstacle can be overcome by adding optical gain to compensate for loss alters and allow SPPs to propagate over longer distances. In this review, we showed the two SPPs optical amplification mechanisms including spontaneous radiation amplification and simulated radiation amplification. Many improvements can be achieved by means of the optimization of the geometry and materials, but the optical losses are caused by the physical performances of the metal and can well be dealt with by introducing optical gain into the structure. Then, we introduced several gain mediums, such as dye doped, QDs, erbium ion, and semiconductor, to compensate optical loss of SPPs. Using gain

medium mentioned above can compensate losses and achieve many potential applications, for example, laser, amplifier, and LRSPP. In the future, SPPs geometries with a range of gain material have been shown to provide a suitable platform for the study of net plasmon amplification and will lead to useful and helpful applications.

Conflict of Interests

The authors declare that there is no conflict of interests regarding the publication of this paper.

Acknowledgments

This work is supported by NSFC under Grant no. 61307066, Doctoral Fund of Ministry of Education of China under Grant nos. 20110092110016 and 20130092120024, Natural Science Foundation of Jiangsu Province under Grant no. BK20130630, the National Basic Research Program of China (973 Program) under Grant no. 2011CB302004, and the Foundation of Key Laboratory of Micro-Inertial Instrument and Advanced Navigation Technology, Ministry of Education, China, under Grant no. 201204.

References

- [1] W. L. Barnes, "Surface plasmon-polariton length scales: a route to sub-wavelength optics," *Journal of Optics A: Pure and Applied Optics*, vol. 8, no. 4, pp. S87–S93, 2006.
- [2] W. L. Barnes, A. Dereux, and T. W. Ebbesen, "Surface plasmon subwavelength optics," *Nature*, vol. 424, no. 6950, pp. 824–830, 2003.
- [3] S. A. Maier and H. A. Atwater, "Plasmonics: localization and guiding of electromagnetic energy in metal/dielectric structures," *Journal of Applied Physics*, vol. 98, no. 1, Article ID 011101, 2005.
- [4] C. L. Haynes, A. D. McFarland, and R. P. van Duyne, "Surface-enhanced: raman spectroscopy," *Analytical Chemistry*, vol. 77, no. 17, pp. 338A–346A, 2005.
- [5] D. K. Gramotnev and S. I. Bozhevolnyi, "Plasmonics beyond the diffraction limit," *Nature Photonics*, vol. 4, no. 2, pp. 83–91, 2010.
- [6] S. Kawata, Y. Inouye, and P. Verma, "Plasmonics for near-field nano-imaging and superlensing," *Nature Photonics*, vol. 3, no. 7, pp. 388–394, 2009.
- [7] J. N. Anker, W. P. Hall, O. Lyandres, N. C. Shah, J. Zhao, and R. P. van Duyne, "Biosensing with plasmonic nanosensors," *Nature Materials*, vol. 7, no. 6, pp. 442–453, 2008.
- [8] J. Homola, "Surface plasmon resonance sensors for detection of chemical and biological species," *Chemical Reviews*, vol. 108, no. 2, pp. 462–493, 2008.
- [9] T. W. Ebbesen, C. Genet, and S. I. Bozhevolnyi, "Surface-plasmon circuitry," *Physics Today*, vol. 61, no. 5, pp. 44–50, 2008.
- [10] P. Berini and I. de Leon, "Surface plasmon-polariton amplifiers and lasers," *Nature Photonics*, vol. 6, no. 1, pp. 16–24, 2012.
- [11] J. B. Khurgin and A. Boltasseva, "Reflecting upon the losses in plasmonics and metamaterials," *MRS Bulletin*, vol. 37, no. 8, pp. 768–779, 2012.
- [12] R. Charbonneau, P. Berini, E. Berolo, and E. Lisicka-Shrzek, "Experimental observation of plasmon-polariton waves supported by a thin metal film of finite width," *Optics Letters*, vol. 25, no. 11, pp. 844–846, 2000.
- [13] P. Berini, "Long-range surface plasmon-polariton waveguides in silica," *Journal of Applied Physics*, vol. 102, no. 5, Article ID 053105, 2007.
- [14] T. Holmgaard and S. I. Bozhevolnyi, "Theoretical analysis of dielectric-loaded surface plasmon-polariton waveguides," *Physical Review B*, vol. 75, no. 24, Article ID 245405, 2007.
- [15] M. Seidel and R. Niessner, "Automated analytical microarrays: a critical review," *Analytical and Bioanalytical Chemistry*, vol. 391, no. 5, pp. 1521–1544, 2008.
- [16] M. E. Stewart, C. R. Anderton, L. B. Thompson et al., "Nanostructured plasmonic sensors," *Chemical Reviews*, vol. 108, no. 2, pp. 494–521, 2008.
- [17] J. R. Lakowicz, "Plasmonics in biology and plasmon-controlled fluorescence," *Plasmonics*, vol. 1, no. 1, pp. 5–33, 2006.
- [18] J. Dostálek and W. Knoll, "Biosensors based on surface plasmon-enhanced fluorescence spectroscopy," *Biointerphases*, vol. 3, no. 3, pp. FD12–FD22, 2008.
- [19] J. R. Lakowicz, J. Malicka, I. Gryczynski, and Z. Gryczynski, "Directional surface plasmon-coupled emission: a new method for high sensitivity detection," *Biochemical and Biophysical Research Communications*, vol. 307, no. 3, pp. 435–439, 2003.
- [20] J. S. Yuk, M. Trnavsky, C. McDonagh, and B. D. MacCraith, "Surface plasmon-coupled emission (SPCE)-based immunoassay using a novel paraboloid array biochip," *Biosensors and Bioelectronics*, vol. 25, no. 6, pp. 1344–1349, 2010.
- [21] S. C. Kitson, W. L. Barnes, and J. R. Sambles, "Photoluminescence from dye molecules on silver gratings," *Optics Communications*, vol. 122, no. 4–6, pp. 147–154, 1996.
- [22] A. N. Sudarkin and P. A. Demkovich, "Excitation of surface electromagnetic waves on the boundary of a metal with an amplifying medium," *Soviet Physics—Technical Physics*, vol. 34, pp. 764–766, 1989.
- [23] G. A. Plotz, H. J. Simon, and J. M. Tucciarone, "Enhanced total reflection with surface plasmons," *Journal of the Optical Society of America*, vol. 69, no. 3, pp. 419–422, 1979.
- [24] T. Okamoto, J. Simonen, and S. Kawata, "Plasmonic crystal for efficient energy transfer from fluorescent molecules to long-range surface plasmons," *Optics Express*, vol. 17, no. 10, pp. 8294–8301, 2009.
- [25] I. de Leon and P. Berini, "Amplification of long-range surface plasmons by a dipolar gain medium," *Nature Photonics*, vol. 4, no. 6, pp. 382–387, 2010.
- [26] A. Kasry and W. Knoll, "Long range surface plasmon fluorescence spectroscopy," *Applied Physics Letters*, vol. 89, no. 10, Article ID 101106, 2006.
- [27] J. Dostálek, A. Kasry, and W. Knoll, "Long range surface plasmons for observation of biomolecular binding events at metallic surfaces," *Plasmonics*, vol. 2, no. 3, pp. 97–106, 2007.
- [28] Y. Wang, A. Brunsen, U. Jonas, J. Dostálek, and W. Knoll, "Prostate specific antigen biosensor based on long range surface plasmon-enhanced fluorescence spectroscopy and dextran hydrogel binding matrix," *Analytical Chemistry*, vol. 81, no. 23, pp. 9625–9632, 2009.
- [29] Y. Wang, J. Dostálek, and W. Knoll, "Long range surface plasmon-enhanced fluorescence spectroscopy for the detection of aflatoxin M₁ in milk," *Biosensors and Bioelectronics*, vol. 24, no. 7, pp. 2264–2267, 2009.

- [30] G. Winter, S. Wedge, and W. L. Barnes, "Can lasing at visible wavelengths be achieved using the low-loss long-range surface plasmon-polariton mode?" *New Journal of Physics*, vol. 8, no. 8, article 125, 2006.
- [31] M. A. Noginov, G. Zhu, M. Mayy, B. A. Ritzo, N. Noginova, and V. A. Podolskiy, "Stimulated emission of surface plasmon polaritons," *Physical Review Letters*, vol. 101, no. 22, Article ID 226806, 2008.
- [32] M. C. Gather, K. Meerholz, N. Danz, and K. Leosson, "Net optical gain in a plasmonic waveguide embedded in a fluorescent polymer," *Nature Photonics*, vol. 4, no. 7, pp. 457–461, 2010.
- [33] R. F. Oulton, V. J. Sorger, T. Zentgraf et al., "Plasmon lasers at deep subwavelength scale," *Nature*, vol. 461, no. 7264, pp. 629–632, 2009.
- [34] R. F. Oulton, V. J. Sorger, D. A. Genov, D. F. P. Pile, and X. Zhang, "A hybrid plasmonic waveguide for subwavelength confinement and long-range propagation," *Nature Photonics*, vol. 2, no. 8, pp. 496–500, 2008.
- [35] Y. Li, F. Qian, J. Xiang, and C. M. Lieber, "Nanowire electronic and optoelectronic devices," *Materials Today*, vol. 9, no. 10, pp. 18–27, 2006.
- [36] R. Yan, D. Gargas, and P. Yang, "Nanowire photonics," *Nature Photonics*, vol. 3, no. 10, pp. 569–576, 2009.
- [37] H. Ditlbacher, A. Hohenau, D. Wagner et al., "Silver nanowires as surface plasmon resonators," *Physical Review Letters*, vol. 95, no. 25, Article ID 257403, 2005.
- [38] P. Kusar, C. Gruber, A. Hohenau, and J. R. Krenn, "Measurement and reduction of damping in plasmonic nanowires," *Nano Letters*, vol. 12, no. 2, pp. 661–665, 2012.
- [39] N. Liu, H. Wei, J. Li et al., "Plasmonic amplification with ultrahigh optical gain at room temperature," *Scientific Reports*, vol. 3, article 1967, 2013.
- [40] X. Wu, Y. Xiao, C. Meng et al., "Hybrid photon-plasmon nanowire lasers," *Nano Letters*, vol. 13, no. 11, pp. 5654–5659, 2013.
- [41] J. Valentine, S. Zhang, T. Zentgraf et al., "Three-dimensional optical metamaterial with a negative refractive index," *Nature*, vol. 455, no. 7211, pp. 376–379, 2008.
- [42] I. de Leon and P. Berini, "Theory of surface plasmon-polariton amplification in planar structures incorporating dipolar gain media," *Physical Review B*, vol. 78, no. 16, Article ID 161401, 2008.
- [43] I. P. Radko, M. G. Nielsen, O. Albrechtsen, and S. I. Bozhevolnyi, "Stimulated emission of surface plasmon polaritons by lead-sulphide quantum dots at near infra-red wavelengths," *Optics Express*, vol. 18, no. 18, pp. 18633–18641, 2010.
- [44] C. Garcia, V. Coello, Z. Han, I. P. Radko, and S. I. Bozhevolnyi, "Partial loss compensation in dielectric-loaded plasmonic waveguides at near infra-red wavelengths," *Optics Express*, vol. 20, no. 7, pp. 7771–7776, 2012.
- [45] M. Ambati, S. H. Nam, E. Ulin-Avila, D. A. Genov, G. Bartal, and X. Zhang, "Observation of stimulated emission of surface plasmon polaritons," *Nano Letters*, vol. 8, no. 11, pp. 3998–4001, 2008.
- [46] J. Kalkman, L. Kuipers, A. Polman, and H. Gersen, "Coupling of Er ions to surface plasmons on Ag," *Applied Physics Letters*, vol. 86, no. 4, Article ID 041113, 2005.
- [47] M. P. Nezhad, A. Simic, O. Bondarenko et al., "Room-temperature subwavelength metallo-dielectric lasers," *Nature Photonics*, vol. 4, no. 6, pp. 395–399, 2010.
- [48] I. Avrutsky, "Surface plasmons at nanoscale relief gratings between a metal and a dielectric medium with optical gain," *Physical Review B*, vol. 70, no. 15, Article ID 155416, 2004.
- [49] J. Seidel, S. Grafström, and L. Eng, "Stimulated emission of surface plasmons at the interface between a silver film and an optically pumped dye solution," *Physical Review Letters*, vol. 94, no. 17, Article ID 177401, 2005.
- [50] M. A. Noginov, V. A. Podolskiy, G. Zhu et al., "Compensation of loss in propagating surface plasmon polariton by gain in adjacent dielectric medium," *Optics Express*, vol. 16, no. 2, pp. 1385–1392, 2008.
- [51] A. B. Kozyrev, H. Kim, and D. W. van der Weide, "Parametric amplification in left-handed transmission line media," *Applied Physics Letters*, vol. 88, no. 26, Article ID 264101, 2006.
- [52] A. K. Popov and V. M. Shalaev, "Compensating losses in negative-index metamaterials by optical parametric amplification," *Optics Letters*, vol. 31, no. 14, pp. 2169–2171, 2006.
- [53] A. D. Boardman, Y. G. Rapoport, N. J. King, and V. N. Malnev, "Creating stable gain in active metamaterials," *Journal of the Optical Society of America B: Optical Physics*, vol. 24, no. 10, pp. A53–A61, 2007.
- [54] A. A. Govyadinov, V. A. Podolskiy, and M. A. Noginov, "Active metamaterials: sign of refractive index and gain-assisted dispersion management," *Applied Physics Letters*, vol. 91, no. 19, Article ID 191103, 2007.
- [55] A. K. Sarychev and G. Tartakovskiy, "Magnetic plasmonic metamaterials in actively pumped host medium and plasmonic nanolaser," *Physical Review B*, vol. 75, no. 8, Article ID 085436, 2007.
- [56] O. Sydoruk, E. Shamonina, and L. Solymar, "Parametric amplification in coupled magnetoinductive waveguides," *Journal of Physics D: Applied Physics*, vol. 40, no. 22, pp. 6879–6887, 2007.
- [57] A. Bratkovsky, E. Ponziovskaia, S. Wang et al., "A metal-wire/quantum-dot composite metamaterial with negative ϵ and compensated optical loss," *Applied Physics Letters*, vol. 93, no. 19, Article ID 193106, 2008.
- [58] S. Chakrabarti, S. A. Ramakrishna, and H. Wanare, "Coherently controlling metamaterials," *Optics Express*, vol. 16, no. 24, pp. 19504–19511, 2008.
- [59] Z. Dong, H. Liu, T. Li et al., "Resonance amplification of left-handed transmission at optical frequencies by stimulated emission of radiation in active metamaterials," *Optics Express*, vol. 16, no. 25, pp. 20974–20980, 2008.
- [60] S. Chénais and S. Forget, "Recent advances in solid-state organic lasers," *Polymer International*, vol. 61, no. 3, pp. 390–406, 2012.
- [61] D. Bimberg, M. Grundmann, F. Heinrichsdorff et al., "Quantum dot lasers: breakthrough in optoelectronics," *Thin Solid Films*, vol. 367, no. 1–2, pp. 235–249, 2000.
- [62] V. I. Klimov, A. A. Mikhailovsky, S. Xu et al., "Optical gain and stimulated emission in nanocrystal quantum dots," *Science*, vol. 290, no. 5490, pp. 314–317, 2000.
- [63] I. Surez, H. Gordillo, R. Abargues, S. Albert, and J. Martínez-Pastor, "Photoluminescence waveguiding in CdSe and CdTe QDs-PMMA nanocomposite films," *Nanotechnology*, vol. 22, no. 43, Article ID 435202, 2011.
- [64] J. Grandidier, G. C. des Francs, S. Massenet et al., "Gain-assisted propagation in a plasmonic waveguide at telecom wavelength," *Nano Letters*, vol. 9, no. 8, pp. 2935–2939, 2009.
- [65] P. M. Bolger, W. Dickson, A. V. Krasavin et al., "Amplified spontaneous emission of surface plasmon polaritons and limitations on the increase of their propagation length," *Optics Letters*, vol. 35, no. 8, pp. 1197–1199, 2010.

- [66] S. Coffa, A. Polman, and R. N. Schwartz, *Rare Earth Doped Semiconductors II*, Materials Research Society, Pittsburgh, Pa, USA, 1996.
- [67] J. Kalkman, C. Strohhofer, B. Gralak, and A. Polman, "Surface plasmon polariton modified emission of erbium in a metallo-dielectric grating," *Applied Physics Letters*, vol. 83, no. 1, pp. 30–32, 2003.
- [68] Y. Wang and Z. Zhou, "Strong enhancement of erbium ion emission by a metallic double grating," *Applied Physics Letters*, vol. 89, no. 25, Article ID 253122, 2006.
- [69] S. John and T. Quang, "Spontaneous emission near the edge of a photonic band gap," *Physical Review A*, vol. 50, no. 2, pp. 1764–1769, 1994.
- [70] W. L. Barnes, T. W. Preist, S. C. Kitson, and J. R. Sambles, "Physical origin of photonic energy gaps in the propagation of surface plasmons on gratings," *Physical Review B*, vol. 54, no. 9, pp. 6227–6244, 1996.
- [71] S. C. Kitson, W. L. Barnes, and J. R. Sambles, "Surface-plasmon energy gaps and photoluminescence," *Physical Review B*, vol. 52, no. 15, pp. 11441–11445, 1995.
- [72] Y. Wang and Z. Zhou, "Silicon optical amplifier based on surface-plasmon-polariton enhancement," *Applied Physics Letters*, vol. 91, no. 5, Article ID 053504, 2007.
- [73] J. R. Lakowicz, "Radiative decay engineering 5: metal-enhanced fluorescence and plasmon emission," *Analytical Biochemistry*, vol. 337, no. 2, pp. 171–194, 2005.
- [74] A. E. Christensen, C. Uhrenfeldt, B. Julsgaard, P. Balling, and A. N. Larsen, "Interaction between Au nanoparticles and Er^{3+} ions in a TiO_2 matrix: up-conversion of infrared light," *Energy Procedia*, vol. 10, pp. 111–116, 2011.
- [75] E. Verhagen, L. Kuipers, and A. Polman, "Field enhancement in metallic subwavelength aperture arrays probed by erbium upconversion luminescence," *Optics Express*, vol. 17, no. 17, pp. 14586–14598, 2009.
- [76] S. Gradečak, F. Qian, Y. Li, H. Park, and C. M. Lieber, "GaN nanowire lasers with low lasing thresholds," *Applied Physics Letters*, vol. 87, no. 17, Article ID 173111, 2005.
- [77] M. A. Zimmler, J. Bao, F. Capasso, S. Müller, and C. Ronning, "Laser action in nanowires: observation of the transition from amplified spontaneous emission to laser oscillation," *Applied Physics Letters*, vol. 93, no. 5, Article ID 051101, 2008.
- [78] R. Agarwal, C. J. Barrelet, and C. M. Lieber, "Lasing in single cadmium sulfide nanowire optical cavities," *Nano Letters*, vol. 5, no. 5, pp. 917–920, 2005.
- [79] A. V. Maslov and C. Z. Ning, "Reflection of guided modes in a semiconductor nanowire laser," *Applied Physics Letters*, vol. 83, no. 6, pp. 1237–1239, 2003.
- [80] P. J. Pauzauskie, D. J. Sirbuly, and P. Yang, "Semiconductor nanowire ring resonator laser," *Physical Review Letters*, vol. 96, no. 14, Article ID 143903, 2006.
- [81] T. Zhang, G. Qian, Y.-Y. Wang et al., "Integrated optical gyroscope using active Long-range surface plasmon-polariton waveguide resonator," *Scientific Reports*, vol. 4, article 3855, 2014.
- [82] M. T. Hill, M. Marell, E. S. P. Leong et al., "Lasing in metal-insulator-metal sub-wavelength plasmonic waveguides," *Optics Express*, vol. 17, no. 13, pp. 11107–11112, 2009.
- [83] R. Ma, R. F. Oulton, V. J. Sorger, G. Bartal, and X. Zhang, "Room-temperature sub-diffraction-limited plasmon laser by total internal reflection," *Nature Materials*, vol. 10, no. 2, pp. 110–113, 2011.
- [84] H. Raether, "Surface plasmons on gratings," in *Surface Plasmons on Smooth and Rough Surfaces and on Gratings*, pp. 91–116, 1988.
- [85] D. J. Bergman and M. I. Stockman, "Surface plasmon amplification by stimulated emission of radiation: quantum generation of coherent surface plasmons in nanosystems," *Physical Review Letters*, vol. 90, no. 2, Article ID 027402, 2003.
- [86] M. A. Noginov, G. Zhu, A. M. Belgrave et al., "Demonstration of a spaser-based nanolaser," *Nature*, vol. 460, no. 7259, pp. 1110–1112, 2009.
- [87] V. J. Sorger and X. Zhang, "Spotlight on plasmon lasers," *Science*, vol. 333, no. 6043, pp. 709–710, 2011.
- [88] R. A. Flynn, C. S. Kim, I. Vurgaftman et al., "A room-temperature semiconductor spaser operating near $1.5 \mu\text{m}$," *Optics Express*, vol. 19, no. 9, pp. 8954–8961, 2011.
- [89] J. K. Kitur, V. A. Podolskiy, and M. A. Noginov, "Stimulated emission of surface plasmon polaritons in a microcylinder cavity," *Physical Review Letters*, vol. 106, no. 18, Article ID 183903, 2011.
- [90] M. Walter, J. Walowski, V. Zbarsky et al., "Seebeck effect in magnetic tunnel junctions," *Nature Materials*, vol. 10, no. 10, pp. 742–746, 2011.
- [91] M. J. H. Marell, B. Smalbrugge, E. J. Geluk et al., "Plasmonic distributed feedback lasers at telecommunications wavelengths," *Optics Express*, vol. 19, no. 16, pp. 15109–15118, 2011.
- [92] K. Ding, Z. Liu, L. Yin et al., "Electrical injection, continuous wave operation of subwavelength-metallic-cavity lasers at 260 K," *Applied Physics Letters*, vol. 98, no. 23, Article ID 231108, 2011.
- [93] E. Cubukcu, E. A. Kort, K. B. Crozier, and F. Capasso, "Plasmonic laser antenna," *Applied Physics Letters*, vol. 89, no. 9, Article ID 093120, 2006.
- [94] N. Yu, J. Fan, Q. J. Wang et al., "Small-divergence semiconductor lasers by plasmonic collimation," *Nature Photonics*, vol. 2, no. 9, pp. 564–570, 2008.
- [95] J. A. Rogers, M. Meier, A. Dodabalapur, E. J. Laskowski, and M. A. Cappuzzo, "Distributed feedback ridge waveguide lasers fabricated by nanoscale printing and molding on nonplanar substrates," *Applied Physics Letters*, vol. 74, no. 22, pp. 3257–3259, 1999.
- [96] H. Ma, A. K.-Y. Jen, and L. R. Dalton, "Polymer-based optical waveguides materials, processing, and devices," *Advanced Materials*, vol. 14, no. 19, pp. 1339–1365, 2002.
- [97] M. T. Hill, Y. Oei, B. Smalbrugge et al., "Lasing in metallic-coated nanocavities," *Nature Photonics*, vol. 1, no. 10, pp. 589–594, 2007.
- [98] D. Amarasinghe, A. Ruseckas, A. E. Vasdekis, M. Goossens, G. A. Turnbull, and I. D. W. Samuel, "Broadband solid state optical amplifier based on a semiconducting polymer," *Applied Physics Letters*, vol. 89, no. 20, Article ID 201119, 2006.
- [99] D. Amarasinghe, A. Ruseckas, A. E. Vasdekis, G. A. Turnbull, and I. D. W. Samuel, "Amplification of optical pulse sequences at a high repetition rate in a polymer slab waveguide," *Applied Physics Letters*, vol. 91, no. 1, Article ID 011105, 2007.
- [100] S. Kéna-Cohen, P. N. Stavrinou, D. D. C. Bradley, and S. A. Maier, "Confined surface plasmon-polariton amplifiers," *Nano Letters*, vol. 13, no. 3, pp. 1323–1329, 2013.
- [101] I. de Leon and P. Berini, "Spontaneous emission in long-range surface plasmon-polariton amplifiers," *Physical Review B*, vol. 83, no. 8, Article ID 081414, 2011.
- [102] I. de Leon and P. Berini, "Theory of noise in high-gain surface plasmon-polariton amplifiers incorporating dipolar gain media," *Optics Express*, vol. 19, no. 21, pp. 20506–20517, 2011.

- [103] I. De Leon and P. Berini, "Gain and noise in long-range surface plasmon-polariton amplifiers," in *CLEO: Applications and Technology*, p. JTuI30, Optical Society of America, 2011.
- [104] P. Berini, "Plasmon-polariton modes guided by a metal film of finite width bounded by different dielectrics," *Optics Express*, vol. 7, no. 10, pp. 329–335, 2000.
- [105] R. Charbonneau, C. Scales, I. Breukelaar et al., "Passive integrated optics elements based on long-range surface plasmon polaritons," *Journal of Lightwave Technology*, vol. 24, no. 1, pp. 477–494, 2006.
- [106] A. Boltasseva and S. I. Bozhevolnyi, "Directional couplers using long-range surface plasmon polariton waveguides," *IEEE Journal on Selected Topics in Quantum Electronics*, vol. 12, no. 6, pp. 1233–1241, 2006.
- [107] J. T. Kim, S. Park, J. J. Ju, S. K. Park, M. Kim, and M. Lee, "Low-loss polymer-based long-range surface plasmon-polariton waveguide," *IEEE Photonics Technology Letters*, vol. 19, no. 18, pp. 1374–1376, 2007.
- [108] T. Nikolajsen, K. Leosson, and S. I. Bozhevolnyi, "Surface plasmon polariton based modulators and switches operating at telecom wavelengths," *Applied Physics Letters*, vol. 85, no. 24, pp. 5833–5835, 2004.
- [109] G. Gagnon, N. Lahoud, G. A. Mattiussi, and P. Berini, "Thermally activated variable attenuation of long-range surface plasmon-polariton waves," *Journal of Lightwave Technology*, vol. 24, no. 11, pp. 4391–4402, 2006.

Review Article

Transmissive/Reflective Structural Color Filters: Theory and Applications

Yan Yu,^{1,2} Long Wen,² Shichao Song,² and Qin Chen^{2,3}

¹ Department of Physics, Shanghai University, Shanghai 200444, China

² Key Lab of Nanodevices and Applications-CAS and Collaborative Innovation Center of Suzhou Nano Science and Technology, Suzhou Institute of Nano-Tech and Nano-Bionics, Chinese Academy of Sciences (CAS), Suzhou 215123, China

³ Peking University Shenzhen SOC Key Laboratory, PKU-HKUST Shenzhen-Hong Kong Institute, Hi-Tech Industrial Park South, Shenzhen 518057, China

Correspondence should be addressed to Qin Chen; qchen2012@sinano.ac.cn

Received 28 February 2014; Accepted 18 April 2014; Published 15 July 2014

Academic Editor: Tong Zhang

Copyright © 2014 Yan Yu et al. This is an open access article distributed under the Creative Commons Attribution License, which permits unrestricted use, distribution, and reproduction in any medium, provided the original work is properly cited.

Structural color filters, which obtain color selection by varying structures, have attracted extensive research interest in recent years due to the advantages of compactness, stability, multifunctions, and so on. In general, the mechanisms of structural colors are based on the interaction between light and structures, including light diffraction, cavity resonance, and surface plasmon resonance. This paper reviews recent progress of various structural color techniques and the integration applications of structural color filters in CMOS image sensors, solar cells, and display.

1. Introduction

Color is one of the most important properties of vision. The color filters, either reflective or transmissive, provide the ability to select individual colors from a white light, which is the prerequisite of colorful imaging and display. Pigment and dye are the most popularly used color filters, which are based on the material selective absorption in the visible band [1]. Various pigments or dyes have to be integrated together by multistep processing to realize a colorful image. For example, in an image sensor with pixels arranged in Bayer's array, three aligned photolithography processes are necessary to define the red, green, and blue color pixels [2]. Alternatively, color can be generated by manipulating the propagation of light, for example, using dispersive gratings based on the light diffraction theory. It can be found in nature like the wings of butterflies [3, 4], where different structures on the wings show different colors. In contrast to the pigments and dyes, the called *structural color* is based on the interaction between light and the structures rather than the material properties. As a result, a complete set of structural color filters can be readily achieved in the same material by single-step

patterning of different structures, which provides structural color with a great chance to gain high compactness and cut down the cost. Furthermore, structural color has high resistance to the chemicals and high stability to the heat and radiation and therefore can be used in the extreme environment like the aerospace.

In this review, we will discuss the mechanisms of various structural color filtering techniques for both reflective and transmissive color filters and then focus on the integrated applications of structural color in the fields of imaging, display, and colorful solar cells. Finally, we will summarize the current issues of structural color and possible resolutions.

2. Transmissive/Reflective Structural Color Filters

2.1. Metallic Nanohole Array Color Filters. As is well known, light is usually blocked by a metal sheet and therefore metallic coatings are widely used as mirrors. In 1998, Ebbesen et al. observed the extraordinary optical transmission (EOT) through a silver film with periodic subwavelength

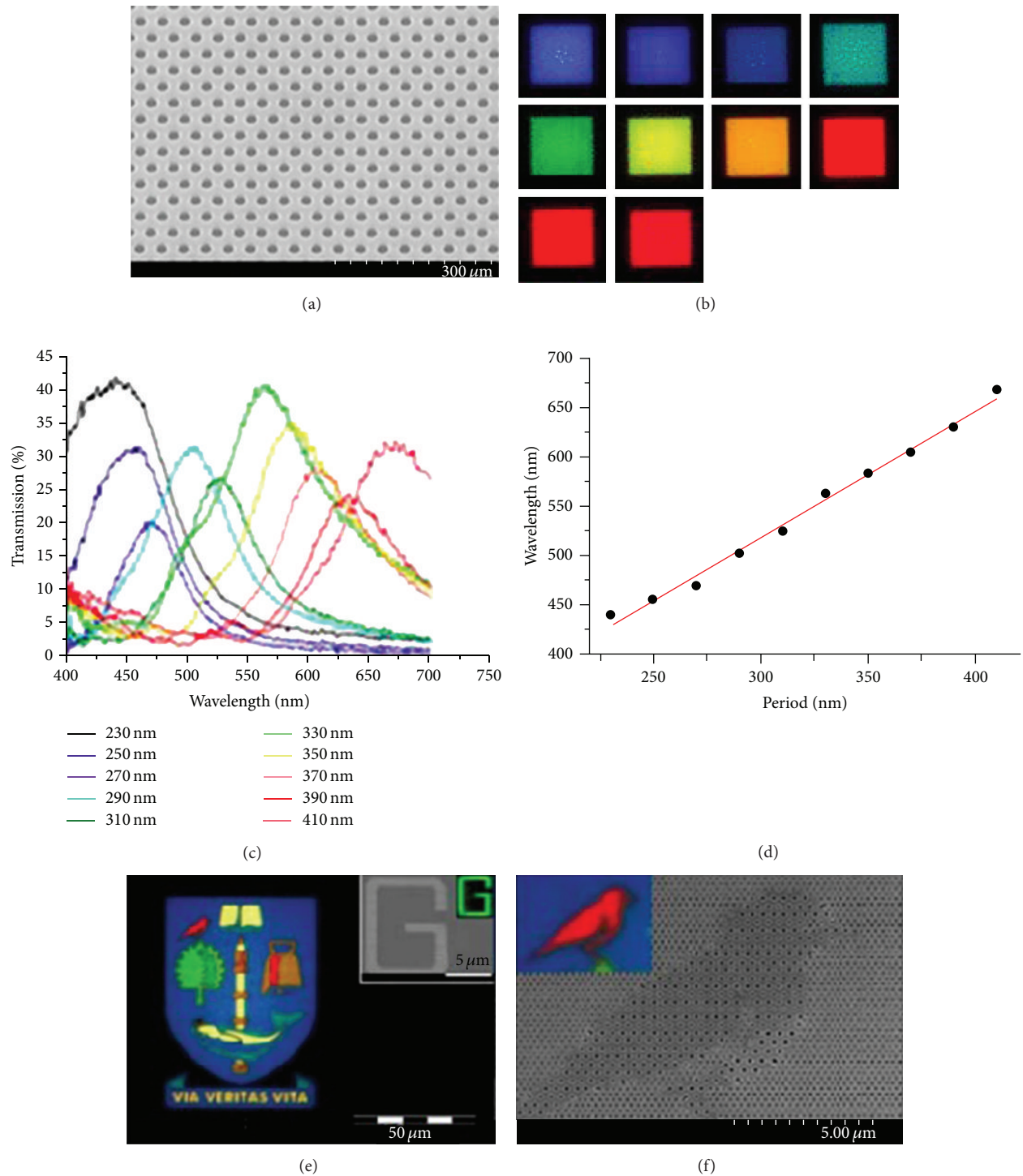


FIGURE 1: Metallic circular hole array transmissive color filters. (a) A SEM image of a hole array in aluminum at a period of 410 nm. (b) Images of hole arrays in different periods taken in microscope transmission mode under a white light illumination. (c) Transmissive spectra of the arrays shown in (b). (d) Wavelengths at the transmission peaks versus the period [17]. (e) Full-color images in microscope transmission mode. Inset is a patterned letter “G” with a 1- μm -wide line showing green color. (f) SEM image of a section of the fabricated logo pattern. The inset is the enlarged microscope image [18].

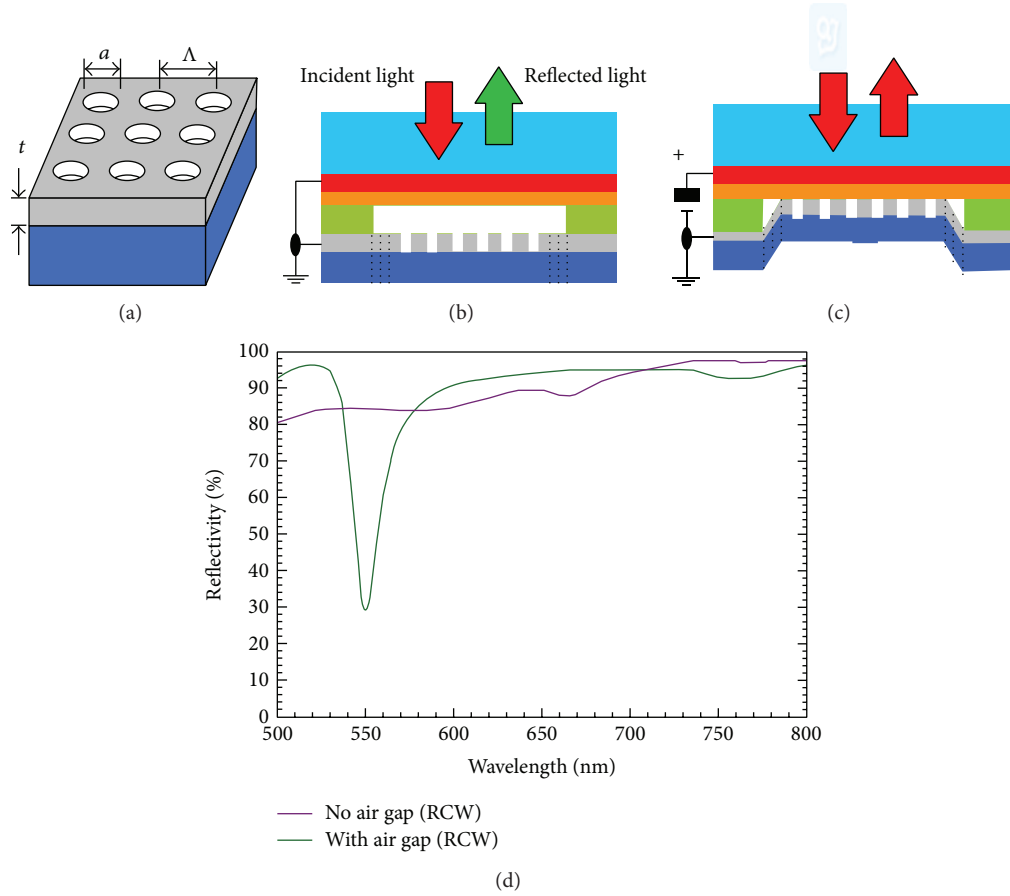


FIGURE 2: Tunable color filter. (a) Schematic of a nanohole array on SOI. (b) The nanohole array has an air gap from the glass plate, that is, “OFF” state. (c) The nanohole array contacts the glass plate, that is, “ON” state. (d) The reflective spectra [27].

hole arrays [5], which contradicts Bethe’s theory on light diffraction by small holes [6]. Although there are debates on the physical mechanisms of this EOT effect, most researchers agree that surface plasmonic resonance (SPR) plays an important role in the color filtering [7–10]. To excite SPR, periodic gratings are usually used to match the wavevector of incident light and that of SPR. The resonant wavelength λ_0 , that is, the transmission peak, is mainly determined by the pattern geometry [11]

$$\lambda_0 = \left(2\pi \sqrt{\frac{\epsilon_m \epsilon_d}{\epsilon_m + \epsilon_d}} \right) \times \left(\left(k_{\parallel} \cos \phi + i \frac{2\pi}{a_x} + j \frac{2\pi}{a_x} \right)^2 + \left(k_{\parallel} \sin \phi - i \frac{2\pi}{a_y} + j \frac{2\pi}{a_y} \right)^2 \right)^{-1/2}, \quad (1)$$

where k_{\parallel} is the in-plane wave vector magnitude, ϕ is the azimuthal angle of incident light, a_x and a_y are the lattice dimensions, i and j are the scattering orders of the array, and ϵ_m and ϵ_d are the permittivity for the metal and dielectric

medium. As shown, the transmissive color can be tuned by simply changing the periods for given material parameters. Metallic hole array color filters in triangular lattice [12–18] and square lattice [19–21] with circular hole [12, 14–21], triangular hole [13], square hole [22], and annular hole [16] have been reported both theoretically and experimentally. Genetic algorithm was used to design filters with the spectral spectrum matching the 1931 International Commission on Illumination color matching functions [8]. Electron beam lithography (EBL) [11–13], nanoimprint [20, 23–25], and nanotransfer print [26] were used to pattern the nanohole array. Chen, one of the authors, fabricated circular hole arrays in triangular lattices in a 150 nm aluminum film [11, 17, 18]. The experimental results are shown in Figure 1. Very regular holes were patterned by EBL in a region of $50 \times 50 \mu\text{m}^2$ for each color. The spectral response was characterized using a microscope spectrometer. The wavelength of transmission peak is found to be nearly linear to the period as shown in Figure 1(d). The transmission is approximately 30% and the full width at half maximum (FWHM) is less than 100 nm. To demonstrate the full control of the color and the high resolution, a complex colorful pattern consisting of different hole arrays was fabricated and the clear colorful image down to a scale of $1 \mu\text{m}$ (letter “G”) was demonstrated in Figure 1(e).

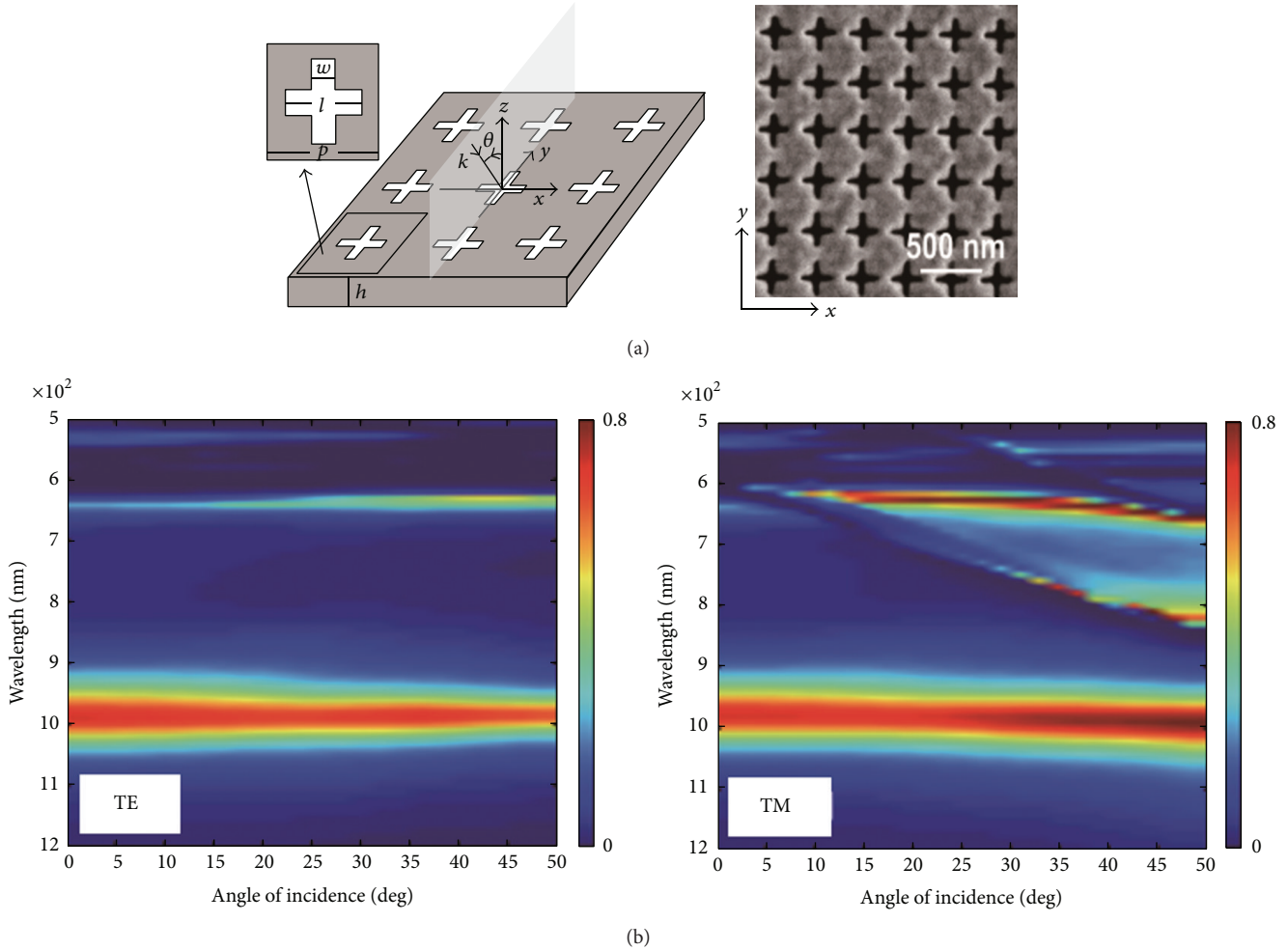


FIGURE 3: Angle robust metallic hole array color filter. (a) Schematic and SEM image of a cross-shape nanohole array. (b) Spectra of both polarizations for different incident angles [28].

Tunability of the structural color based on nanohole array has also been demonstrated by tuning the dielectric environment around the array [27]. As illustrated in Figure 2, the metallic hole array is patterned on top of a suspended silicon layer in a silicon-on-insulator (SOI) wafer, which is capped by an indium-tin-oxide (ITO) covered glass plate with a small gap. The hole array can be switched into contact with the glass plate by electrostatic actuation, resulting in a modified SPR due to the refractive index difference between air and glass. The substantial difference in the reflection spectra can be seen between two states as shown in Figure 2(d), which induces the variation of color.

For some applications such as image sensors and display, angular insensitivity is generally preferred. However, the filtering color of the metallic hole array varies with the incident angle as predicted in (1). When the metallic hole arrays are integrated in the imager or display to replace the pigment color filters, the issue of angle dependent color filtering should be addressed. A lot of cross-shape hole arrays show the most promising performance. In Figure 3, the cross-hole array shows excellent angle independent filtering up

to 50° for both polarizations in the near infrared region [28]. The transmission peak is attributed to the excitation of localized surface plasmon resonance (LSPR) within the apertures, which is determined by the hole shape rather than the coupling between the holes for SPR in circular hole array. We scaled down the cross dimensions and optimized the transmission filtering performance for the visible band. The results are shown in Figure 4, where we can see that the transmission peaks have no obvious shift for the incident angle up to 50° . The red, green, and blue passband are clearly demonstrated.

For a more complex structure consisting of nanohole-nanodisk pair array as shown in Figure 5, there exists LSPR in the gap between nanohole and nanodisk, which induces coupling absorption of incident light due to the excitation of LSPR [29]. As a result, the LSPR dip in the reflection spectra causes a reflective color. As the LSPR effect is confined into a nanoscale, the resolution of the color image by this method could achieve 10^5 dpi, which is 100 times the state-of-the-art imaging technique. A similar dual layer structure in one dimension fabricated by interference lithography has

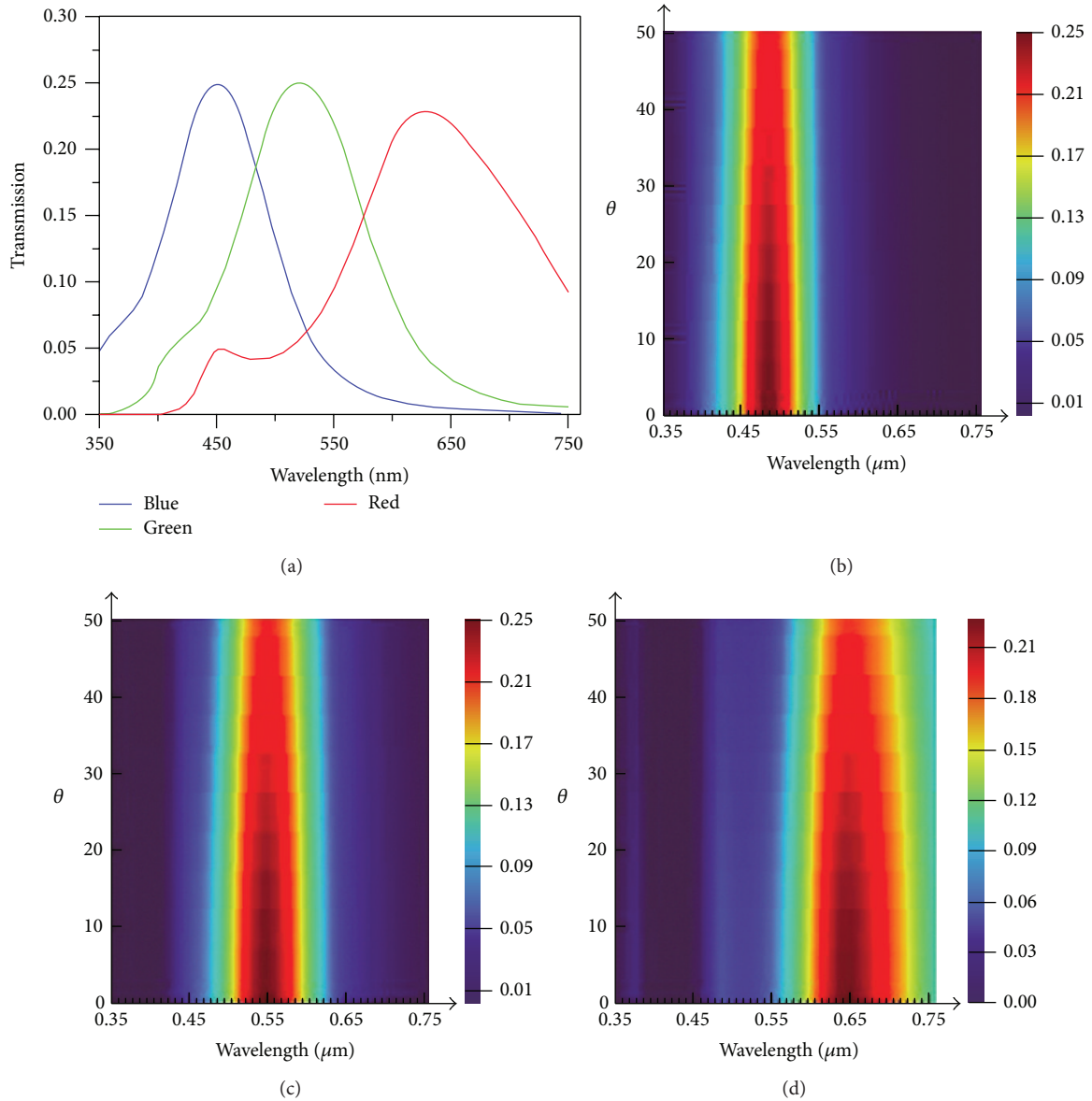


FIGURE 4: (a) Transmission spectra of color filters based on cross-shape nanohole array in the visible band. (b)–(d) are the transmission spectra versus incident angle θ . The geometrical parameters as defined in Figure 3(a): $h = 200$ nm; $l = 120$ nm (blue), 140 nm (green), and 180 nm (red); $w = 48$ nm (blue), 50 nm (green), and 40 nm (red); $p = 150$ nm (blue), 180 nm (green), and 230 nm (red).

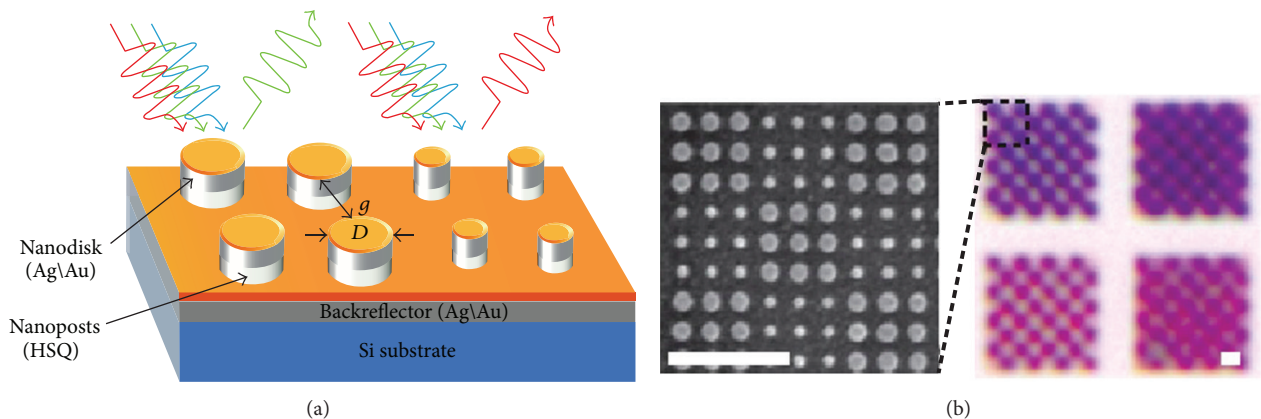


FIGURE 5: Nanohole-nanodisk pair array reflective color filters and the images in microscope reflection mode. Scale bar is 500 nm [29].

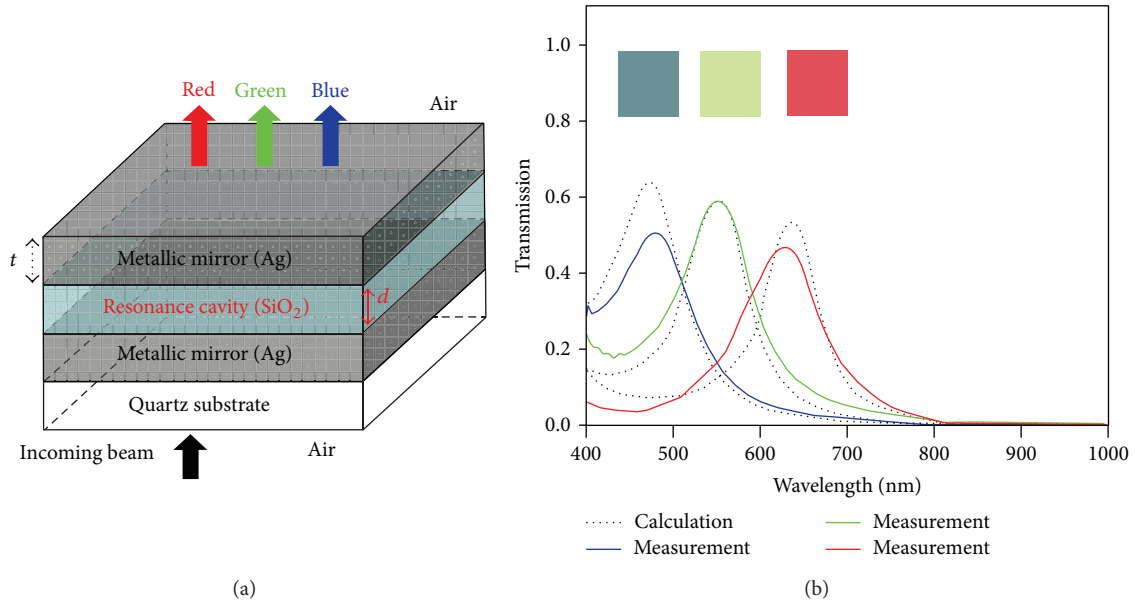


FIGURE 6: (a) Schematic of an etalon color filter. (b) Calculated and measured transmission spectra [36].

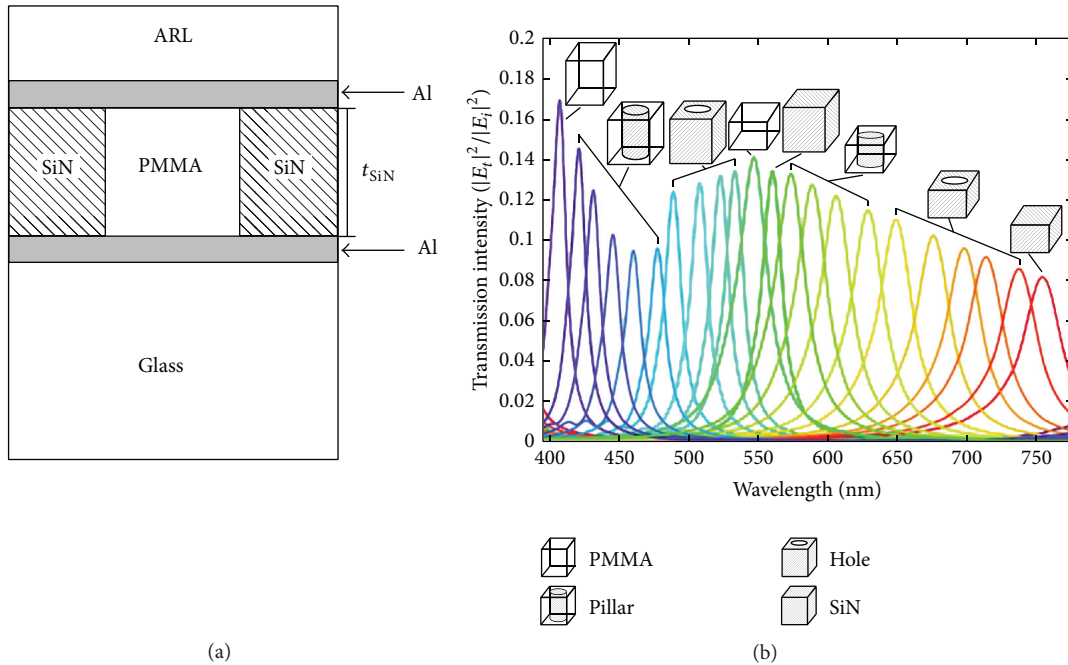


FIGURE 7: (a) Schematic and (b) simulated transmission spectra of modified etalon color filters [39].

also been demonstrated showing both color filtering and polarization functions [30]. In addition, when the bottom hole array in Figure 5 becomes a continuous metal film, the gap plasmon resonance still exists and demonstrates color filtering [31–33].

2.2. Metal-Insulator-Metal (MIM) Resonator Color Filters. Interference effect can also be used for color selection. For example, the Fabry-Pérot (FP) resonance resulting from the interference of the multiple reflected waves is normally used

to determine the lasing wavelength in the laser design, where only the light at the resonance wavelength can be emitted from the cavity. A MIM structure with the semitransparent metal layer as reflective mirrors is such a configuration supporting the FP resonance [34–38]. When the thickness of the insulator layer goes down to hundreds of nanometers, the FP resonances fall into the visible region. The resonance wavelength λ can be obtained by

$$\lambda = 2n_{\text{eff}} \cdot d, \quad (2)$$

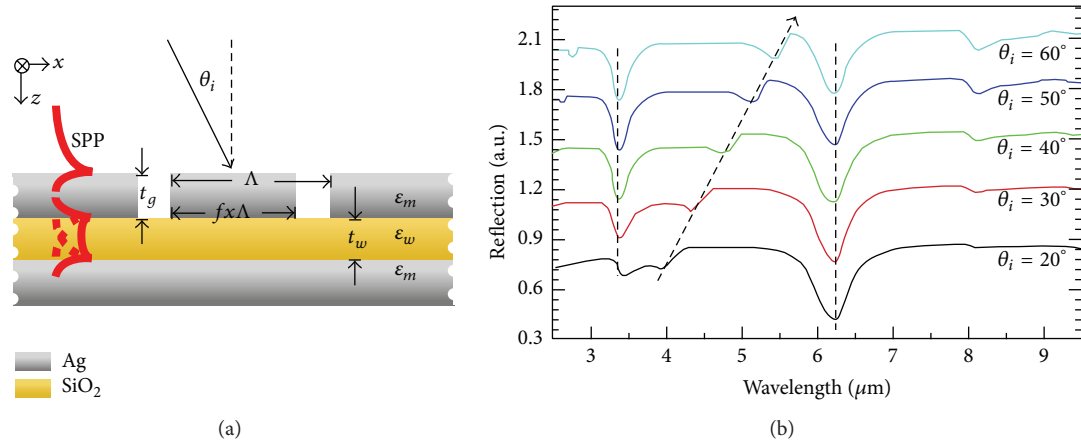


FIGURE 8: (a) Schematic of MIM reflective color filters and (b) simulated reflection spectra versus incident angle [40].

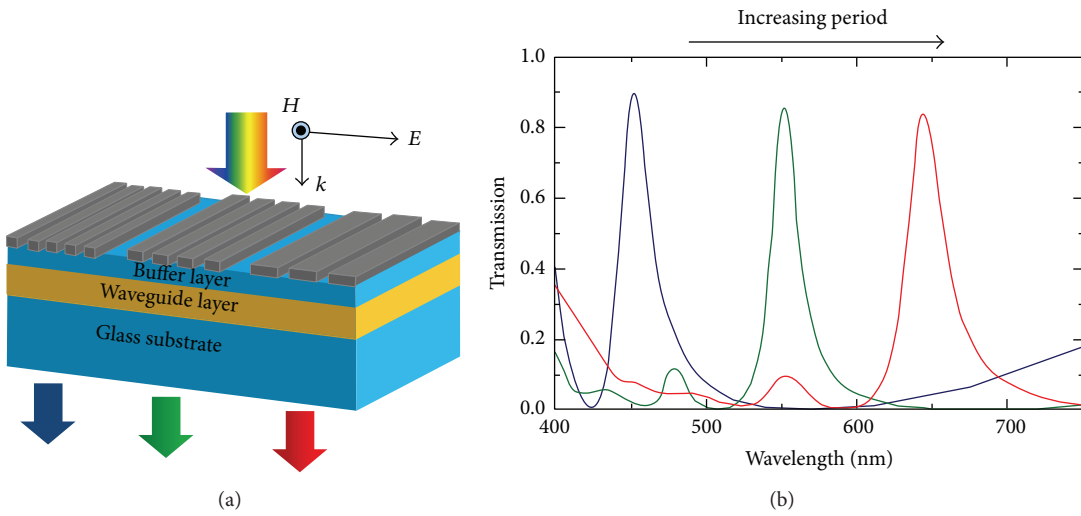


FIGURE 9: (a) Schematic of a transmissive GMR color filter. (b) Simulated transmission spectra [51].

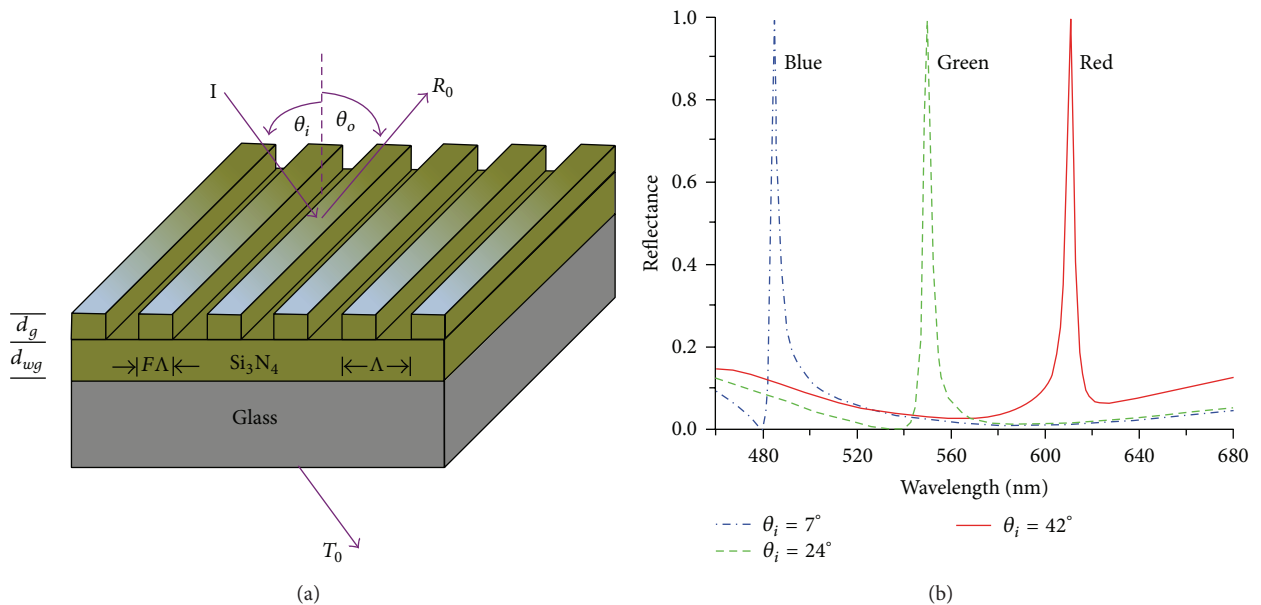


FIGURE 10: (a) Schematic of a reflective GMR color filter. (b) Calculated spectral response of the tunable color filter [57].

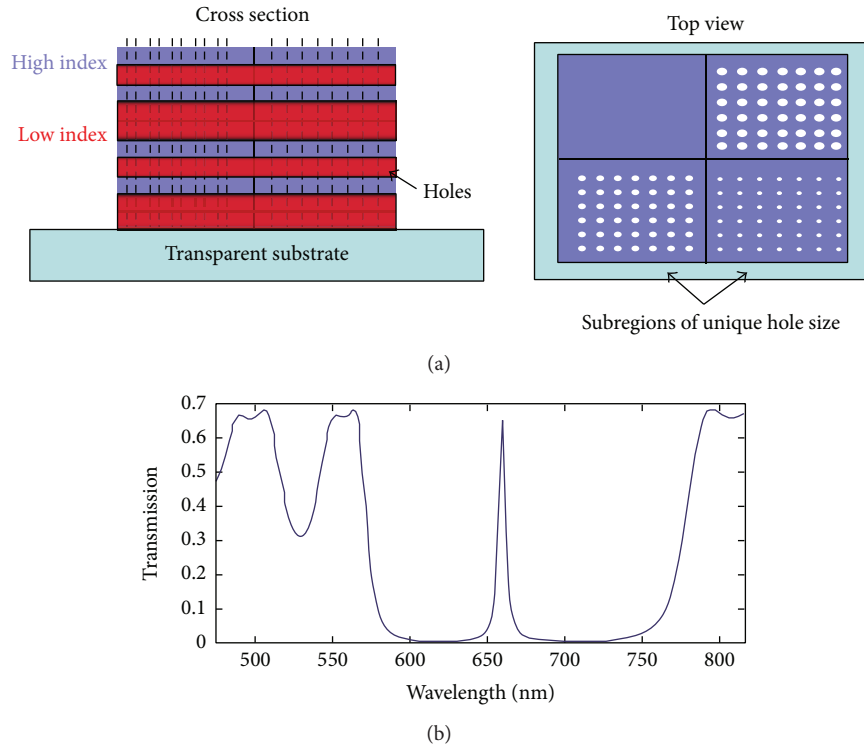


FIGURE 11: (a) Schematic of PhC color filter. (b) Transmission spectrum [62].

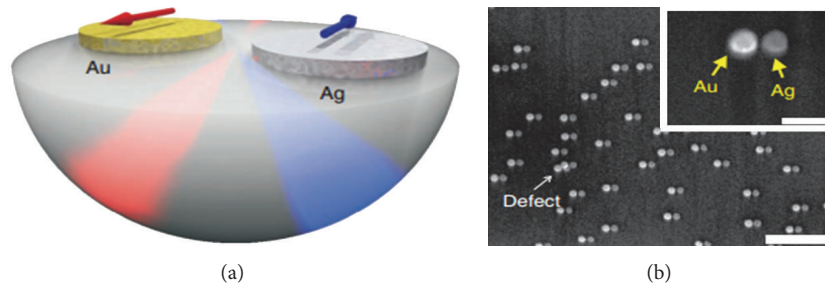


FIGURE 12: Au-Ag disk pair color routing. (a) Schematic and (b) SEM image of the fabricated sample [66].

where n_{eff} is the effective refractive index of the cavity mode and d is the cavity length.

Figure 6 shows such an etalon color filter where a Ag-SiO₂-Ag stack is used to select the transmitted wavelength [36]. Both the simulation and the measured spectra show well-defined red, green, and blue passband. A thin film of silver at 25 nm is used to ensure a reasonable transmittance and provide a mirror reflection. Because the transmission peak at the FP resonance is determined by the cavity length, different color filters need different insulator thickness, which results in multiple-step patterning if various etalon color filters are integrated. To solve this issue, we investigated a modified etalon color filter, in which the top metal mirror and the insulator layer were etched into subwavelength holes and filled with PMMA [39]. Because the hole size is smaller than the light wavelength, it can be treated as an effective material. Varying the hole size, we can change the effective refractive index of the whole stack and therefore tune the FP resonance.

The schematic of this modified etalon color filter is shown in Figure 7(a) and the simulated transmission spectra are shown in Figure 7(b). By varying the hole size, the transmissive colors covering the whole visible band are achieved for only four different insulator thicknesses. Furthermore, the FWHM around 30 nm is much smaller than the hole array color filters, which has potential application in spectral imaging. Reflective color filters based on MIM structure have also been demonstrated [40, 41]. A Ag-SiO₂-Ag structure supports LSPR resulting in angle robust color filtering as shown in Figure 8 [40], which is different from FP cavity resonance. The MIM structure can also be used to tune the guided mode dispersion and construct a plasmonic lens [42–44].

2.3. Guided-Mode-Resonance (GMR) Color Filters. Diffraction is an important dispersive phenomenon, which has been widely used, for example, the dispersive gratings in

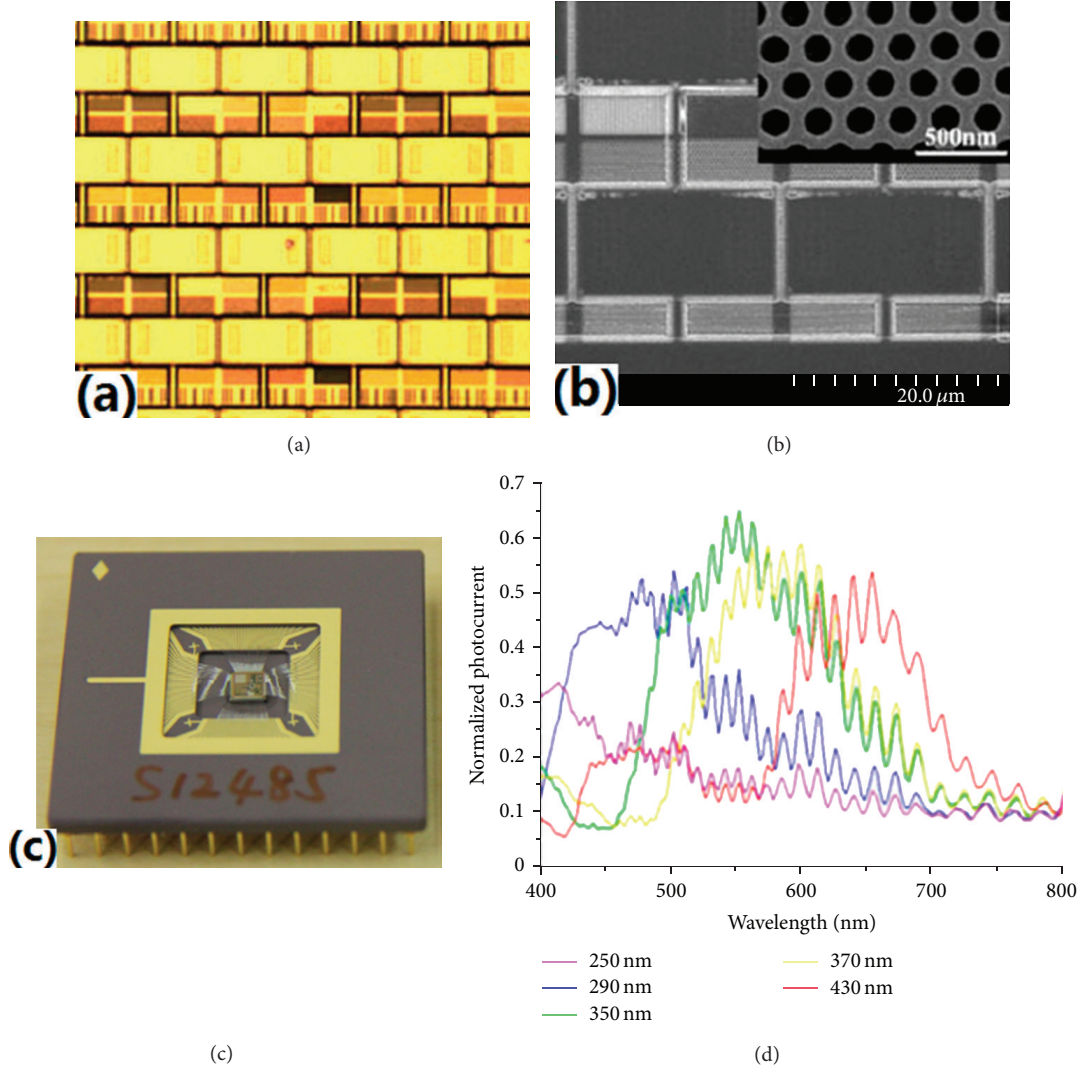


FIGURE 13: Surface plasmon enhanced CIS. (a) Microscope image and (b) SEM image of the patterned pixel array. (c) Microscope image of the packaged CIS. (d) The measured photocurrent from different pixels [18].

spectral measurement. The diffraction angle θ depends on the wavelength λ and the grating period p by the Bragg law:

$$p \cdot \sin \theta = \frac{m \cdot \lambda}{2}, \quad (3)$$

where m is an integer that stands for the diffraction order. Light at different wavelengths can be diffracted to different directions determined by the grating period. When the diffraction gratings are brought into contact with a waveguide, the diffracted light can be coupled with a guided mode when the wavevector matching condition is matched:

$$\beta = \frac{2\pi}{p}, \quad (4)$$

where β is the propagation constant of the guided mode. The coupling results in GMR that can be used for color filtering [45–58]. Kaplan et al. proposed a GMR transmissive color filter with a buffer layer between the metallic gratings and

the waveguide layer [51], where the buffer layer reduces the overlap of the guided mode and the metal to reduce the absorption loss. As a result, the transmission is much higher than other structural filters and the passband is very narrow as shown in Figure 9. GMR effect can also be used in reflective color filters, where dielectric gratings are usually used to provide the coupling between the reflected diffraction and the waveguide mode. Uddin and Magnusson demonstrated such a reflective color filter by fabricating Si_3N_4 gratings on a glass slide as shown in Figure 10 [57]. However, this structure is very sensitive to the incident angle due to the diffraction effect. The reflected light changes from blue to red when the viewing angle moves from 7° to 42° .

2.4. Photonic Crystal (PhC) Color Filters. PhC is a structure with subwavelength periodic refractive index variation, which has been applied to optical fiber [59], laser [60], microwave antenna [61], color filter [62], and so forth. As

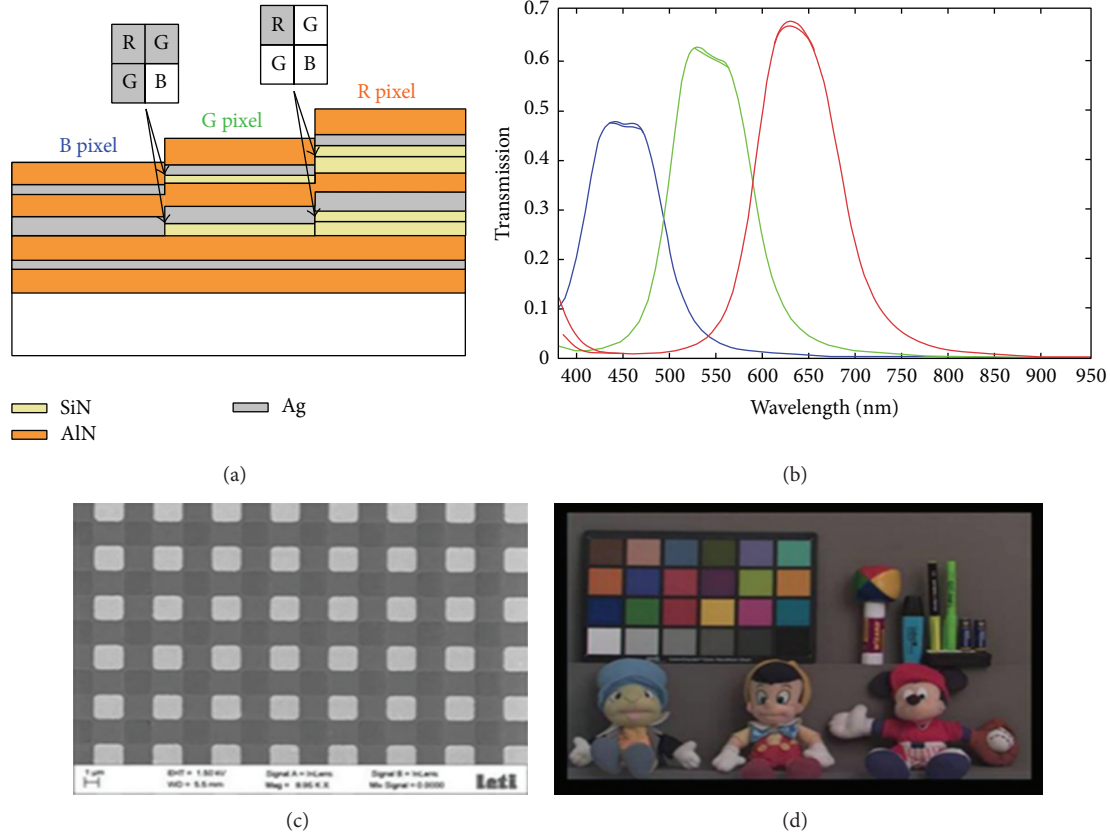


FIGURE 14: CIS using MIM color filters. (a) Schematic of the MIM color filters. (b) Simulated spectra. (c) SEM image of the pixel array. (d) A color image recorded by this CIS [38].

the electron energy band in solid state physics, photonic band can be engineered by modifying the structure of PhC [63–65]. One-dimensional PhC is a perfect reflector with the lowpass band. If a defect layer is introduced, a defect energy level appears in the bandgap, that is, a passband [51, 56, 57]. Figure 11 shows a transmission PhC color filter [62]. We can see that a 70% transmission peak with a very narrow bandwidth shows in the energy band of PhC. With optimization, if a single transmission peak can be achieved in the visible band, we can have a very high color purity and brightness. By etching holes with different sizes as the etalon color filters above, the passband can also be tuned.

2.5. Color Routing by Scattering. Light scattering usually occurs when light spreads through inhomogeneous medium. Part of light deviates from original direction with the deviation angle depending on the wavelength. Scattering from both metallic and dielectric scatters shows dispersive behavior [66–68]. Recently, Küll proposed a gold-silver disk pair for color routing as shown in Figure 12, where the phase accumulation through material-dependent plasmon resonances induces fantastic optical properties, that is, scattering red and blue light in opposite directions. This color routing device is as small as $\lambda^3/100$ [66]. It is very attractive for high-resolution imaging, but the light scattering efficiency is quite low. A dielectric light deflector of a SiN_x bar as small

as 280 nm was reported recently for color routing in a CMOS image sensor by Panasonic [68]. The large refractive index contrast between the deflector and the surrounding material induces a near-field deflection with a strong dispersion (Figure 15). One of the most important advantages of the scattering color routing is that almost all energy in the spectral band is used for colorful imaging. In contrast, there is reflection/transmission loss for the transmissive/reflective color filters based on nanohole array, GMR, and MIM techniques.

3. Applications

3.1. CMOS Image Sensors (CIS). CIS are the leading mass-market technology for digital imaging. Conventional color filtering technique for CIS uses pigment or dye filters [69]. However, these polymer based color filters cannot sustain heat and radiation. Furthermore, each color filter for red, green, and blue on the pixel arrays must be fabricated step by step with accurate alignment. Therefore, structural color filters, whose performance is based on the stable metal or dielectric subwavelength structures, are very attractive. Various color filters can be fabricated using the same material and in a single lithography step.

As shown in Figure 13, we fabricated metallic nanohole array color filters on top of the pixel array of CIS and

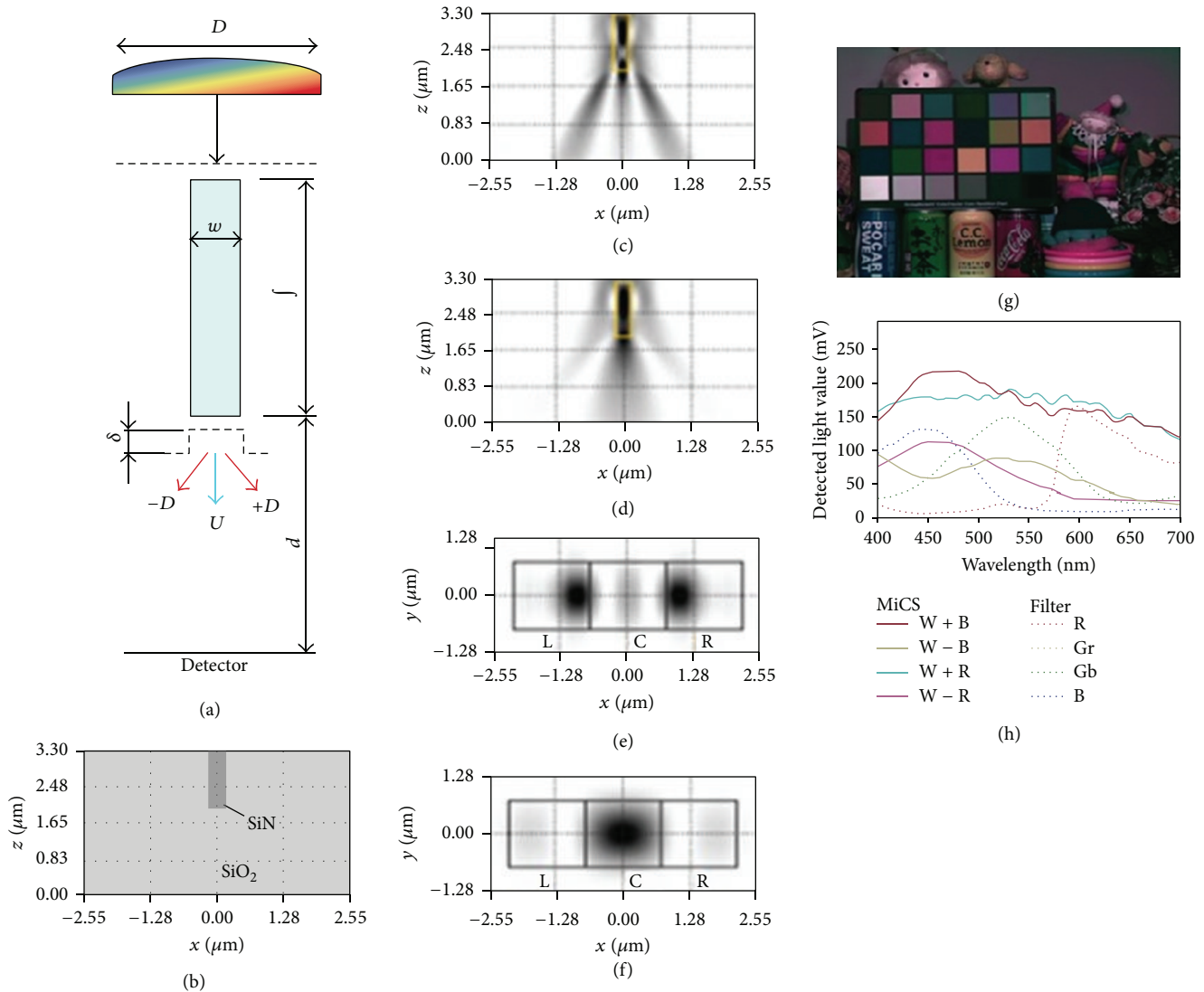


FIGURE 15: CIS based on scattering color. Left: SiN_x bar deflector; right: detected light signals from different pixels and the recorded image [68].

demonstrate the potential imaging function by measuring the photocurrent response from separated pixels [18]. The results agree with the design quite well and the distinct color filtering is achieved. For the pixels with hole arrays with period of 250 nm–430 nm, the photocurrents show intensity peaks of 450 nm–650 nm. Although the metallic hole array was fabricated by EBL directly on top of the CIS chip, the full CMOS integration of these color filters in the metal interconnect layers can be readily achieved by the state-of-the-art CMOS technologies. CEA and STM Electronics demonstrated this idea using the MIM resonator color filters [38]. And a 300 M-pixel CIS with full functions was demonstrated as seen in Figure 14. Because the MIM resonator color filter has to use space layers with different thicknesses for different colors, multistep lithography process was used. In 2013, Panasonic Ltd. presented a CIS with a pixel size as small as $1.43 \mu\text{m} \times 1.43 \mu\text{m}^2$, in which a 280 nm wide SiN bar was used as the light scatter to direct incident light as

shown in Figure 15 [68]. As discussed in the previous section, the scattering technique for color routing suffers very little light reflection/transmission loss. 1.85 times improvement of the amount of light received by each pixel was achieved.

3.2. Colorful Solar Cells. As introduced in Section 2, sub-wavelength metallic gratings can reflect light in different colors. When these gratings are integrated in solar cells, the transmitted light is absorbed in the active layer and converted into charge, but the reflected light shows color. By attaching these colorful solar cells on the walls and roofs of the buildings, they provide both decoration and power. It is also photovoltaic color filters, which can be used in self-powering electric display device. Park et al. demonstrated this idea in an organic solar cell [70]. As shown in Figure 16, the P3HT:PCBM photoactive layer is sandwiched by an Au nanograting layer and a continuous

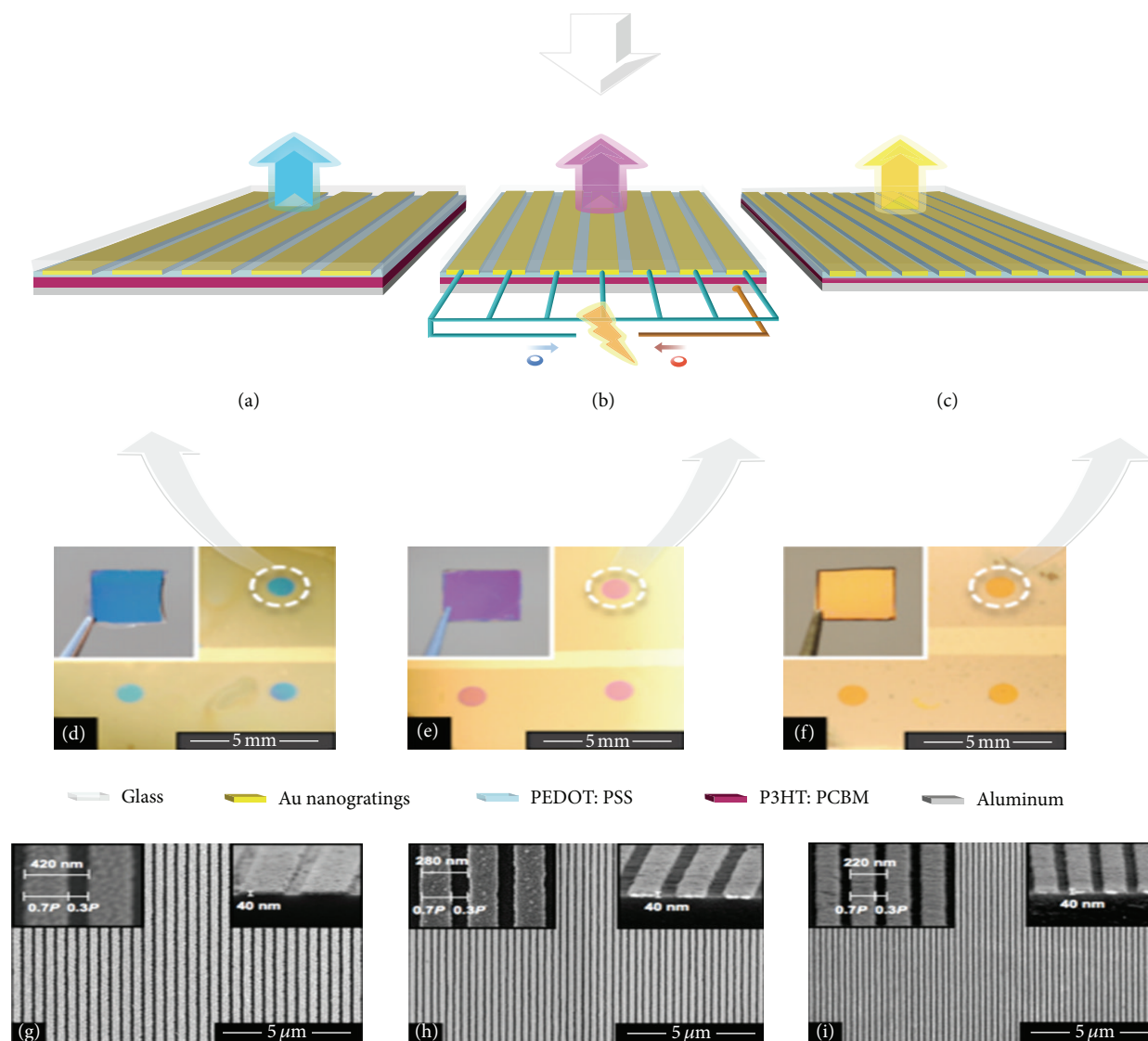


FIGURE 16: Colorful solar cells with the metallic gratings integrated with the organic active material [70].

Al film. The Au nanogratings are used as semitransparent electrodes for the solar cells and reflect light in different colors. Meanwhile, spectral engineering of light transmission for the transparent solar cells (TSCs) allows us to achieve more aesthetically pleasing indoor lighting with the multicolored solar windows. Transmissive colorful solar cells were developed by integrating MIM resonant color filters in Figure 17(a) [71]. As shown in Figure 17(b), by tuning the relative layer thickness of the MIM stacks, narrow-band coloring can be achieved for the TSCs. Efficiency of 5% on average was obtained for the colored TSCs, but at the expense of a rather limited luminosity. Lee et al. presented an ultrathin undoped amorphous silicon/organic hybrid solar cell structure [72]. The simple diagram of the structure can be seen in Figure 18(a). To achieve color tunability, inorganic absorbing layers with 6 nm, 11 nm, and 31 nm were selected to produce blue, green, and red cells. The structures show that the transmissive spectra have great angle insensitivity

in Figures 18(b)–18(g). Although, monochromatic coloring and near unity internal quantum efficiency were obtained, their efficiencies were significantly undermined by the poor light-harvesting capacity for such ultrathin absorbing layers. Actually, the metallic gratings can be used to tune the absorption spectrum of solar cell and achieve a significant improvement of the absorption due to effects such as LSPR, GMR, and FP resonance [73].

3.3. Colorful OLED Display. Although colorful OLEDs can be obtained by using different electroluminescence (EL) materials, the intrinsic emission spectra of EL materials are not narrow enough for high purity colorful display. Furthermore, different EL materials have to be used in display to generate the full color, which needs multiple lithography process like the pigment color filters in CIS. The combination of white OLED and color filters has lower cost and higher

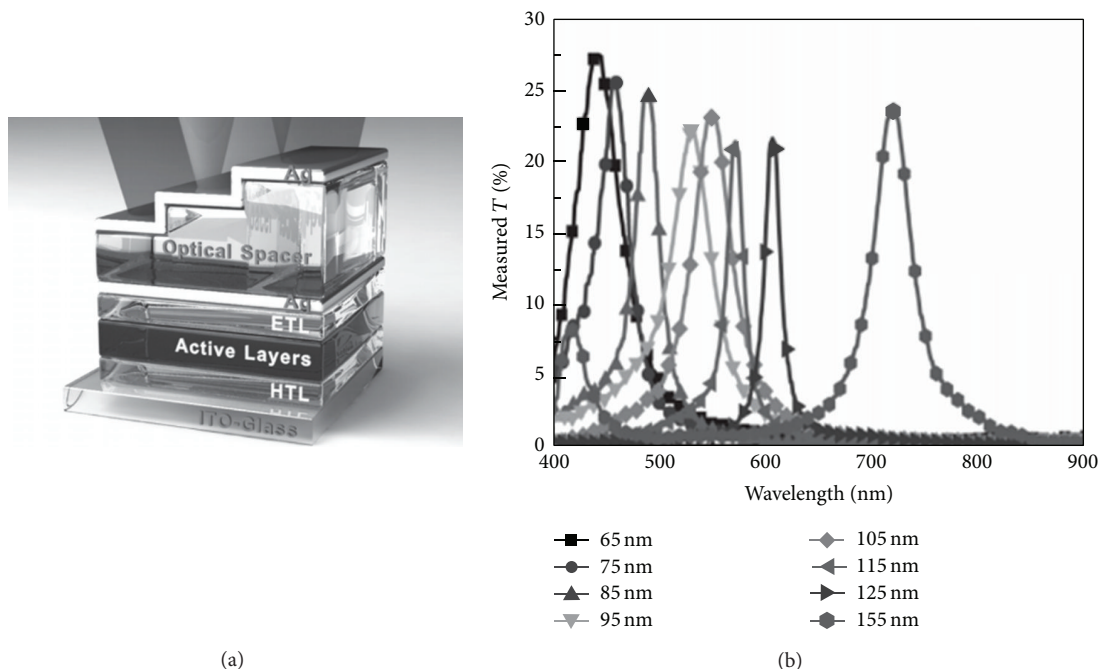


FIGURE 17: (a) Device architecture of MIM transmissive solar cell. (b) The measured transmissive spectra [71].

yield. In order to improve the purity of the color, many researchers have engaged in OLED with different types of color filters. For example, both one dimensional metal slits and two dimensional nanoholes have been theoretically and experimentally demonstrated [74, 75]. A narrow band and high transmission can be achieved by changing the parameter of the color filters, making these types of color filters have potential advantages in OLED display. As shown in Figure 19, in the color filters, distributed Bragg reflector acts as the half mirror; IZO/ITO and SiN_x are used as the optical filler to tune the color [76]. By integrating the structures at the emitting surface of the OLED, a set of colorful OLEDs were achieved. Photograph of a display fabricated with this design clearly shows the excellent color performance.

4. Discussion

From the above, we can see that structural color filters have attracted extensive interest from both academia and industry due to advantages such as high resistance, high stability, high compactness, tunability, low loss, and functionalities. There are also issues to be addressed before the massive applications. First, high resolution, high throughput, and low cost fabrication techniques of structure colors need to be developed. Because of the short wavelength of the visible light, the structural colors are usually based on sub- μm structures, which is a challenge for current microfabrication techniques. Nanoimprint and interference lithography could be an answer to this issue. Second, overall optimization of light efficiency, cross-talk, and angle insensitivity need to be considered. Metallic hole array shows low transmission;

GMR has strong angle dependence; scattering has a significant cross-talk; MIM and PhC also suffer angle sensitivity. Third, there are integration issues of structural color filters, for example, metal loss and compatibility with the industrial processes. Advanced fabrication technology, new photonic mechanism, and novel device design would be developed to address these issues.

5. Summary and Outlook

We review the recent development of transmissive/reflective structural color techniques including nanohole array, MIM resonator, GMR effect, photonic crystal, and light scattering. Mechanisms and performances of various structural color filters are presented, together with the integrated applications in CIS, display, solar cells, and OLEDs. The results are promising and some prototype devices have been achieved. We consider that these structural color filters still have a long way to go before extensive commercialization. The next step for the research will focus on improving the transmission/reflection efficiency, reducing the bandwidth, suppressing the angular dependence, and so forth. High throughput and low cost fabrication technologies are also required. We believe structural color filters can be more extensively applied in our life.

Conflict of Interests

The authors declare that there is no conflict of interests regarding the publication of this paper.

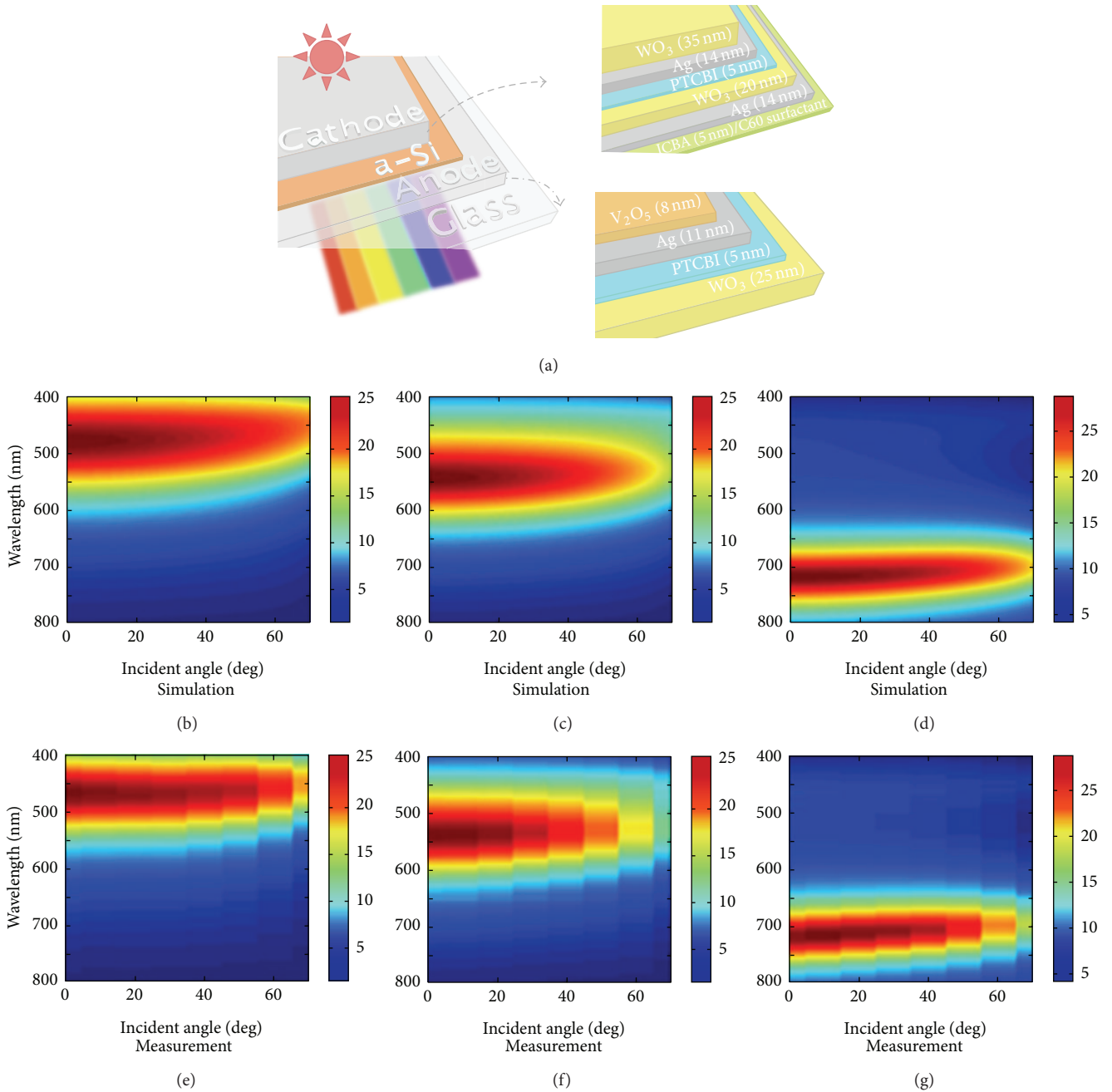


FIGURE 18: (a) Schematic of the angle insensitive structure. (b)–(d) and (e)–(g) are the simulated and measured relationship between incident angle and transmission [72].

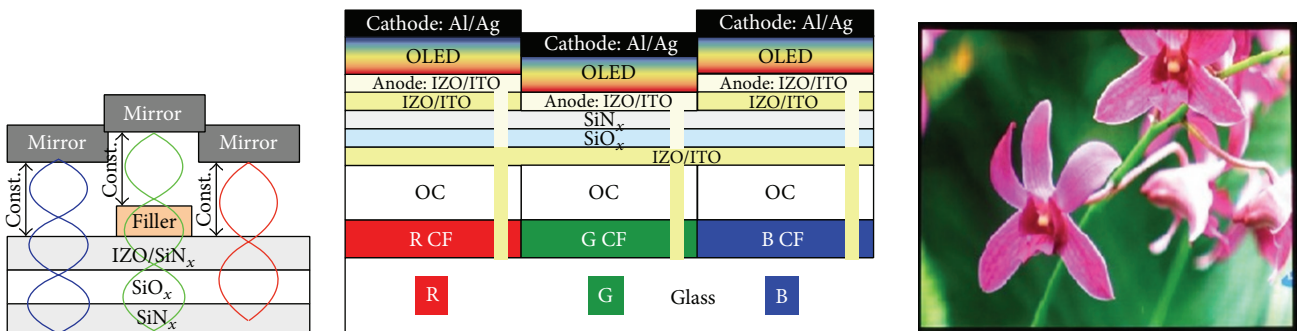


FIGURE 19: Microcavity embedded RGBW bottom-emitting AMOLED and the photograph of a display fabricated with the design [76].

Acknowledgments

This work is supported by Grants from the National Natural Science Foundation of China (no. 11274344), the Hundred Talents Program of the Chinese Academy of Sciences, the Scientific Research Foundation for the Returned Overseas Chinese Scholars, the State Education Ministry, and the Fundamental Research Project of Shenzhen Science and Technology Foundation (no. JC201105180781A).

References

- [1] H. Koo, M. Chen, and P. Pan, "LCD-based color filter films fabricated by a pigment-based colorant photo resist inks and printing technology," *Thin Solid Films*, vol. 515, no. 3, pp. 896–901, 2006.
- [2] M. C. Gather, A. Köhnen, A. Falcou, H. Becker, and K. Meerholz, "Solution-processed full-color polymer organic light-emitting diode displays fabricated by direct photolithography," *Advanced Functional Materials*, vol. 17, no. 2, pp. 191–200, 2007.
- [3] T. Xu, H. Shi, Y. Wu, A. F. Kaplan, J. G. Ok, and L. J. Guo, "Structural colors: from plasmonic to carbon nanostructures," *Small*, vol. 7, no. 22, pp. 3128–3136, 2011.
- [4] J. J. Cowan, "Aztec surface-relief volume diffractive structure," *Journal of the Optical Society of America A*, vol. 7, no. 8, pp. 1529–1544, 1990.
- [5] T. W. Ebbesen, H. J. Lezec, H. F. Ghaemi, T. Thio, and P. A. Wolff, "Extraordinary optical transmission through sub-wavelength hole arrays," *Nature*, vol. 391, no. 6668, pp. 667–669, 1998.
- [6] H. A. Bethe, "Theory of diffraction by small holes," *Physical Review*, vol. 66, no. 7-8, pp. 163–182, 1944.
- [7] H. F. Ghaemi, T. Thio, D. E. Grupp, T. W. Ebbesen, and H. J. Lezec, "Surface plasmons enhance optical transmission through subwavelength holes," *Physical Review B. Condensed Matter and Materials Physics*, vol. 58, no. 11, pp. 6779–6782, 1998.
- [8] J. A. Porto, E. J. García-Vidal, and J. B. Pendry, "Transmission resonances on metallic gratings with very narrow slits," *Physical Review Letters*, vol. 83, no. 14, pp. 2845–2848, 1999.
- [9] M. N. E. Popov, S. Enoch, and R. Reinisch, "Theory of light transmission through subwavelength periodic hole arrays," *Physical Review B*, vol. 62, Article ID 16100, 2000.
- [10] Q. Cao and P. Lalanne, "Negative role of surface plasmons in the transmission of metallic gratings with very narrow slits," *Physical Review Letters*, vol. 88, no. 5, Article ID 057403, 2002.
- [11] K. Walls, Q. Chen, S. Collins, D. R. S. Cumming, and T. D. Drysdale, "Automated design, fabrication, and characterization of color matching plasmonic filters," *IEEE Photonics Technology Letters*, vol. 24, no. 7, pp. 602–604, 2012.
- [12] H. Lee, Y. Yoon, S. Lee, S. Kim, and K. Lee, "Color filter based on a subwavelength patterned metal grating," *Optics Express*, vol. 15, no. 23, pp. 15457–15463, 2007.
- [13] W. Li and S. Y. Chou, "Solar-blind deep-UV band-pass filter (250–350 nm) consisting of a metal nano-grid fabricated by nanoimprint lithography," *Optics Express*, vol. 18, no. 2, pp. 931–937, 2010.
- [14] Q. Chen and D. R. S. Cumming, "High transmission and low color cross-talk plasmonic color filters using triangular-lattice hole arrays in aluminum films," *Optics Express*, vol. 18, no. 13, pp. 14056–14062, 2010.
- [15] D. Inoue, A. Miura, T. Nomura et al., "Polarization independent visible color filter comprising an aluminum film with surface-plasmon enhanced transmission through a subwavelength array of holes," *Applied Physics Letters*, vol. 98, no. 9, Article ID 093113, 2011.
- [16] G. Si, Y. Zhao, H. Liu et al., "Annular aperture array based color filter," *Applied Physics Letters*, vol. 99, no. 3, Article ID 033105, 2011.
- [17] Q. Chen, D. Chitnis, K. Walls, T. D. Drysdale, S. Collins, and D. R. S. Cumming, "CMOS photodetectors integrated with plasmonic color filters," *IEEE Photonics Technology Letters*, vol. 24, no. 3, pp. 197–199, 2012.
- [18] Q. Chen, D. Das, D. Chitnis et al., "A CMOS image sensor integrated with plasmonic colour filters," *Plasmonics*, vol. 7, no. 4, pp. 695–699, 2012.
- [19] F. Przybilla, A. Degiron, C. Genet et al., "Efficiency and finite size effects in enhanced transmission through subwavelength apertures," *Optics Express*, vol. 16, no. 13, pp. 9571–9579, 2008.
- [20] S. Yokogawa, S. P. Burgos, and H. A. Atwater, "Plasmonic color filters for CMOS image sensor applications," *Nano Letters*, vol. 12, no. 8, pp. 4349–4354, 2012.
- [21] S. P. Burgos, S. Yokogawa, and H. A. Atwater, "Color imaging via nearest neighbor hole coupling in plasmonic color filters integrated onto a complementary metal-oxide semiconductor image sensor," *Acs Nano*, vol. 7, no. 11, pp. 10038–10047, 2013.
- [22] D. van Labeke, D. Gérard, B. Guizal, F. I. Baida, and F. Li, "An angle-independent frequency selective surface in the optical range," *Optics Express*, vol. 14, no. 25, pp. 11945–11951, 2006.
- [23] S. Y. Chou, P. R. Krauss, and P. J. Renstrom, "Nanoimprint lithography," *Journal of Vacuum Science and Technology B: Microelectronics and Nanometer Structures*, vol. 14, no. 6, pp. 4129–4133, 1996.
- [24] Q. Chen, G. Hubbard, P. A. Shields et al., "Broadband moth-eye antireflection coatings fabricated by low-cost nanoimprinting," *Applied Physics Letters*, vol. 94, no. 26, Article ID 263118, 2009.
- [25] G. Hubbard, S. J. Abbott, Q. Chen et al., "Wafer-scale transfer of nanoimprinted patterns into silicon substrates," *Physica E: Low-Dimensional Systems and Nanostructures*, vol. 41, no. 6, pp. 1118–1121, 2009.
- [26] Q. Chen, C. Martin, and D. R. S. Cumming, "Transfer printing of nanoplasmonic devices onto flexible polymer substrates from a rigid stamp," *Plasmonics*, vol. 7, no. 4, pp. 755–761, 2012.
- [27] J. L. Skinner, A. A. Talin, and D. A. Horsley, "A MEMS light modulator based on diffractive nanohole gratings," *Optics Express*, vol. 16, no. 6, pp. 3701–3711, 2008.
- [28] L. Lin and A. Roberts, "Angle-robust resonances in cross-shaped aperture arrays," *Applied Physics Letters*, vol. 97, no. 6, Article ID 061109, 2010.
- [29] K. Kumar, H. Duan, R. S. Hegde, S. C. W. Koh, J. N. Wei, and J. K. W. Yang, "Printing colour at the optical diffraction limit," *Nature Nanotechnology*, vol. 7, no. 9, pp. 557–561, 2012.
- [30] Z. Ye, J. Zheng, S. Sun, L. Guo, and H. D. Shieh, "Compact transreflective color filters and polarizers by bilayer metallic nanowire gratings on flexible substrates," *IEEE Journal on Selected Topics in Quantum Electronics*, vol. 19, no. 3, pp. 4800205–4800209, 2013.
- [31] A. S. Roberts, A. Pors, O. Albrechtsen, and S. I. Bozhevolnyi, "Subwavelength plasmonic color printing protected for ambient use," *Nano Letters*, vol. 14, no. 2, pp. 783–787, 2014.
- [32] S. Song, Q. Chen, L. Jin, and F. Sun, "Great light absorption enhancement in a graphene photodetector integrated with a

- metamaterial perfect absorber,” *Nanoscale*, vol. 5, no. 20, pp. 9615–9619, 2013.
- [33] Q. Chen, F. Sun, and S. Song, “Subcell misalignment in vertically cascaded metamaterial absorbers,” *Optics Express*, vol. 21, no. 13, pp. 15896–15903, 2013.
- [34] W. Cai, U. K. Chettiar, H. Yuan et al., “Metamagnetics with rainbow colors,” *Optics Express*, vol. 15, no. 6, pp. 3333–3341, 2007.
- [35] Z. Wu, D. Lee, M. F. Rubner, and R. E. Cohen, “Structural color in porous, superhydrophilic, and self-cleaning $\text{SiO}_2/\text{TiO}_2$ bragg stacks,” *Small*, vol. 3, no. 8, pp. 1445–1451, 2007.
- [36] Y.-T. Yoon and S.-S. Lee, “Transmission type color filter incorporating a silver film based etalon,” *Optics Express*, vol. 18, no. 5, pp. 5344–5349, 2010.
- [37] T. Xu, Y. Wu, X. Luo, and L. J. Guo, “Plasmonic nanoresonators for high-resolution colour filtering and spectral imaging,” *Nature Communications*, vol. 1, pp. 59–63, 2010.
- [38] L. Frey, P. Parrein, J. Raby et al., “Color filters including infrared cut-off integrated on CMOS image sensor,” *Optics Express*, vol. 19, no. 14, pp. 13073–13080, 2011.
- [39] K. Walls, Q. Chen, J. Grant, S. Collins, D. R. S. Cumming, and T. D. Drysdale, “Narrowband multispectral filter set for visible band,” *Optics Express*, vol. 20, no. 20, pp. 21917–21923, 2012.
- [40] C. M. Wang, Y. C. Chang, M. W. Tsai et al., “Angle-independent infrared filter assisted by localized surface plasmon polariton,” *IEEE Photonics Technology Letters*, vol. 20, no. 13, pp. 1103–1105, 2008.
- [41] A. F. Kaplan, T. Xu, Y. Wu, and L. J. Guo, “Multilayer pattern transfer for plasmonic color filter applications,” *Journal of Vacuum Science and Technology B: Microelectronics and Nanometer Structures*, vol. 28, no. 6, Article ID C6O60, 2010.
- [42] Q. Chen and D. R. S. Cumming, “Visible light focusing demonstrated by plasmonic lenses based on nano-slits in an aluminum film,” *Optics Express*, vol. 18, no. 14, pp. 14762–14767, 2010.
- [43] Q. Chen, “Effect of the number of zones in a one-dimensional plasmonic zone plate lens: simulation and experiment,” *Plasmonics*, vol. 6, no. 1, pp. 75–82, 2011.
- [44] Q. Chen, “A Novel Plasmonic Zone Plate Lens Based on Nano-Slits with Refractive Index Modulation,” *Plasmonics*, vol. 6, no. 2, pp. 381–385, 2011.
- [45] W. Nakagawa, P. Sun, C. Chen, and Y. Fainman, “Wide-field-of-view narrow-band spectral filters based on photonic crystal nanocavities,” *Optics Letters*, vol. 27, no. 3, pp. 191–193, 2002.
- [46] A. Mehta, R. C. Rumpf, Z. Roth, and E. G. Johnson, “Nanofabrication of a space-variant optical transmission filter,” *Optics Letters*, vol. 31, no. 19, pp. 2903–2905, 2006.
- [47] S. S. Wang and R. Magnusson, “Theory and applications of guide-mode resonance filters,” *Applied Optics*, vol. 32, no. 14, pp. 2606–2613, 1993.
- [48] Y. Kanamori, M. Shimono, and K. Hane, “Fabrication of transmission color filters using silicon subwavelength gratings on quartz substrates,” *IEEE Photonics Technology Letters*, vol. 18, no. 20, pp. 2126–2128, 2006.
- [49] Y. T. Yoon, H. S. Lee, S. S. Lee, S. H. Kim, J. D. Park, and K. Lee, “Color filter incorporating a subwavelength patterned grating in poly silicon,” *Optics Express*, vol. 16, no. 4, pp. 2374–2380, 2008.
- [50] B. Luk’Yanchuk, N. I. Zheludev, S. A. Maier et al., “The Fano resonance in plasmonic nanostructures and metamaterials,” *Nature Materials*, vol. 9, no. 9, pp. 707–715, 2010.
- [51] A. F. Kaplan, T. Xu, and L. Jay Guo, “High efficiency resonance-based spectrum filters with tunable transmission bandwidth fabricated using nanoimprint lithography,” *Applied Physics Letters*, vol. 99, no. 14, Article ID 143111, 2011.
- [52] K. Kintaka, T. Majima, J. Inoue, K. Hatanaka, J. Nishii, and S. Ura, “Cavity-resonator-integrated guided-mode resonance filter for aperture miniaturization,” *Optics Express*, vol. 20, no. 2, pp. 1444–1449, 2012.
- [53] I. R. Mckerracher, L. Fu, H. H. Tan, and C. Jagadish, “Integration of bandpass guided-mode resonance filters with mid-wavelength infrared photodetectors,” *Journal of Physics D: Applied Physics*, vol. 46, no. 9, Article ID 095104, 2013.
- [54] I. D. Block, M. Pineda, C. J. Choi, and B. T. Cunningham, “High sensitivity plastic-substrate photonic crystal biosensor,” *IEEE Sensors Journal*, vol. 8, no. 9–10, pp. 1546–1547, 2008.
- [55] S. S. Wang, R. Magnusson, J. S. Bagby, and M. G. Moharam, “Guided-mode resonances in planar dielectric-layer diffraction gratings,” *Journal of the Optical Society of America A: Optics Image Science and Vision*, vol. 7, no. 8, pp. 1470–1474, 1990.
- [56] N. Nguyen-Huu, Y.-L. Lo, and Y.-B. Chen, “Color filters featuring high transmission efficiency and broad bandwidth based on resonant waveguide-metallic grating,” *Optics Communications*, vol. 284, no. 10–11, pp. 2473–2479, 2011.
- [57] M. J. Uddin and R. Magnusson, “Efficient guided-mode-resonant tunable color filters,” *IEEE Photonics Technology Letters*, vol. 24, no. 17, pp. 1552–1554, 2012.
- [58] D. Rosenblatt, A. Sharon, and A. A. Friesem, “Resonant grating waveguide structures,” *IEEE Journal of Quantum Electronics*, vol. 33, no. 11, pp. 2038–2059, 1997.
- [59] J. C. Knight, “Photonic crystal fibres,” *Nature*, vol. 424, no. 6950, pp. 847–851, 2003.
- [60] H. Matsubara, S. Yoshimoto, H. Saito, Y. Jianglin, Y. Tanaka, and S. Noda, “GaN photonic-crystal surface-emitting laser at blue-violet wavelengths,” *Science*, vol. 319, no. 5862, pp. 445–447, 2008.
- [61] E. R. Brown, C. D. Parker, and E. Yablonovitch, “Radiation properties of a planar antenna on a photonic-crystal substrate,” *Journal of the Optical Society of America B: Optical Physics*, vol. 10, no. 2, pp. 404–407, 1993.
- [62] G. Shambat, R. Athale, G. Euliss, M. Mirotznik, E. Johnson, and V. Smolski, “Reconfigurable photonic crystal filters for multi-band optical filtering on a monolithic substrate,” in *Proceedings of SPIE Nanostructured Thin Films*, vol. 7041, pp. 70410P1–70410P12, 2008.
- [63] Q. Chen, M. D. Archbold, and D. W. E. Allsopp, “Design of ultrahigh-Q 1-D photonic crystal microcavities,” *IEEE Journal of Quantum Electronics*, vol. 45, no. 3, pp. 233–239, 2009.
- [64] Q. Chen and D. W. E. Allsopp, “Group velocity delay in coupled-cavity waveguides based on ultrahigh-Q cavities with Bragg reflectors,” *Journal of Optics A: Pure and Applied Optics*, vol. 11, no. 5, Article ID 054010, 2009.
- [65] Q. Chen and D. W. E. Allsopp, “One-dimensional coupled cavities photonic crystal filters with tapered Bragg mirrors,” *Optics Communications*, vol. 281, no. 23, pp. 5771–5774, 2008.
- [66] T. Shegai, S. Chen, V. D. Miljković, G. Zengin, P. Johansson, and M. Käll, “A bimetallic nanoantenna for directional colour routing,” *Nature Communications*, vol. 2, no. 1, article 481, 2011.
- [67] S. H. A. Lavasani and T. Pakizeh, “Color-switched directional ultracompact optical nanoantennas,” *Journal of the Optical Society of America B: Optical Physics*, vol. 29, no. 6, pp. 1361–1366, 2012.

- [68] S. Nishiwaki, T. Nakamura, M. Hiramoto, T. Fujii, and M. Suzuki, "Efficient colour splitters for high-pixel-density image sensors," *Nature Photonics*, vol. 7, no. 3, pp. 240–246, 2013.
- [69] Y. Huo, C. C. Fesenmaier, and P. B. Catrysse, "Microlens performance limits in sub- $2\mu\text{m}$ pixel CMOS image sensors," *Optics Express*, vol. 18, no. 6, pp. 5861–5872, 2010.
- [70] H. J. Park, T. Xu, J. Y. Lee, A. Ledbetter, and L. J. Guo, "Photonic color filters integrated with organic solar cells for energy harvesting," *ACS Nano*, vol. 5, no. 9, pp. 7055–7060, 2011.
- [71] Y. H. Chen, C. W. Chen, Z. Y. Huang et al., "Microcavity-embedded, colour-tuneable, transparent organic solar cells," *Advanced Materials*, vol. 26, no. 7, pp. 1129–1134, 2014.
- [72] J. Y. Lee, K. T. Lee, S. Seo, and L. J. Guo, "Decorative power generating panels creating angle insensitive transmissive colors," *Scientific Reports*, vol. 4, pp. 4192–4197, 2014.
- [73] L. Wen, F. Sun, and Q. Chen, "Cascading metallic gratings for broadband absorption enhancement in ultrathin plasmonic solar cells," *Applied Physics Letters*, vol. 104, no. 15, Article ID 151106, 2014.
- [74] X. Hu, L. Zhan, and Y. Xia, "Color filters based on enhanced optical transmission of subwavelength-structured metallic film for multicolor organic light-emitting diode display," *Applied Optics*, vol. 47, no. 23, pp. 4275–4279, 2008.
- [75] Y. Qiu, L. Zhan, X. Hu, S. Luo, and Y. Xia, "Demonstration of color filters for OLED display based on extraordinary optical transmission through periodic hole array on metallic film," *Displays*, vol. 32, no. 5, pp. 308–312, 2011.
- [76] B. W. Lee, Y. I. Hwang, H. Y. Lee, C. W. Kim, and Y. G. Ju, "Micro-cavity design of RGBW AMOLED for 100% color gamut," in *Proceedings of the 2008 Sid International Symposium, Digest of Technical Papers*, vol. 39, pp. 1050–1053, Books I–III, 2008.

Research Article

Optical Amplification at 1525 nm in BaYF₅: 20% Yb³⁺, 2% Er³⁺ Nanocrystals Doped SU-8 Polymer Waveguide

Pengcheng Zhao, Meiling Zhang, Tianjiao Wang, Xinyang Liu, Xuesong Zhai, Guanshi Qin, Weiping Qin, Fei Wang, and Daming Zhang

State Key Laboratory on Integrated Optoelectronics, College of Electronic Science and Engineering, Jilin University, Changchun 130012, China

Correspondence should be addressed to Fei Wang; wang_fei@jlu.edu.cn

Received 25 February 2014; Accepted 3 April 2014; Published 3 June 2014

Academic Editor: Tong Zhang

Copyright © 2014 Pengcheng Zhao et al. This is an open access article distributed under the Creative Commons Attribution License, which permits unrestricted use, distribution, and reproduction in any medium, provided the original work is properly cited.

We demonstrated optical amplification in BaYF₅: 20% Yb³⁺, 2% Er³⁺ (BYF) nanocrystals doped polymer waveguide. BYF nanocrystals with an average size of ~13 nm were synthesized by a high-boiling solvent process. Intense 1.53 μm fluorescence was obtained in the nanocrystals under excitation at 980 nm. An optical polymer waveguide was fabricated by using BYF nanocrystals doped SU-8 polymer as the core material. A relative optical gain of ~10.4 dB at 1525 nm was achieved in a 1.1 cm long waveguide for an input signal power of ~0.09 mW and a pump power of ~212 mW.

1. Introduction

Erbium doped fiber amplifier (EDFA) is considered as the most deployed fiber amplifier as its amplification window coincides with low loss telecommunication windows at 1550 nm. However, EDFAs are incompatible with miniature and integrated optical devices in access and home network applications [1, 2]. Compared to EDFAs, erbium doped waveguide amplifier (EDWA) provides a higher gain in a much smaller size waveguide rather than several meters of fiber and can be integrated with other photonic devices potentially, such as switches, couplers, and splitters [3–8]. Usually, inorganic host materials are used to fabricate EDWA. However, the use of polymeric hosts in the fabrication of EDWA gives many advantages, including low fabrication costs, simplified processing steps, and compatibility with processing techniques for patterning [8–12]. In particular, Er³⁺-doped inorganic nanocrystals can be dispersed into polymer matrices and used to construct polymer-based EDWAs [8, 9, 13, 14]. However until recently there are only a few reports on obtained optical gains based on inorganic nanocrystals doped polymeric optical waveguide amplifiers. Zhang et al. synthesized LaF₃: Er³⁺, Yb³⁺ nanocrystals and

constructed a polymer-based EDWA with an optical gain of ~5 dB [8]. Zhai et al. demonstrated a polymer-based EDWA based on NaYF₄: Er³⁺, Yb³⁺, and Ce³⁺ nanocrystals and its maximum gain was about 4 dB [15]. Very recently, sub-10 nm BaYF₅: Yb³⁺, Er³⁺ nanocrystals were synthesized and used to construct a polymer-based EDWA with an optical gain of ~6.3 dB [16]. The large gain in this device was attributed to the good dispersibility in polymer matrices and highly efficient 1.55 μm emission of BaYF₅: Yb³⁺, Er³⁺ nanocrystals. Although smaller nanocrystals provide a good redispersibility, their luminescence quantum yield is generally low due to nonradiative energy losses caused by the surface defects as well as vibrational deactivation ascribed to solvent molecules and ligands absorbed on the nanocrystals. So we consider that there exists a trade-off between the luminescence quantum yield and the dispersibility in polymer matrices, and the gain performance of the polymer-based EDWA might be improved by slightly increasing the size of BaYF₅: Yb³⁺, Er³⁺ nanocrystals owing to the reduction of surface quenching effects of the nanocrystals.

In this paper, BaYF₅: Yb³⁺, Er³⁺ nanocrystals with an average size of ~13 nm were synthesized by a high-boiling

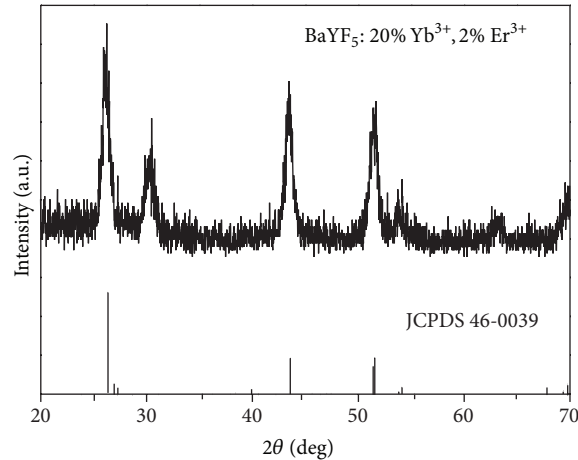


FIGURE 1: XRD pattern of the as-synthesized $\text{BaYF}_5: \text{Yb}^{3+}, \text{Er}^{3+}$ samples.

solvent process. The photoluminescence spectra were characterized. An optical polymer waveguide was fabricated by using $\text{BaYF}_5: \text{Yb}^{3+}, \text{Er}^{3+}$ nanocrystals doped SU-8 polymer as the core layer and PMMA as the coating layer. A relative optical gain of ~ 10.4 dB at 1525 nm was achieved in a 1.1 cm long waveguide for an input signal power of ~ 0.09 mW and a pump power of ~ 212 mW. To the best of our knowledge, such an optical gain is the highest one in polymer-based EDWAs with erbium doped inorganic nanocrystals ever reported.

2. Results and Discussion

$\text{BaYF}_5: \text{Yb}^{3+}, \text{Er}^{3+}$ nanocrystals were synthesized by a high-boiling solvent process. 0.5 mmol preprepared rare-earth stearate was added along with 0.5 mmol barium stearate to a 100 mL three neck round-bottom flask containing 5 mL 1-octadecene and 15 mL oleic acid. The solution was stirred magnetically and heated slowly to 100°C under vacuum for 30 min to remove residual water or oxygen. After 30 min, the reaction was brought under argon atmosphere and cooled to room temperature. A solution of NH_4F (3 mmol, 111 mg) in 10 mL of methanol was added, and then the solution was kept at 50°C for 30 min. After methanol was evaporated, the reaction was then heated to 300°C as soon as possible under an argon atmosphere, kept for 1 h, and then cooled to room temperature. The nanocrystals were precipitated with ethanol, collected after centrifugation, and redispersed in cyclohexane. The phase structure of the products was first examined by X-ray diffraction (XRD) (Model Rigaku Ru-200b), using a nickel-filtered $\text{Cu K}\alpha$ radiation ($\lambda = 1.5406 \text{ \AA}$) in the range of $10^\circ \leq 2\theta \leq 70^\circ$. Figure 1 shows the XRD pattern of the as-synthesized $\text{BaYF}_5: \text{Yb}^{3+}, \text{Er}^{3+}$ samples. The diffraction peaks of the sample can be indexed as a tetragonal-phase BaYF_5 ; the locations and relative intensity of the diffraction peaks coincide well with the literature values (JCPDS number 46-0039, space group P-421m). The size of the samples was further characterized by a JEM-2100F electron microscope at 200 kV. Figures 2(a) and 2(b) show

the transmission electron microscope (TEM) image of the as-synthesized samples and the corresponding histogram of size distribution, respectively. The as-synthesized $\text{BaYF}_5: \text{Yb}^{3+}, \text{Er}^{3+}$ samples have an average size of ~ 13 nm and a good uniformity of size.

Figure 3 shows infrared emission spectrum of $\text{BaYF}_5: \text{Yb}^{3+}, \text{Er}^{3+}$ nanocrystals at room temperature under a 980 nm laser excitation. The emission peaked at 1535 nm is assigned to the $^4\text{I}_{13/2} \rightarrow ^4\text{I}_{15/2}$ transition of Er^{3+} . The full width at half maximum of the emission is about 54 nm, which indicates a relatively wide bandwidth of the gain spectrum.

The fabrication procedure of a polymer-based waveguide is shown in Figure 4. SU-8 2005 polymer was used as the polymeric host for the fabrication of the optical waveguide. 0.005 g $\text{BaYF}_5: \text{Yb}^{3+}, \text{Er}^{3+}$ nanocrystals were dissolved into 1.8 g toluene; the solution was ultrasonically agitated for 3 h and then was mixed into SU-8 2005 polymer, and the concentration of nanocrystals in SU-8 2005 polymer was about 0.12 wt%. Waveguides of dimensions, $4 \mu\text{m}$ height by $8 \mu\text{m}$ width, were fabricated by standard photolithography and wet etching technology of a thin silicon dioxide layer. A $5 \mu\text{m}$ thick film of BYF nanocrystals doped SU-8 2005 was spin-coated onto a $2 \mu\text{m}$ thick silicon dioxide layer based on silicon substrates and prebaked at 90°C for 20 min to remove any traces of the solvent. The pattern exposure was performed at a wavelength of 365 nm using the 350 mW Hg lamp power through a contact chromium mask. The exposure time was 180 s. After postbaking, the resist was developed into propylene glycol-monomethyl ether-acetate (PGMEA) for 40 s, rinsed in isopropyl alcohol and then deionized water, and was subsequently blow-dried. A $5 \mu\text{m}$ thick P(MMA-GMA) film is spin-coated as the upper cladding layer. The refractive indices of the core and upper cladding were measured using ellipsometry method (J. A. Woollam, Co. M2000) to be 1.578 and 1.495 at 1535 nm wavelength, respectively. Figure 5 is a SEM image of the $\text{BaYF}_5: \text{Yb}^{3+}, \text{Er}^{3+}$ nanocrystals dispersed polymer rectangular waveguide amplifier (without top cladding), indicating that the size

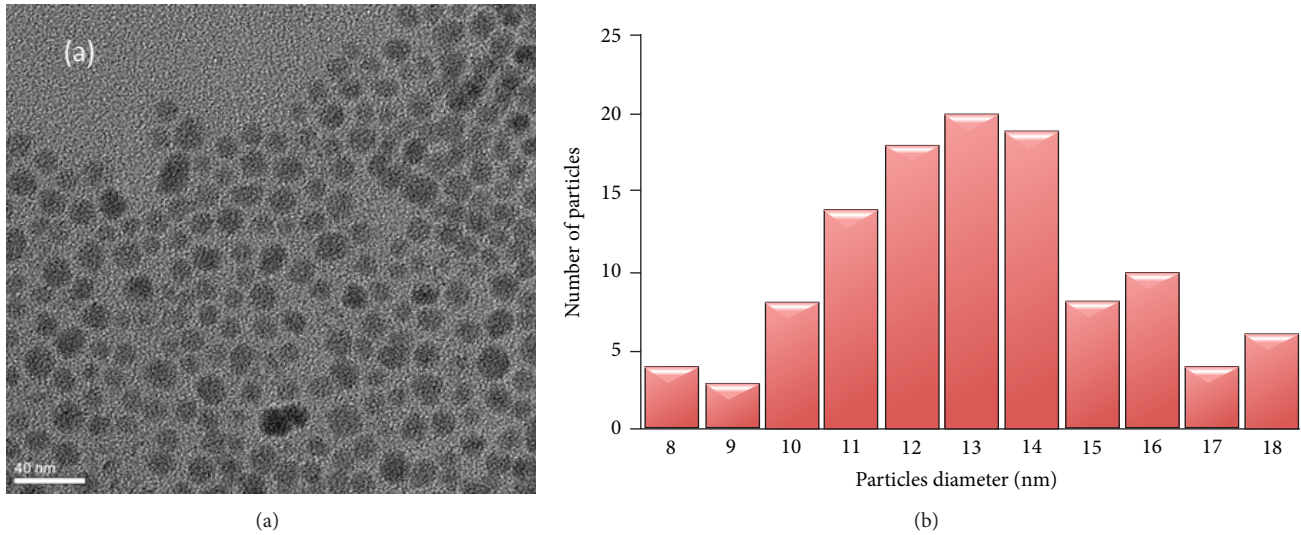


FIGURE 2: (a) A TEM image of nanocrystals, the average crystals size is about 13 nm. (b) The corresponding histogram of size distribution.

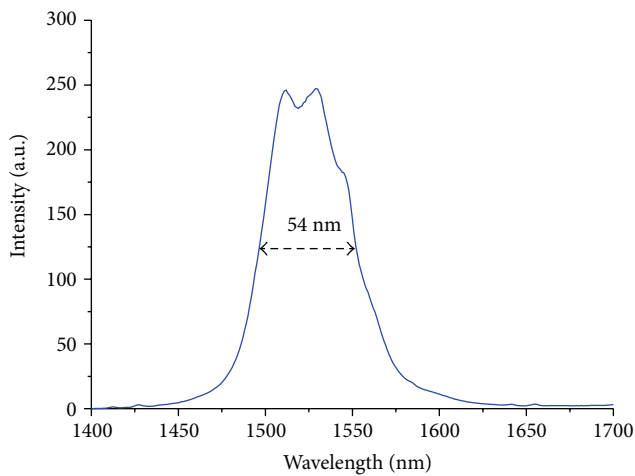


FIGURE 3: Room temperature fluorescence spectra of the nanocrystals excited under 980 nm in 0.01 M cyclohexane solutions.

of the waveguide amplifier is $8\ \mu\text{m}$ high and $4\ \mu\text{m}$ wide. Figure 6 is the output near-field profile from a 16 mm long waveguide at 1535 nm wavelength measured by using an infrared camera (Electrophysics model 7290A). The input signal power is 0.2 mW. The background loss of the waveguide with nanocrystals was also measured by using a cutback method and was about 3.1 dB/cm, which was higher than that (~ 1 dB/cm) of the waveguide without nanocrystals.

Then, we constructed a waveguide amplifier and measured their performances. Figure 7 shows the schematics of the experimental setup for the optical gain measurement. Relative gain of the waveguide amplifiers was carried out

by using a tunable laser with a working wavelength range of 1510–1590 nm (Santec TSL-210) as the signal source and a 976 nm continuous wave laser diode as the pump source. Both the pump and signal sources were coupled to the channel waveguides through a 980/1550 nm wavelength-division multiplexing fiber coupler. Output light from the device was collected and coupled to an optical spectrum analyzer (OSA, Ando AQ-6315A). The relative gain was calculated using the formula $10 \log[(P_{\text{out}} - P_{\text{ASE}})/P_{\text{in}}]$ dB, where P_{out} was the output signal power amplified by the waveguide, P_{ASE} was the amplified spontaneous emission power, and P_{in} was the input signal power. Figure 8 shows the measured gain as a function of pump power at 976 nm in a 16 mm long rectangular waveguide. The gain gradually increases with the increment of pump power. A maximum relative optical gain of ~ 10.4 dB at 1525 nm was achieved in a 1.1 cm long waveguide for an input signal power of ~ 0.09 mW and a pump power of ~ 212 mW. Such an optical gain is the highest one in polymer-based EDWAs with erbium doped inorganic nanocrystals ever reported, to the best of our knowledge. The gain coefficient of our device was also calculated based on the above measured results and was about 9.5 dB/cm [17]. Such a value is higher than that in previous published results [8, 15, 16]. We considered that such an improvement compared to previous results was obtained by investigating the trade-off between the luminescence quantum yield and the dispersibility in polymer matrices for the nanocrystals and further solving it with the optimized nanocrystals.

In addition, we measured the long time stability of the device performance under the irradiation of pump laser and found that the gain value was almost kept stable and unchanged for more than two hours. And also, we remeasured the performance of our device after two months since the fabrication of the device. The measured results showed

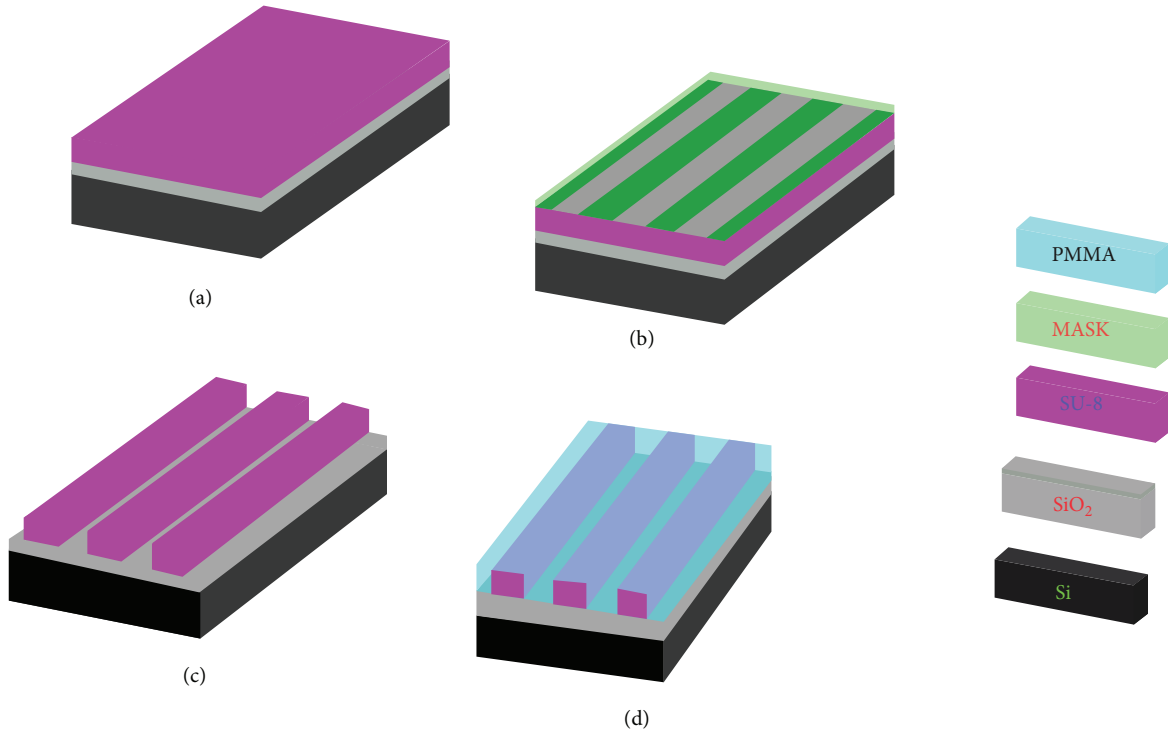


FIGURE 4: (a) Spin coating and soft bake. (b) Exposure. (c) Development and postexposure bake. (d) Spin coating top cladding and cure.

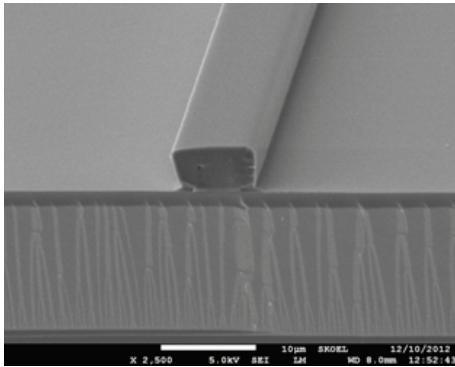


FIGURE 5: A SEM micrograph of a waveguide amplifier cross section without top cladding indicating that the size of the waveguide is $8\ \mu\text{m}$ wide and $4\ \mu\text{m}$ high.

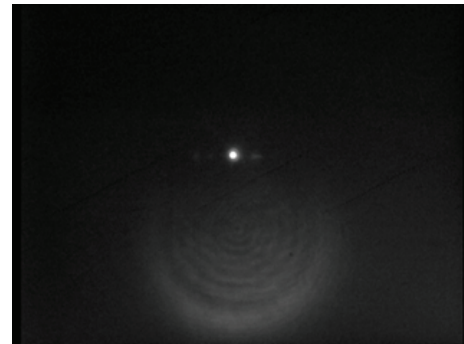


FIGURE 6: Output near-field profile from a 1.1 cm long waveguide at 1525 nm. The input signal power is 0.09 mW.

that the optical gain was not changed compared to the previous measured value.

3. Conclusions

In conclusion, we demonstrated a $\text{BaYF}_5: 20\% \text{Yb}^{3+}, 2\% \text{Er}^{3+}$ (BYF) nanocrystals doped polymer waveguide amplifier. BYF nanocrystals with an average size of $\sim 13\ \text{nm}$ were

synthesized by a high-boiling solvent process. An optical polymer waveguide was fabricated by using $\text{BaYF}_5: \text{Yb}^{3+}, \text{Er}^{3+}$ nanocrystals doped SU-8 polymer as the core layer and PMMA as the coating layer. A relative optical gain of $\sim 10.4\ \text{dB}$ at 1525 nm was achieved in a 1.1 cm long waveguide for an input signal power of $\sim 0.09\ \text{mW}$ and a pump power of $\sim 212\ \text{mW}$. Our results show that $\text{BaYF}_5: \text{Yb}^{3+}, \text{Er}^{3+}$ nanocrystals are promising candidates for building high gain polymer-based EDWAs.

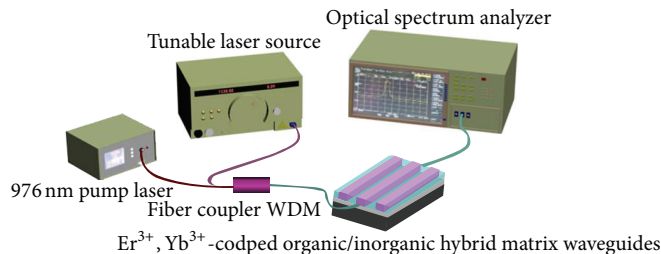


FIGURE 7: The schematics of the experimental setup for the optical gain measurement.

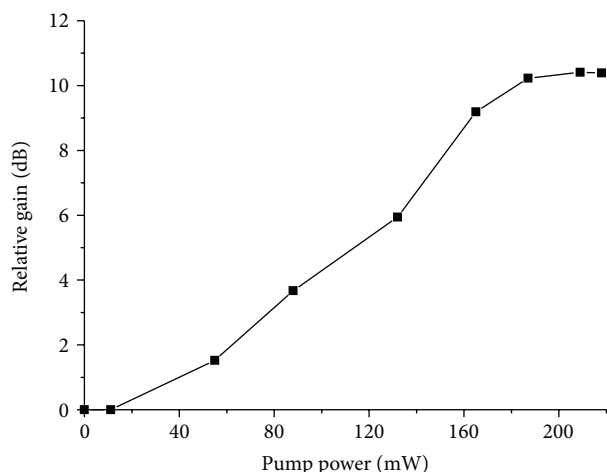


FIGURE 8: A 10.4 dB optical relative gain at 1525 wavelength was observed in a 1.1 cm long device with a cross section of $8 \times 4 \mu\text{m}^2$.

Conflict of Interests

The authors declare that there is no conflict of interests regarding the publication of this paper.

Acknowledgments

This work was supported by the National Natural Science Foundation of China (nos. 61261130586, 61177027, 11274139, 51072065, and 61077033) and the Science and Technology Development Plan of Jilin Province (no. 20140519006JH).

References

- [1] L. H. Slooff, A. van Blaaderen, A. Polman et al., "Rare-earth doped polymers for planar optical amplifiers," *Journal of Applied Physics*, vol. 91, no. 7, pp. 3955–3980, 2002.
- [2] A. Polman and F. C. J. M. van Veggel, "Broadband sensitizers for erbium-doped planar optical amplifiers: review," *Journal of the Optical Society of America B: Optical Physics*, vol. 21, no. 5, pp. 871–892, 2004.
- [3] R. N. Ghosh, J. Shmulovich, C. F. Kane et al., "8-mW threshold Er^{3+} -doped planar waveguide amplifier," *IEEE Photonics Technology Letters*, vol. 8, no. 4, pp. 518–520, 1996.
- [4] Y. Wei, F. Lu, X. Zhang, and D. Chen, "Polyol-mediated synthesis of water-soluble $\text{LaF}_3:\text{Yb},\text{Er}$ upconversion fluorescent nanocrystals," *Materials Letters*, vol. 61, no. 6, pp. 1337–1340, 2007.
- [5] D. Zhang, C. Chen, D. Zheng, T. Li, L. Song, and Z. Zhen, "Erbium-ytterbium codoped waveguide amplifier fabricated with solution-processable complex," *Applied Physics Letters*, vol. 94, no. 4, Article ID 041119, 2009.
- [6] C. Chen, D. Zhang, T. Li, D. Zhang, L. Song, and Z. Zhen, "Demonstration of Optical Gain at 1550 nm in erbium-ytterbium co-doped polymer waveguide amplifier," *Journal of Nanoscience and Nanotechnology*, vol. 10, no. 3, pp. 1947–1950, 2010.
- [7] K. Vu and S. Madden, "Tellurium dioxide Erbium doped planar rib waveguide amplifiers with net gain and 2.8 dB/cm internal gain," *Optics Express*, vol. 18, no. 18, pp. 19192–19200, 2010.
- [8] D. Zhang, C. Chen, C. Chen et al., "Optical gain at 1535 nm in $\text{LaF}_3:\text{Er},\text{Yb}$ nanoparticle-doped organic-inorganic hybrid material waveguide," *Applied Physics Letters*, vol. 91, no. 16, Article ID 161109, 2007.
- [9] S. H. Bo, J. Hu, Z. Chen et al., "Core-shell $\text{LaF}_3:\text{Er},\text{Yb}$ nanocrystal doped sol-gel materials as waveguide amplifiers," *Applied Physics B: Lasers and Optics*, vol. 97, no. 3, pp. 665–669, 2009.
- [10] S. Bo, J. Wang, H. Zhao et al., " $\text{LaF}_3:\text{Er},\text{Yb}$ doped sol-gel polymeric optical waveguide amplifiers," *Applied Physics B: Lasers and Optics*, vol. 91, no. 1, pp. 79–83, 2008.
- [11] J. Wang, J. Hu, D. Tang, X. Liu, and Z. Zhen, "Oleic acid (OA)-modified $\text{LaF}_3:\text{Er},\text{Yb}$ nanocrystals and their polymer hybrid materials for potential optical-amplification applications," *Journal of Materials Chemistry*, vol. 17, no. 16, pp. 1597–1601, 2007.
- [12] W. H. Wong, E. Y. B. Pun, and K. S. Chan, " $\text{Er}^{3+}-\text{Yb}^{3+}$ codoped polymeric optical waveguide amplifiers," *Applied Physics Letters*, vol. 84, no. 2, pp. 176–178, 2004.
- [13] G. A. Kumar, C. W. Chen, J. Ballato, and R. E. Riman, "Optical characterization of infrared emitting rare-earth-doped fluoride nanocrystals and their transparent nanocomposites," *Chemistry of Materials*, vol. 19, no. 6, pp. 1523–1528, 2007.
- [14] G. A. Kumar, C. W. Chen, R. Riman, S. Chen, D. Smith, and J. Ballato, "Optical properties of a transparent $\text{CaF}_2:\text{Er}^{3+}$ fluoropolymer nanocomposite," *Applied Physics Letters*, vol. 86, no. 24, Article ID 241105, pp. 1–3, 2005.
- [15] X. Zhai, J. Li, S. Liu et al., "Enhancement of 1.53 μm emission band in $\text{NaYF}_4:\text{Er}^{3+},\text{Yb}^{3+},\text{Ce}^{3+}$ nanocrystals for polymer-based optical waveguide amplifiers," *Optical Materials Express*, vol. 3, no. 2, pp. 270–277, 2013.

- [16] X. Zhai, S. Liu, X. Liu et al., "Sub-10 nm BaYF₅:Yb³⁺,Er³⁺ core-shell nanoparticles with intense 1.53 μ m fluorescence for polymer-based waveguide amplifiers," *Journal of Materials Chemistry C*, vol. 1, no. 7, pp. 1525–1530, 2013.
- [17] D. Dai, Y. Shi, S. He, L. Wosinski, and L. Thylen, "Gain enhancement in a hybrid plasmonic nano-waveguide with a low-index or high-index gain medium," *Optics Express*, vol. 19, no. 14, pp. 12925–12936, 2011.

Research Article

Applications of Silver Nanowires on Transparent Conducting Film and Electrode of Electrochemical Capacitor

Yuan-Jun Song,^{1,2} Jing Chen,³ Jing-Yuan Wu,^{1,2} and Tong Zhang^{1,2}

¹ School of Electronic Science and Engineering, Southeast University, Nanjing 210096, China

² Suzhou Key Laboratory of Metal Nano-Optoelectronic Technology, Suzhou Research Institute of Southeast University, Suzhou 215123, China

³ School of Physics and Key Laboratory of Weak-Light Nonlinear Photonics, Nankai University, Tianjin 300071, China

Correspondence should be addressed to Tong Zhang; tzhang@seu.edu.cn

Received 28 February 2014; Revised 15 May 2014; Accepted 19 May 2014; Published 2 June 2014

Academic Editor: Qin Chen

Copyright © 2014 Yuan-Jun Song et al. This is an open access article distributed under the Creative Commons Attribution License, which permits unrestricted use, distribution, and reproduction in any medium, provided the original work is properly cited.

Silver nanowire has potential applications on transparent conducting film and electrode of electrochemical capacitor due to its excellent conductivity. Transparent conducting film (G-film) was prepared by coating silver nanowires on glass substrate using Meyer rod method, which exhibited better performance than carbon nanotube and graphene. The conductivity of G-film can be improved by increasing sintering temperature. Electrode of electrochemical capacitor (I-film) was fabricated through the same method with G-film on indium tin oxide (ITO). CV curves of I-film under different scanning rates had obvious redox peaks, which indicated that I-film exhibited excellent electrochemical pseudocapacitance performance and good reversibility during charge/discharge process. In addition, the specific capacitance of I-film was measured by galvanostatic charge/discharge experiments, indicating that I-film exhibits high special capacitance and excellent electrochemical stability.

1. Introduction

In recent years, noble metal nanomaterials, especially silver nanomaterial become the focus of research because of their unique physical and chemical properties, which has been widely used in catalysis [1], optical, electrical [2, 3], and antibacterial [4] areas. Among these various silver nanostructures, nanowire has attracted intense forces due to its high dc conductivity and optical transmittance. As optoelectronic devices become smaller and lighter, there is an increasing need for efficient transparent electrodes. The most common material of transparent electrodes is indium tin oxide (ITO); however, ITO cannot keep pace with the development of optoelectronic devices because of its high cost, brittleness, and critical preparation process. Although people have tried to use other materials to fabricate transparent electrodes, such as carbon nanotubes (CNTs) [5–8], graphene [9–11], and conducting polymer [12–14], the problem that how to achieve ratio of transmittance to sheet resistance (R_s) as high as ITO still cannot be solved. Therefore, many groups put efforts on metallic nanowires, particularly silver nanowires. Leem

et al. [15] have pioneered silver nanowires as the electrode in solar cells, and the transmittance of it was 89.3% with low R_s of 10 Ω/sq . Since then, silver nanowire films have been fabricated by rod-coating technique [16] and spray-coating method [17]. Therefore, silver nanowire can be used as a replacement of ITO in the future. In order to further decrease the R_s of silver nanowire film, Bergin et al. [18] studied the effects of the length and diameter of silver nanowires on their properties. Longer nanowires can result in lower R_s due to fewer connections between nanowires. Therefore, the preparation of ultralong nanowires is an urgent issue. Apart from increasing the length of nanowire to improve its properties, Hu et al. applied mechanical pressing method to reduce the resistance of junctions, which can make connection of silver nanowires closer leading to the increase of the conductivity [19]. They also found that coating gold on the film is an efficient way, which can make the surface of silver nanowire smooth leading to the decrease of the junction resistance. Zhu et al. [20] used plasma treatment to remove the polymer coated on the surface of silver nanowire and welded the junctions, improving the performance of silver nanowire

film. However, the large contact resistance of internanowires is still a limitation of the development of silver nanowire films in optoelectronic and electronic devices.

In addition, silver nanowire can also be used as electrodes of electrochemical capacitor. Transparent capacitors have potential application on energy storage [21–23]. Sorel et al. [24] prepared transparent capacitor by spray-coating silver nanowires on polymer films, which exhibited capacitor properties with $1.1 \mu\text{F}/\text{cm}^2$. However, compared with other electrodes of capacitor, the specific capacitance was much lower. Pan et al. [25] found that nanostructured AgO electrode showed excellent electrochemical properties, and silver nanowires can be oxidized to Ag_2O forming Ag/ Ag_2O core-shell nanostructures during the electrochemical process [26]; therefore, silver nanowire is a promising candidate of electrochemical capacitor.

In this paper, we prepared long silver nanowires by a simple method reported in our previous work. Based on this, transparent conducting film (G-film) and electrode of electrochemical capacitor (I-film) were fabricated by coating silver nanowires on glass or ITO, respectively, and their characteristics were investigated. The relationship between transmittance and R_s of G-film was discussed. The conductivity of G-film was improved by increasing sintering temperature. By cyclic voltammetry and galvanostatic charge/discharge experiments, the capacitor properties of I-film were studied, indicating that silver nanowire has high and stable electrochemical capacitance which can be used as material of electrode of electrochemical pseudocapacitance.

2. Experimental

Silver nitrate (AgNO_3 , 99+%), sodium chloride (NaCl), ethylene glycol (EG), concentrated sulfuric acid (H_2SO_4), and hydrogen peroxide (H_2O_2) were all purchased from Nanjing Chemical Reagent Co., Ltd. Polyvinyl pyrrolidone (PVP, K88) was purchased from Aladdin. Indium tin oxide (ITO) was purchased from Nanjing Chemical Reagent Co., Ltd.

The morphologies and Energy Dispersive Spectrometer (EDS) of silver nanowires were measured by scanning electron microscope (SEM) (SIRION, USA). The R_s of silver nanowire film was measured by four-probe technique with a Keithley 2701 source meter. UV-vis spectra were recorded by a fiber-optic spectrometer (PG2000, Ideo Optics Technology Ltd., Shanghai, China). Electrochemical capacitance property of silver nanowire electrode is investigated through cyclic voltammetry (CV) and galvanostatic charge/discharge measurements using an electrochemical workstation (CHI 760D, CH Instruments Co., Ltd.).

2.1. Preparation of Silver Nanowires. Silver nanowire was prepared by the method reported in our previous work [27]. In each synthesis, 1 mL EG solution of AgNO_3 (0.9 M) and 0.6 mL EG solution of NaCl (0.01 M) were added into 18.4 mL EG solution of PVP (0.286 M). Then the mixture was refluxed at 185°C for 20 min. After the above processes, the excess PVP and EG were removed by adding deionized water centrifuging at 14000 rpm for 10 min, 3 times.

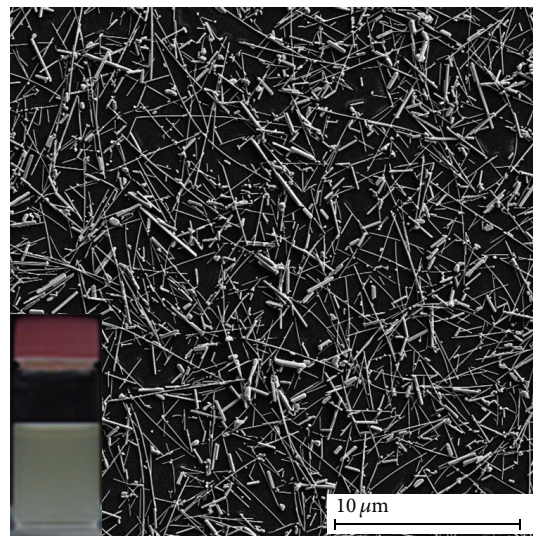


FIGURE 1: The SEM image of silver nanowires: the inset is the corresponding solution.

2.2. Procedure of Silver Films on Glass and ITO. The glass and ITO substrates were treated by the mixture solution of concentrated sulfuric acid and hydrogen peroxide under ultrasonication for 30 min, which can make them hydrophilic. In this case, uniform film can be obtained. Silver nanowires were coated on glass or ITO substrate with treatment, using Meyer rod, and then heated in 150°C for 20 min. The film obtained on glass substrate was named G-film. Samples 1 to 5 are G-films fabricated with 2 mM, 1.75 mM, 1.5 mM, 1 mM, and 0.5 mM silver nanowires solution, respectively. The film obtained on the ITO was named I-film. The two kinds of films have different properties because of different substrates.

3. Results and Discussions

3.1. Morphology of Silver Nanowire Film. As shown in Figure 1, uniform silver nanowire film was prepared using Meyer rod. The length of most silver nanowire exceeds $5 \mu\text{m}$, which is long enough to be connected into a network. The inset in Figure 1 is silver nanowire colloids. The color of silver colloids is yellowish white, similar to the highly purified silver nanowire colloids obtained after cross-flow filtration [28]. Preparation of high yield and long silver nanowires has been studied by many groups; however, these reaction processes are usually complex or difficult to control [29, 30]. Without fine control of reactant concentrations and growth process, the obtained silver nanowires are always in low yield accompanied by large amounts of by-products such as nanocubes or nanospheres growing from isotropic seeds, which influences the properties of silver nanowire films.

3.2. Transparent Conducting Film. Optical transmittance over a large wavelength range is an important property for transparent and conductive film. Figure 2 exhibits the transmittances of G-films with different thicknesses, which were fabricated on glass substrates with different concentrations of silver nanowires. The transmittance of sample 1 is 13%, which

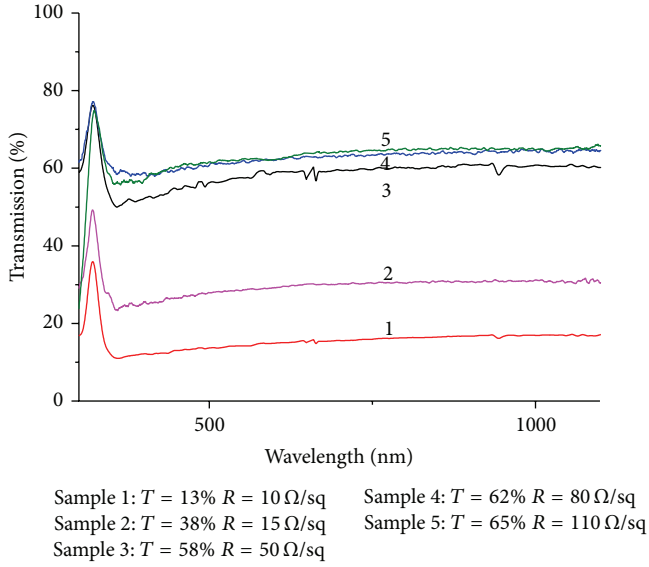


FIGURE 2: The transmittance and R_s of G-film fabricated with different concentrations of silver nanowires. (1) 2 mM/L; (2) 1.75 mM/L; (3) 1.5 mM/L; (4) 1 mM/L; (5) 0.5 mM/L.

is very low. When the concentration decreased from 2 mM to 0.5 mM, the transmittance of samples showed an increasing tendency reaching 31%, 58%, 62%, and 65%, respectively. In addition, it can be seen in Figure 2 that the transmittances of G-films keep stable in the near-infrared regions, which is important for solar cells. However, the transmittance of ITO decreased from 1100 nm described to its plasmon resonance peak at 1300 nm [19]. The conductivity of G-films is also affected by the thickness of film. As shown in Figure 2, with the increase of thickness, the R_s of G-film drops.

As mentioned in the introduction, it is a big problem to decrease the junction resistance of silver nanowire film. We found that increasing the sintering temperature is a facile and effective way to improve the conductivity of silver nanowire film. As shown in Table 1, when the sintering temperature was 150°C, the R_s of sample 4 was 80 Ω/sq . Increasing sintering temperature to 200°C, the R_s dropped to 45 Ω/sq . Because the PVP coated on surface of silver nanowires was decomposed partially at 200°C, the surfaces of silver nanowires can connect together leading to higher conductivity [31]. In addition, at 200°C some silver nanowires can be welded together. When the sintering temperature was 250°C, PVP was almost removed and most of the junctions between silver nanowires were melted resulting in the lower R_s with 15 Ω/sq , which can be seen in Figure 3(a). When the sintering temperature was 300°C, although some of silver nanowires were broken, the film still was a conductive network with lower R_s (6 Ω/sq) shown in Figure 3(b). However, when thinner sample 5 was sintered at 300°C, many silver nanowires were broken leading to nonconductive film which can be seen in Figure 3(d). At 400°C, the silver nanowires of sample 4 were almost broken (in Figure 3(c)). According to (1) [20], we can calculate σ_{dc}/σ_{op} which can evaluate the performance of transparent conducting film, the higher σ_{dc}/σ_{op} means the higher ratio of transmittance to R_s . The σ_{dc}/σ_{op} of sample 4 after treated at

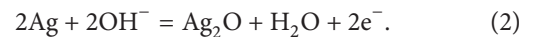
TABLE 1: R_s of samples 4 and 5 under different sintering temperatures.

Sintering temperature/(°C)	150	200	250	300	400
R_s of sample 4 (Ω/sq)	80	45	15	6	/

300°C was 116.5 which is higher than that of carbon nanotube [32, 33] and graphene [34]. Therefore, G-films have potential application on optoelectronic devices:

$$T = \left(1 + \frac{188.5 \sigma_{op}}{R_s \sigma_{dc}} \right)^{-2}. \quad (1)$$

3.3. *Electrode of Electrochemical Capacitor.* The cyclic voltammetry is used to evaluate the electrochemical properties of I-film. All these electrochemical measurements are conducted in 1.0 M KOH using a three-electrode system. Figure 4 showed CV curves of I-film electrode at a scan rate from 10 to 100 mV s^{-1} . The CV curve of I-film exhibits definitely different capacitance properties from electric double layer capacitance which has rectangular CV curve. Distinct redox peak can be seen from Figure 4 in the applied potential from -0.5 to 0.5 V versus Hg/HgO resulting from the redox reaction between Ag and Ag_2O [35] described as (2). The capacitance of I-film at different scan rates can be estimated by the area of the closed circle. Changes in capacitance at different scan rates result from that at low scan rates; the diffusion of ions throughout the reaction system is unlimited leading to full use of silver nanowire as electrode, while at high scan rates, the capacitance performs double-layer or non-Faradic behavior so that silver is not fully oxidized or reduced resulting in the decrease of the capacitance [36]. Results indicate that I-film shows excellent electrochemical pseudocapacitance performance and good reversibility during charge/discharge process:



Usually, silver experiences a reversed redox in an alkaline condition. In the first step, Ag is electrochemically oxidized to Ag_2O by OH^- , leaving a water molecule and two electrons. In a converse direction, a water molecule was separated into H^+ and OH^- , so that Ag_2O can be reduced to Ag by H^+ leaving OH^- . As a result, silver nanowires were transformed into Ag/ Ag_2O core-shell nanostructures as Figure 5(a) showed. To detect the production of Ag_2O during the process, the EDS with a large spot size (approximately 5 μm) was performed. In Figure 5(b), we can see the percentages of elements. EDS spectrum exhibited that the atom ratio between Ag and O is less than two. The reason is that sources of oxygen are from Ag_2O and PVP which is covered on the surface of silver nanowires, and the core of silver nanowires is still Ag element. Thus, the experiment result is consistent with theory and demonstrates the form of $\text{Ag}_2\text{O}/\text{Ag}$ core-shell nanostructures during the charge/discharge process.

There is a linear relationship between the scan rate and the response current according to (3) [37], where I is the discharge current (mA); C is the capacitance; dV/dt is the

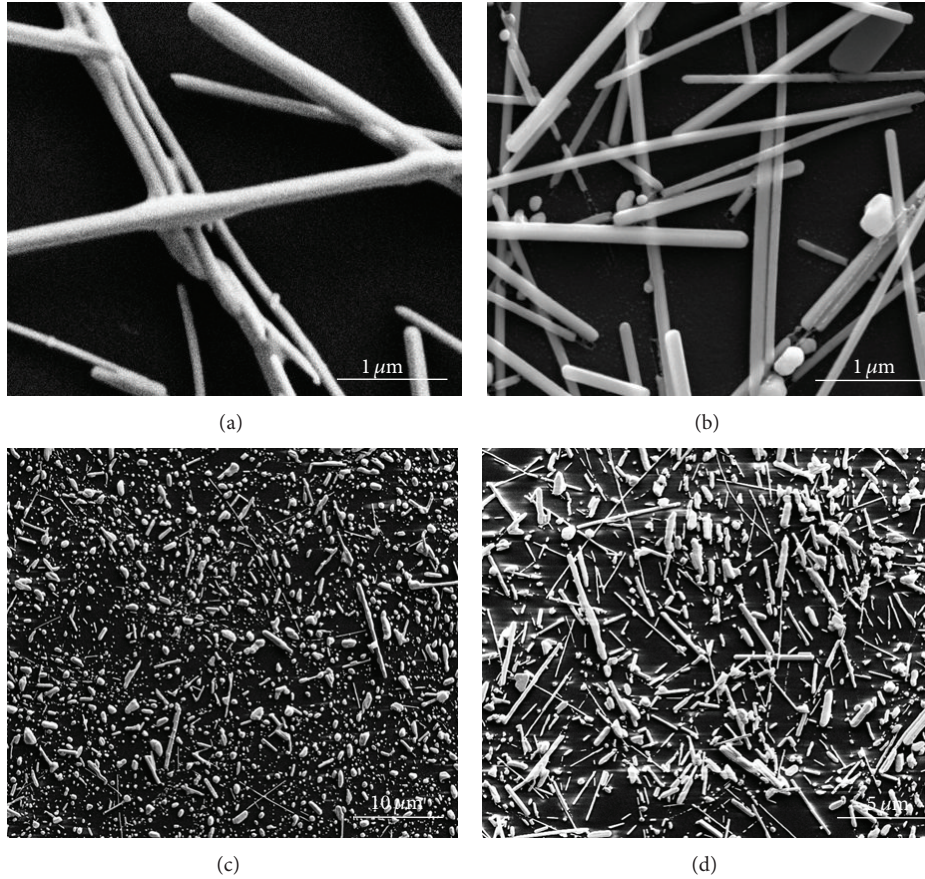


FIGURE 3: SEM images of G-film at different sintering temperature. (a) Sample 4 at 250°C; (b) sample 4 at 300°C; (c) sample 4 at 400°C; (d) sample 5 at 250°C.

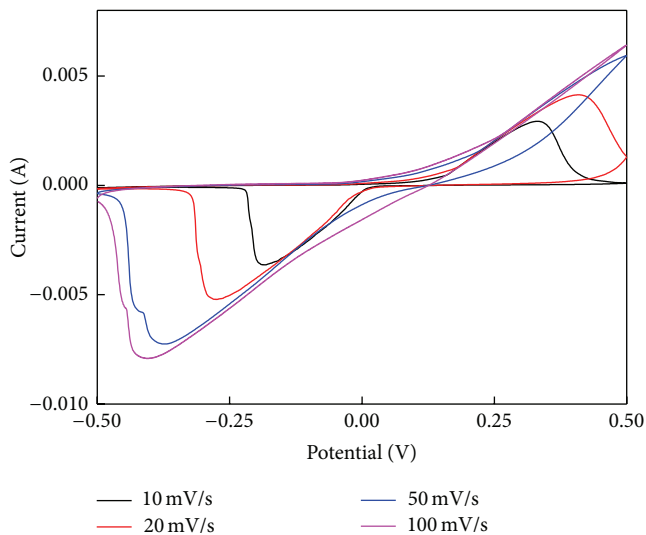


FIGURE 4: CV curves of I-film under different scanning rates.

scan rate of the cyclic voltammetry. The enclosed area of the cyclic voltammetry curve can be used to estimate the electrochemical capacitance. The specific capacitance C_s is

calculated using (4), where s is the area of active material (cm^2):

$$I = C \times \left(\frac{dV}{dt} \right) \quad (3)$$

$$C_s = \frac{C}{s} = \frac{I}{[(dV/dt) \times s]}. \quad (4)$$

The galvanostatic charge/discharge experiments are conducted at a potential window from -0.5 to 0.5 V to study the specific capacitance of I-film. Figure 6 shows the galvanostatic charge/discharge curves of I-film at a current density from 0.5 to 6 mA cm^{-2} . As Table 2 showed, the specific capacitance of I-film increased from 42.2 to 41.76 mF/cm^2 when the current density increased from 0.5 to 3.0 mA/cm^2 , which is only 1% decay. However, the specific capacitance of I-film sharply declined to 27 mF/cm^2 under 6.0 mA/cm^2 . The reason is that larger current density results in shorter time of redox between $\text{Ag}/\text{Ag}_2\text{O}$, so that ions have not enough time to diffuse from electrolyte and interphase [26]. In addition, the surface of nanowires is covered by PVP, which also have effect on the charge/discharge rate [38]. Figure 7 presented that the capacitance retention of I-film at a current density of 6 mA/cm^2 can achieve 94.2% of initial value after 100 cycles.

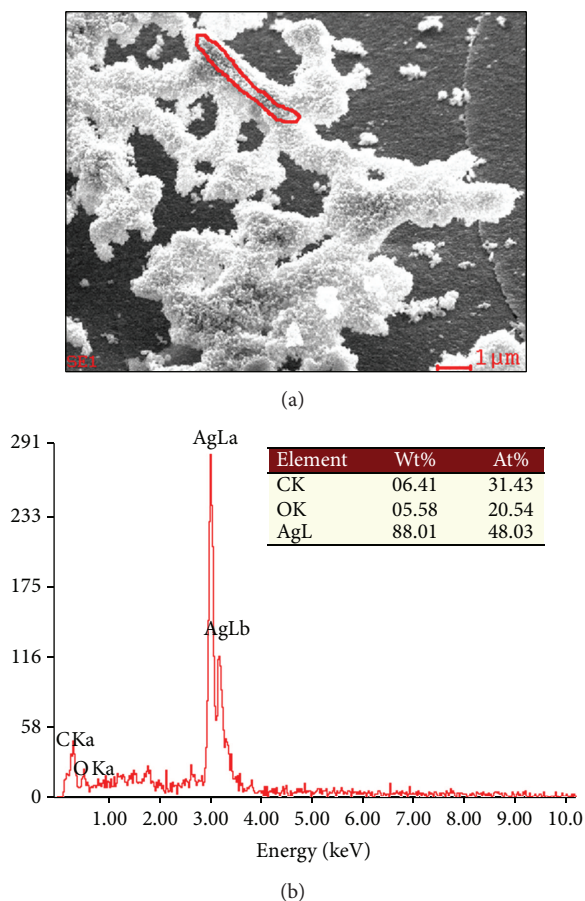


FIGURE 5: (a) SEM image for I-film; (b) EDS for I-film.

TABLE 2: Specific capacitances of I-film at different current densities.

Current density (mA/cm ²)	0.5	1.0	1.5	2.0	3.0	6.0
Specific capacitance (mF/cm ²)	42.2	42.29	42.24	42.08	41.76	27

As a result, the I-film electrode has a good stability during continuous cycles.

4. Conclusions

G-film and I-film have been fabricated by coating silver nanowires on glass and ITO, respectively. The transmittance of G-film increased with the decrease of the thickness of G-film, and the conductivity can be improved by increasing sintering temperature attributed to the removal of PVP and weld of junctions of silver nanowires. Results showed that G-film had higher ratio of transmittance to R_s than that of carbon nanotube and graphene, which is a promising replacement of ITO applied in optoelectronic areas. In addition, the CV curves of I-film under different scanning rates had obvious redox peaks indicating its good performance of electrochemical pseudocapacitance and good reversibility during charge/discharge process. Through galvanostatic charge/discharge experiments, it can be seen that

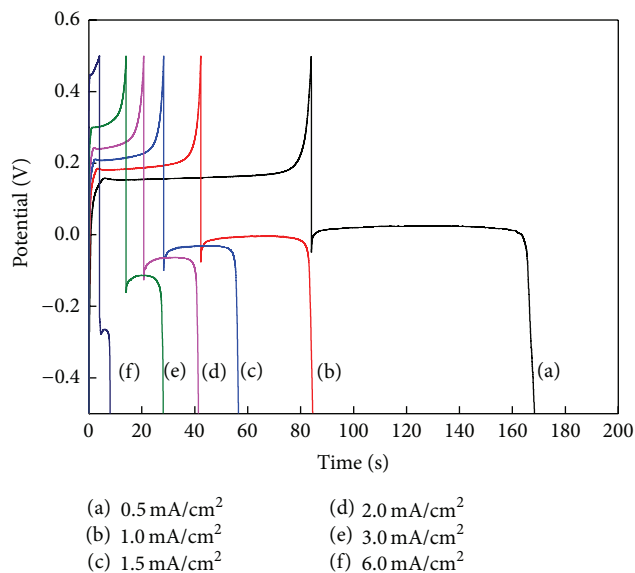


FIGURE 6: Galvanostatic charge/discharge curves of I-film under different current densities. (a) 0.5 mA/cm²; (b) 1 mA/cm²; (c) 1.5 mA/cm²; (d) 2 mA/cm²; (e) 3 mA/cm²; (f) 6 mA/cm².

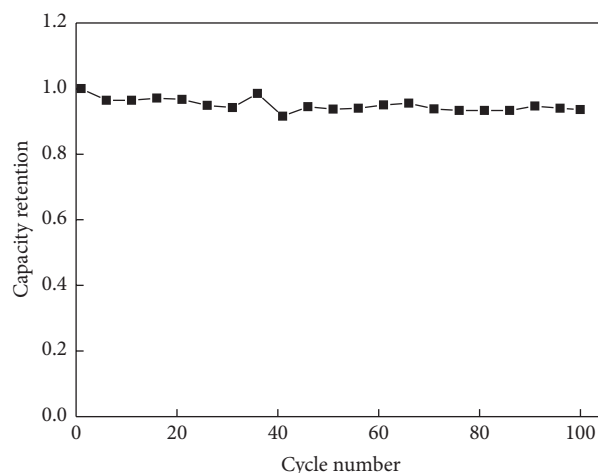


FIGURE 7: Capacity retention of I-film with respect to cycle numbers at a current density of 6 mA/cm².

the specific capacitance of I-film depends on the current density, and I-film exhibits high electrochemical stability. At low current density, the decay of specific capacitance can be ignored while, at high current density, the specific capacitance decayed dramatically because of short time for the diffusion of ions. Therefore, silver nanowires have great potential applications in optoelectronic devices.

Conflict of Interests

The authors declare that there is no conflict of interests regarding the publication of this paper.

Acknowledgments

This work is supported by NSFC under Grant no. 61307066, Doctoral Fund of Ministry of Education of China under

Grants nos. 20110092110016 and 20130092120024, Natural Science Foundation of Jiangsu Province under Grant no. BK20130630, the National Basic Research Program of China (973 Program) under Grant no. 2011CB302004, and the Foundation of Key Laboratory of Micro-Inertial Instrument and Advanced Navigation Technology, Ministry of Education, China, under Grant no. 201204.

References

- [1] C. Shi, M. Cheng, Z. Qu, and X. Bao, "Investigation on the catalytic roles of silver species in the selective catalytic reduction of NO_x with methane," *Applied Catalysis B: Environmental*, vol. 51, no. 3, pp. 171–181, 2004.
- [2] X. Y. Zhang, T. Zhang, S. Q. Zhu et al., "Fabrication and spectroscopic investigation of branched silver nanowires and nanomeshworks," *Nanoscale Research Letters*, vol. 7, article 596, 2012.
- [3] M. N. Lin, S. Q. Zhu, X. Y. Zhang, T. Zhang, and D. Su, "Island-shaped gold nanoparticle film with controllable optical properties for surface enhanced Raman scattering," *NRL Advances*. In press.
- [4] C. N. Lok, C. M. Ho, R. Chen et al., "Proteomic analysis of the mode of antibacterial action of silver nanoparticles," *Journal of Proteome Research*, vol. 5, no. 4, pp. 916–924, 2006.
- [5] Y. H. Yoon, J. W. Song, D. Kim et al., "Transparent film heater using single-walled carbon nanotubes," *Advanced Materials*, vol. 19, no. 23, pp. 4284–4287, 2007.
- [6] D. Kim, H. C. Lee, J. Y. Woo, and C. S. Han, "Thermal behavior of transparent film heaters made of single-walled carbon nanotubes," *Journal of Physical Chemistry C*, vol. 114, no. 13, pp. 5817–5821, 2010.
- [7] L. Hu, D. S. Hecht, and G. Gruner, "Percolation in transparent and conducting carbon nanotube networks," *Nano Letters*, vol. 4, no. 12, pp. 2513–2517, 2004.
- [8] B. Dan, G. C. Irvin, and M. Pasquali, "Continuous and scalable fabrication of transparent conducting carbon nanotube films," *ACS Nano*, vol. 3, no. 4, pp. 835–843, 2009.
- [9] G. Eda, G. Fanchini, and M. Chhowalla, "Large-area ultrathin films of reduced graphene oxide as a transparent and flexible electronic material," *Nature Nanotechnology*, vol. 3, no. 5, pp. 270–274, 2008.
- [10] Z. Wu, Z. Chen, X. Du et al., "Transparent, conductive carbon nanotube films," *Science*, vol. 305, no. 5688, pp. 1273–1276, 2004.
- [11] X. Wang, L. Zhi, and K. Müllen, "Transparent, conductive graphene electrodes for dye-sensitized solar cells," *Nano Letters*, vol. 8, no. 1, pp. 323–327, 2008.
- [12] H. D. Tran, D. Li, and R. B. Kaner, "One-dimensional conducting polymer nanostructures: bulk synthesis and applications," *Advanced Materials*, vol. 21, no. 14–15, pp. 1487–1499, 2009.
- [13] X. Lu, W. Zhang, C. Wang, T. C. Wen, and Y. Wei, "One-dimensional conducting polymer nanocomposites: synthesis, properties and applications," *Progress in Polymer Science*, vol. 36, no. 5, pp. 671–712, 2011.
- [14] Z. Yin and Q. Zheng, "Controlled synthesis and energy applications of one-dimensional conducting polymer nanostructures: an overview," *Advanced Energy Materials*, vol. 2, no. 2, pp. 179–218, 2012.
- [15] D. S. Leem, A. Edwards, M. Faist, J. Nelson, D. D. Bradley, and J. C. de Mello, "Efficient organic solar cells with solution-processed silver nanowire electrodes," *Advanced Materials*, vol. 23, no. 38, pp. 4371–4375, 2011.
- [16] C. H. Liu and X. Yu, "Silver nanowire-based transparent, flexible, and conductive thin film," *Nanoscale Research Letters*, vol. 6, no. 1, article 75, 2011.
- [17] D. Y. Choi, H. W. Kang, H. J. Sung, and S. S. Kim, "Annealing-free, flexible silver nanowire-polymer composite electrodes via a continuous two-step spray-coating method," *Nanoscale*, vol. 5, no. 3, pp. 977–983, 2013.
- [18] S. M. Bergin, Y. H. Chen, A. R. Rathmell, P. Charbonneau, Z. Y. Li, and B. J. Wiley, "The effect of nanowire length and diameter on the properties of transparent, conducting nanowire films," *Nanoscale*, vol. 4, no. 6, pp. 1996–2004, 2012.
- [19] L. B. Hu, H. S. Kim, J. Y. Lee, P. Peumans, and Y. Cui, "Scalable coating and properties of transparent, flexible, silver nanowire electrodes," *ACS Nano*, vol. 4, no. 5, pp. 2955–2963, 2010.
- [20] S. Zhu, Y. Gao, B. Hu et al., "Transferable self-welding silver nanowire network as high performance transparent flexible electrode," *Nanotechnology*, vol. 24, no. 33, Article ID 335202, 2013.
- [21] K. K. Uprety, L. E. Ocola, and O. Auciello, "Growth and characterization of transparent Pb(Zi,Ti)O₃ capacitor on glass substrate," *Journal of Applied Physics*, vol. 102, no. 8, Article ID 084107, 2007.
- [22] C. J. Xian and S. G. Yoon, "Transparent capacitor for the storage of electric power produced by transparent solar cells," *Journal of the Electrochemical Society*, vol. 156, no. 11, pp. G180–G183, 2009.
- [23] L. Hu, J. W. Choi, Y. Yang et al., "Highly conductive paper for energy-storage devices," *Proceedings of the National Academy of Sciences of the United States of America*, vol. 106, no. 51, pp. 21490–21494, 2009.
- [24] S. Sorel, U. Khan, and J. N. Coleman, "Flexible, transparent dielectric capacitors with nanostructured electrodes," *Applied Physics Letters*, vol. 101, no. 10, Article ID 103106, 2012.
- [25] J. Pan, Y. Sun, Z. Wang, P. Wan, X. Liu, and M. Fan, "Nano silver oxide (AgO) as a super high charge/discharge rate cathode material for rechargeable alkaline batteries," *Journal of Materials Chemistry*, vol. 17, no. 45, pp. 4820–4825, 2007.
- [26] Z. A. Hu, Y. X. Wang, Y. L. Xie, Y. Y. Yang, Z. Y. Zhang, and H. Y. Wu, "Ag nanowires and its application as electrode materials in electrochemical capacitor," *Journal of Applied Electrochemistry*, vol. 40, no. 2, pp. 341–344, 2010.
- [27] Y. J. Song, M. L. Wang, X. Y. Zhang, J. Y. Wu, and T. Zhang, "Investigation on the role of the molecular weight of polyvinyl pyrrolidone in the shape control of high-yield silver nanospheres and nanowires," *Nanoscale Research Letters*, vol. 9, no. 1, article 27, 2014.
- [28] K. C. Pradel, K. Sohn, and J. Huang, "Cross-flow purification of nanowires," *Angewandte Chemie*, vol. 50, no. 15, pp. 3412–3416, 2011.
- [29] X. Tang, M. Tsuji, P. Jiang, M. Nishio, S. M. Jang, and S. H. Yoon, "Rapid and high-yield synthesis of silver nanowires using air-assisted polyol method with chloride ions," *Colloids and Surfaces A: Physicochemical and Engineering Aspects*, vol. 338, no. 1–3, pp. 33–39, 2009.
- [30] Y. G. Sun, Y. D. Yin, B. T. Mayers, T. Herricks, and Y. N. Xia, "Uniform silver nanowires synthesis by reducing AgNO₃ with ethylene glycol in the presence of seeds and poly(vinyl pyrrolidone)," *Chemistry of Materials*, vol. 14, no. 11, pp. 4736–4745, 2002.
- [31] J. Y. Lee, S. T. Connor, Y. Cui, and P. Peumans, "Solution-processed metal nanowire mesh transparent electrodes," *Nano Letters*, vol. 8, no. 2, pp. 689–692, 2008.

- [32] H. Z. Geng, K. K. Kim, K. P. So, Y. S. Lee, Y. Chang, and Y. H. Lee, "Effect of acid treatment on carbon nanotube-based flexible transparent conducting films," *Journal of the American Chemical Society*, vol. 129, no. 25, pp. 7758–7759, 2007.
- [33] P. N. Nirmalraj, P. E. Lyons, S. De, J. N. Coleman, and J. J. Boland, "Electrical connectivity in single-walled carbon nanotube networks," *Nano Letters*, vol. 9, no. 11, pp. 3890–3895, 2009.
- [34] S. De and J. N. Coleman, "Are there fundamental limitations on the sheet resistance and transmittance of thin graphene films?" *ACS Nano*, vol. 4, no. 5, pp. 2713–2720, 2010.
- [35] M. Takeji, Y. Oaki, and H. Imai, "Electrically guided microweb formation with Ag nanofibers under UV irradiation and its application to electrochemical and plasmonic devices," *Journal of Physical Chemistry C*, vol. 116, no. 10, pp. 6103–6107, 2012.
- [36] H. Adelkhani, K. Didehban, and M. Hayasi, "Performance evaluation of polyacrylamide/silver composite as electrode material in electrochemical capacitor," *Current Applied Physics*, vol. 13, no. 3, pp. 522–525, 2013.
- [37] Y. Xie and X. Fang, "Electrochemical flexible supercapacitor based on manganese dioxide-titanium nitride nanotube hybrid," *Electrochimica Acta*, vol. 120, pp. 273–283, 2014.
- [38] R. Liu and S. B. Lee, "MnO₂/poly(3,4-ethylenedioxythiophene) coaxial nanowires by one-step coelectrodeposition for electrochemical energy storage," *Journal of the American Chemical Society*, vol. 130, no. 10, pp. 2942–2943, 2008.

Research Article

Partial Polarization in Interfered Plasmon Fields

**P. Martínez Vara,¹ M. A. Torres Rodríguez,² S. I. De Los Santos-García,²
J. Muñoz López,² and G. Martínez-Niconoff²**

¹Departamento de Ingenierías, Benemérita Universidad Autónoma de Puebla (BUAP), 72570 Puebla, PUE, Mexico

²Instituto Nacional de Astrofísica, Óptica y Electrónica, INAOE, Santa María Tonantzintla, 72840 Puebla, PUE, Mexico

Correspondence should be addressed to G. Martínez-Niconoff; gmartin@inaoep.mx

Received 26 February 2014; Accepted 29 April 2014; Published 25 May 2014

Academic Editor: Tong Zhang

Copyright © 2014 P. Martínez Vara et al. This is an open access article distributed under the Creative Commons Attribution License, which permits unrestricted use, distribution, and reproduction in any medium, provided the original work is properly cited.

We describe the polarization features for plasmon fields generated by the interference between two elemental surface plasmon modes, obtaining a set of Stokes parameters which allows establishing a parallelism with the traditional polarization model. With the analysis presented, we find the corresponding coherence matrix for plasmon fields incorporating to the plasmon optics the study of partial polarization effects.

1. Introduction

Elemental surface plasmon modes (Sp) are nonhomogeneous vector waves generated by the coherent oscillations of the plasma electrons [1, 2]. A generic feature that presents vector waves is the polarization which can be understood as the study of the trajectory that describes the electric field as a function of the amplitude and relative phases [3]. As a consequence of the vector structure of the Sp, polarization features can be introduced in a similar way to homogeneous waves propagating in free space. However, deep physical differences must be remarked. One of them is that the path to the electric field shares the same plane with the Poynting vector. In fact, each component of the electric field for the Sp is related with each other, according to Maxwell equations; this means that no term can be individually manipulated without modifying the other components. As a consequence, the polarization state for Sp is fixed and the polarization path cannot be modified without changing the structure of the Sp. Previous statements are contained in the expression for the electric field of a Sp, given by

$$\vec{E}_1 = a \left(\hat{i} + \frac{\alpha_1}{i\beta} \hat{k} \right) e^{i(\beta z - \omega t)} e^{-\alpha_1 x}, \quad x \geq 0;$$

$$\vec{E}_2 = a \left(\frac{\varepsilon_1}{\varepsilon_2} \hat{i} - \frac{\varepsilon_1 \alpha_2}{\varepsilon_2 i \beta} \hat{k} \right) e^{i(\beta z - \omega t)} e^{\alpha_2 x}, \quad x < 0, \quad (1)$$

where the subindex refers to the parameters of the electric field in each media. In this representation, $\varepsilon_{1,2}$ are the dielectric constant on each media, a is a parameter that describes the amplitude of the Sp, $\alpha_{1,2}$ are the decaying factor, and β is the dispersion relation function.

In the present work, we develop the study of plasmon fields, whose structure can be tunable, allowing incorporating the traditional model of polarization. We propose to use a superposition of surface plasmon cosine modes (Sp_c) generated by the interference between two Sp, where the interference parameters can be controlled [4], incorporating in this way, the polarization features desired. The convergence of the set of Sp_c generates plasmon fields with partial coherence and consequently with partial polarized features. From this propose the Stokes parameters and consequently the coherence matrix for plasmon fields can be obtained by letting the interference parameters have the behavior of a random variable, where the probability density function allows the calculus of the mean values.

The study presented represents a step forward in the study of the physics of the plasmon fields offering a great variety of contemporary applications in topics such as tunable spectroscopy, the development of plasmon tweezers, and synthesis of metamaterials.

2. Theory

The general structure of a Sp, propagating on the plane y - z , can be obtained from (1), applying a rotation along x -axis, using the expression for the electric field in medium 1, it acquires the form:

$$\vec{E} = a \left(\hat{i} + \hat{j} \frac{i\alpha}{\beta} \sin \theta + \hat{k} \frac{i\alpha}{\beta} \cos \theta \right) e^{-\alpha x} e^{i\beta(z \cos \theta + y \sin \theta)}, \quad (2)$$

where we have avoided the subindex to simplify the notation.

With the purpose to identify the interference parameters, which allows to control the polarization features, we describe the sum between two Sp whose expression is given by

$$\begin{aligned} \vec{E} = & a \left(\hat{i} + \hat{j} \frac{i\alpha}{\beta} \sin \theta + \hat{k} \frac{i\alpha}{\beta} \cos \theta \right) e^{-\alpha x} e^{i\beta(z \cos \theta + y \sin \theta)} \\ & + a \left(\hat{i} - \hat{j} \frac{i\alpha}{\beta} \sin \theta + \hat{k} \frac{i\alpha}{\beta} \cos \theta \right) e^{-\alpha x} e^{i\beta(z \cos \theta - y \sin \theta)}. \end{aligned} \quad (3)$$

Rewriting the resulting vector as a column vector, we obtain

$$\begin{aligned} \vec{E} = & 2ae^{-\alpha x} e^{i(\text{Re } \beta)z \cos \theta} \\ & \times e^{-(\text{Im } \beta)z \cos \theta} \begin{pmatrix} \cos(\text{Re } \beta y \sin \theta) \\ W \sin(\text{Re } \beta y \sin \theta) \sin \theta e^{i\delta_y} \\ W \cos(\text{Re } \beta y \sin \theta) \cos \theta e^{i\delta_z} \end{pmatrix}, \end{aligned} \quad (4)$$

whose structure corresponds to a plasmon beam cosine kind (SpC); here we have the parameters

$$\begin{aligned} W = |\beta|, \quad \delta_y = \frac{\text{Im } \beta}{\text{Re } \beta}, \\ \delta_z = \frac{\text{Im } \beta}{\text{Re } \beta} + \frac{\pi}{2}. \end{aligned} \quad (5)$$

To describe the polarization effects, from (4), we define the Jones plasmon vector as

$$\vec{J} = \begin{pmatrix} J_x \\ J_y \\ J_z \end{pmatrix} = \begin{pmatrix} \cos \Omega \\ W \sin \Omega \sin \theta e^{i\delta_y} \\ W \cos \Omega \cos \theta e^{i\delta_z} \end{pmatrix}, \quad (6)$$

where $\Omega = \text{Re } \beta y \sin \theta$. Analyzing the projection of the Jones plasmon vector on each plane and following the classical treatment of polarization [3], we identify three paths to the electric field on $(x$ - $y)$, $(x$ - $z)$, and $(y$ - $z)$ planes as follows.

(1) On the $(x$ - $y)$ plane, the trajectory for the electric field is

$$\begin{aligned} \left(\frac{E_x}{\cos \Omega} \right)^2 + \left(\frac{E_y}{W \sin \theta \sin \Omega} \right)^2 \\ - \left(\frac{2E_x E_y}{W \cos \Omega \sin \Omega \sin \theta} \right) \cos \delta_y = (\sin \delta_y)^2, \end{aligned} \quad (7)$$

and the corresponding Stokes parameters are

$$\begin{aligned} S_{0xy} &= (\cos \Omega)^2 + W^2 (\sin \theta)^2 (\sin \Omega)^2, \\ S_{1xy} &= (\cos \Omega)^2 - W^2 (\sin \theta)^2 (\sin \Omega)^2, \\ S_{2xy} &= 2W \cos \Omega \sin \theta \sin \Omega \cos \delta_y, \\ S_{3xy} &= 2W \cos \Omega \sin \theta \sin \Omega \sin \delta_y. \end{aligned} \quad (8)$$

Here we must note that Stokes parameters are dependent on the y coordinate. The simplest case corresponding to the zero order interference fringes is obtained when $y = 0$; the values for the Stokes parameters are

$$(S_{0xy}, S_{1xy}, S_{2xy}, S_{3xy})_{y=0} = (1, 1, 0, 0). \quad (9)$$

This means that the zero order interference fringe has linear polarization, being the electric field perpendicular to the y - z plane.

(2) On the $(x$ - $z)$ plane, the trajectory is

$$\begin{aligned} \left(\frac{E_x}{\cos \Omega} \right)^2 + \left(\frac{E_z}{W \cos \theta \cos \Omega} \right)^2 \\ - \left(\frac{2E_x E_z}{W \cos \theta (\cos \Omega)^2} \right) \cos \delta_z = (\sin \delta_z)^2. \end{aligned} \quad (10)$$

The Stokes parameters are given by

$$\begin{aligned} S_{0xz} &= (\cos \Omega)^2 + W^2 (\cos \theta)^2 (\cos \Omega)^2, \\ S_{1xz} &= (\cos \Omega)^2 - W^2 (\cos \theta)^2 (\cos \Omega)^2, \\ S_{2xz} &= 2W (\cos \Omega)^2 \cos \theta \cos \delta_z, \\ S_{3xz} &= 2W (\cos \Omega)^2 \cos \theta \sin \delta_z. \end{aligned} \quad (11)$$

When $y = 0$, the Stokes parameters take the form

$$\begin{aligned} (S_{0xz}, S_{1xz}, S_{2xz}, S_{3xz})_{y=0} \\ = (1 + W^2 \cos^2 \theta, 1 - W^2 \cos^2 \theta, \\ 2W \cos \theta \cos \delta_z, 2W \cos \theta \sin \delta_z), \end{aligned} \quad (12)$$

which means that the zero order interference fringe on $(x$ - $z)$ plane has elliptical polarization.

(3) On the $(y$ - $z)$ plane, the trajectory is

$$\begin{aligned} \left(\frac{E_y}{W \sin \Omega \sin \theta} \right)^2 + \left(\frac{E_z}{W \cos \Omega \cos \theta} \right)^2 \\ - \left(\frac{2E_y E_z}{W^2 \sin \Omega \sin \theta \cos \Omega \cos \theta} \right) \cos \delta_z = (\sin \delta_z)^2. \end{aligned} \quad (13)$$

The Stokes parameters are given by

$$\begin{aligned} S_{0yz} &= W^2 (\sin \theta)^2 (\sin \Omega)^2 + W^2 (\cos \theta)^2 (\cos \Omega)^2, \\ S_{1yz} &= W^2 (\sin \theta)^2 (\sin \Omega)^2 - W^2 (\cos \theta)^2 (\cos \Omega)^2, \\ S_{2yz} &= 2W^2 \sin \theta \sin \Omega \cos \theta \cos \Omega \cos \delta_z, \\ S_{3yz} &= 2W^2 \sin \theta \sin \Omega \cos \theta \cos \Omega \sin \delta_z. \end{aligned} \quad (14)$$

On $y = 0$, the values for the Stokes parameters are

$$(S_{0yz}, S_{1yz}, S_{2yz}, S_{3yz})_{y=0} = (W^2 \cos^2 \theta^2, -W^2 \cos^2 \theta^2, 0, 0), \quad (15)$$

which means that the electric field has linear polarization along z -coordinate.

It is easy to show that the Stokes parameters on each plane satisfy

$$S_0^2 = S_1^2 + S_2^2 + S_3^2, \quad (16)$$

which is satisfied for completely coherent and polarized plasmon fields. Finally we remark that each set of Stokes parameter depends on (y, θ) parameters. The parameter θ will be used in the following section to generate a set of Spc modes mutually incoherent whose convergence generates partially polarized plasmon fields [4].

As a partial conclusion, we get that the elemental surface plasmon has a fixed polarization state; however, the interference between two of them presents similar features to classical optical polarizable fields. The polarization state is described by projecting the electric field on three mutually perpendicular planes.

3. Partially Polarized Surface Plasmon Modes

The set of Stokes parameters for interfered beams are dependent on the (y, θ) parameters; consequently, each interference fringe has different polarization states and they have associated three Poincaré's spheres corresponding to the projected plasmon electric field over each plane. From this representation it is possible to incorporate partially polarized effects implicit in the coherence matrix associated to each plane. The structure of the coherence matrix in terms of the Stokes parameters is [5]

$$J = \left[\begin{array}{cc} \left\langle \frac{S_0 + S_1}{2} \right\rangle & \left\langle \frac{S_2 + iS_3}{2} \right\rangle \\ \left\langle \frac{S_2 - iS_3}{2} \right\rangle & \left\langle \frac{S_0 - S_1}{2} \right\rangle \end{array} \right], \quad (17)$$

and the angle brackets represent the mean value; it is obtained using the relation

$$\langle S_i \rangle = \int S_i(y, \theta) \rho(\theta) d\theta = M_i(y); \quad i = 0, 1, 2, 3, \quad (18)$$

where $\rho(\theta)$ is the probability density function. For the experimental implementation, we propose to use a gold thin

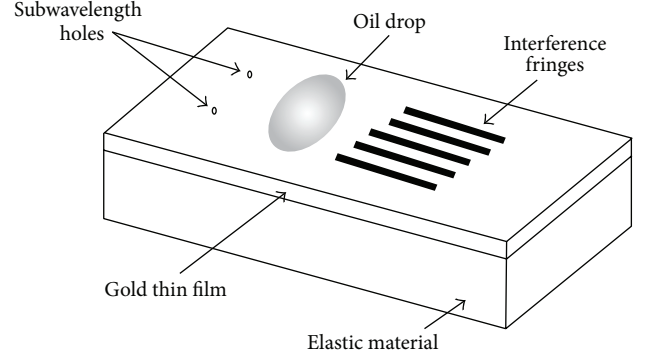


FIGURE 1: Experimental setup to generate the incoherent convergence of Spc. The width of the gold thin film is 40 nm placed on an elastic material. The relative position between holes is in the interval 5–15 nm and it is controlled applying a random force. The refractive index for the oil drop is $n = 2.1$.

film containing two subwavelength holes [6, 7] deposited on an elastic material, applying a random force parallel to the y -axis that connects the holes, we can control the relative separation between them to generate an ensemble of Spc. The setup to generate the interference is sketched in Figure 1, where the oil drop acts as a lens, generating the sum between two Sp. More details can be founded in [8].

As an example we consider the case when the probability density function $\rho(\theta)$ is uniform in the interval $-\theta_0 \leq \theta \leq \theta_0$. Expanding the Stokes parameters given by (8)–(14) in terms of Bessel function [9], the mean values acquire the following forms.

On the $(x-y)$ plane the Stokes parameters are

$$\begin{aligned} \langle S_{0xy} \rangle &= \frac{1}{2} + \left(\frac{1}{2} - \frac{W^2}{4} \right) J_0(2 \operatorname{Re} \beta y) \\ &\quad + \frac{W^2}{4} J_2(2 \operatorname{Re} \beta y), \\ \langle S_{1xy} \rangle &= \frac{1}{2} + \left(\frac{1}{2} + \frac{W^2}{4} \right) J_0(2 \operatorname{Re} \beta y) \\ &\quad - \frac{W^2}{4} J_2(2 \operatorname{Re} \beta y), \\ \langle S_{2xy} \rangle &= 2W \cos \delta_y J_1(2 \operatorname{Re} \beta y), \\ \langle S_{3xy} \rangle &= 2W \sin \delta_y J_1(2 \operatorname{Re} \beta y). \end{aligned} \quad (19)$$

In general, the mean polarization on $(x-y)$ plane corresponds to elliptical polarization, containing the case of linear polarization which occurs when $y = 0$.

On the $(x-z)$ plane the Stokes parameters are

$$\begin{aligned} \langle S_{0xz} \rangle &= \left(\frac{1}{2} + \frac{W^2}{4} \right) J_0(2 \operatorname{Re} \beta y) \\ &\quad + \frac{W^2}{4} J_2(2 \operatorname{Re} \beta y) + \frac{1}{2} + \frac{W^2}{4}, \end{aligned}$$

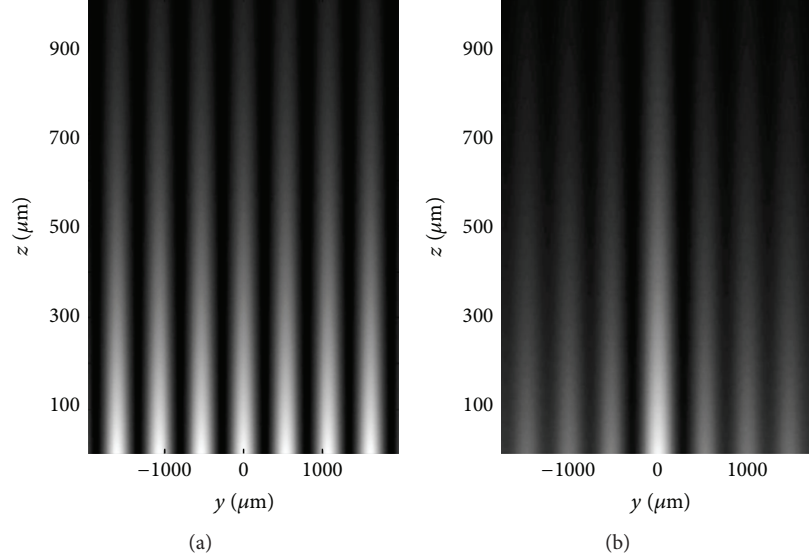


FIGURE 2: (a) Irradiance distribution for the cosine mode completely coherent. (b) Partially polarized plasmon mode with uniform probability density function.

$$\begin{aligned}
 \langle S_{1xz} \rangle &= \left(\frac{1}{2} + \frac{W^2}{4} \right) J_0(2 \operatorname{Re} \beta y) \\
 &\quad - \frac{W^2}{4} J_2(2 \operatorname{Re} \beta y) + \frac{1}{2} - \frac{W^2}{4}, \\
 \langle S_{2xz} \rangle &= W \cos \delta_z J_0(2 \operatorname{Re} \beta y), \\
 \langle S_{3xz} \rangle &= W \sin \delta_z J_0(2 \operatorname{Re} \beta y).
 \end{aligned} \tag{20}$$

In general, the mean polarization on $(x-z)$ plane corresponds to elliptical polarization.

On the $(y-z)$ plane the Stokes parameters are

$$\begin{aligned}
 \langle S_{0yz} \rangle &= W^2 (1 + J_0(2 \operatorname{Re} \beta y)) + J_2(2 \operatorname{Re} \beta y), \\
 \langle S_{1yz} \rangle &= 0, \\
 \langle S_{2yz} \rangle &= 0, \\
 \langle S_{3yz} \rangle &= 0.
 \end{aligned} \tag{21}$$

On $(y-z)$ plane the plasmon field is completely nonpolarized.

In Figure 2(a) we show the computer simulation for the irradiance distribution on $(y-z)$ plane associated to the surface plasmon cosine mode completely coherent associated with (4). In Figure 2(b), we show the computer simulation when the relative separation between apertures, sketched in Figure 1, follows a uniform probability density function, where the modulation curve is easily identified. The calculus was obtained by taking the square modulus of (4) and then obtaining the mean value. We select the $(y-z)$ plane because it is matched with the metal surface which allows us to establish the reference system.

4. Final Remarks and Conclusions

The elemental surface plasmon mode has a polarization state which cannot be modified; for this reason, in the present study, we use plasmon interfered modes, where the parameters responsible of the interference allow introducing partial polarization effects. In addition, with this kind of plasmon fields, it is possible to induce arrays of particles whose distributions depend on the interference fringes and the plasmon polarization effects are capable of inducing the particles tunable dipole moments. We remark that the dipole moments of the particle depend on the interference fringe, generating variations in the refractive index depending on position, which offers applications to the synthesis of tunable materials, in particular, the generation of metamaterials; another application is the generation of plasmon percolation effects by propagating the dipolar wave trough the particles arrays. In other context, the partial polarized features can be implemented for particle trapping [10], also as the generation of plasmon tweezers and tunable spectroscopy features.

The study presented can be extended in a general way by implementing different probability density functions, and the integral for the calculus of the mean values given by (18) can be reinterpreted as a first kind Fredholm integral equation [11], whose kernel is the Stokes parameters. This can be done by proposing a specific function for $M_i(y)$, where now the unknown function is the probability density function $\rho(\theta)$.

As conclusions, we performed the study of the plasmon electric field establishing an analogy with the traditional model of polarization. The study was implemented by means of the interference between elemental surface plasmon modes, whose parameters are tunable allowing us to induce partially polarized features. The electric field was projected on three mutual perpendicular planes and paves the way to get a deep understanding about the conditions under in which radiative process in plasmon fields may occur also as

the generation of plasmon polarization singularities [12], which must occur in the plasmon focusing regions [13].

Conflict of Interests

The authors declare that there is no conflict of interests regarding the publication of this paper.

Acknowledgment

Two of the authors (MATR, SISG) are grateful to the Conacyt for the scholarship grant.

References

- [1] M. H. Raether, *Surface Plasmons on Smooth and Rough Surfaces and on Gratings*, vol. 111 of *Springer Tracts in Modern Physics*, Springer, Berlin, Germany, 1988.
- [2] J. M. Pitarke, V. M. Silkin, E. V. Chulkov, and P. M. Echenique, "Theory of surface plasmons and surface-plasmon polaritons," *Reports on Progress in Physics*, vol. 70, no. 1, pp. 1–87, 2007.
- [3] R. M. A. Azzam and N. M. Bashara, *Ellipsometry and Polarized Light*, North-Holland, 1979.
- [4] G. Martínez Niconoff, P. Martínez Vara, J. Muñoz-Lopez, J. C. Juárez-Morales, and A. Carbajal-Dominguez, "Partially coherent surface plasmon modes," *Journal of the European Optical Society*, vol. 6, Article ID 11009, p. 52, 2011.
- [5] L. Mandel and E. Wolf, *Optical Coherence and Quantum Optics*, Cambridge U. Press, Cambridge, UK, 1995.
- [6] H. F. Ghaemi, T. Thio, D. E. Grupp, T. W. Ebbesen, and H. J. Lezec, "Surface plasmons enhance optical transmission through subwavelength holes," *Physical Review B. Condensed Matter and Materials Physics*, vol. 58, no. 11, pp. 6779–6782, 1998.
- [7] W. L. Barnes, A. Dereux, and T. W. Ebbesen, "Surface plasmon subwavelength optics," *Nature*, vol. 424, no. 6950, pp. 824–830, 2003.
- [8] G. Martinez Niconoff, J. A. Sanchez-Gil, H. H. Sanchez, and A. P. Leija, "Self-imaging and caustics in two-dimensional surface plasmon optics," *Optics Communications*, vol. 281, no. 8, pp. 2316–2320, 2008.
- [9] G. N. Watson, *A Treatise on the Theory of Bessel Functions*, Cambridge University Press, 1966.
- [10] W. Liu, D. N. Neshev, I. V. Shadrivov, A. E. Miroshnichenko, and Y. S. Kivshar, "Plasmonic Airy beam manipulation in linear optical potentials," *Optics Letters*, vol. 36, no. 7, pp. 1164–1166, 2011.
- [11] A. C. Pipkin, *A Course on Integral Equations*, Springer, 1991.
- [12] G. Martinez Niconoff, P. Martinez Vara, G. Diaz Gonzalez, J. Silva Barranco, and A. Carbajal Dominguez, "Surface plasmon singularities," *International Journal of Optics*, vol. 2012, Article ID 152937, 7 pages, 2012.
- [13] J. F. Nye, "Polarization effects in the diffraction of electromagnetic waves: the role of disclinations," *Proceedings of The Royal Society of London A: Mathematical and Physical Sciences*, vol. 387, no. 1792, pp. 105–132, 1983.

Research Article

Large-Scale Synthesis of Silver Nanoparticles by Aqueous Reduction for Low-Temperature Sintering Bonding

Qiu Xiliang,¹ Cao Yang,¹ Lin Tiesong,¹ He Peng,¹ Wang Jun,¹ Liu Ping,² and Gu Xiaolong²

¹ State Key Laboratory of Advanced Welding and Joining, Harbin Institute of Technology, Harbin 150001, China

² Zhejiang Province Key Laboratory of Soldering & Brazing Materials and Technology, Zhejiang Metallurgical Research Institute Co., Ltd., Hangzhou 310030, China

Correspondence should be addressed to He Peng; hithepeng@hit.edu.cn

Received 28 February 2014; Revised 6 May 2014; Accepted 6 May 2014; Published 21 May 2014

Academic Editor: Tong Zhang

Copyright © 2014 Qiu Xiliang et al. This is an open access article distributed under the Creative Commons Attribution License, which permits unrestricted use, distribution, and reproduction in any medium, provided the original work is properly cited.

Silver nanoparticles with average diameter of 22.4 nm were prepared by aqueous reduction method for low-temperature sintering bonding application. The reaction temperature and PVP concentration, which are the influential factors of nanoparticle characteristics, were investigated during reduction process. In our research, monodispersity of nanoparticles was remarkably improved while unfavorable agglomeration was avoided with the AgNO₃/PVP mass ratio of 1 : 4 at the reaction temperature 30°C. Besides, copper pads were successfully bonded using sintering paste employing fresh silver nanoparticles with diameter of 20~35 nm at 200°C. In addition, after morphology of the bonding joint was analysed by scanning electron microscope (SEM), the porous sintering characteristics were confirmed.

1. Introduction

With the increasing awareness to the environmental protection, lead containing materials which are quite widely applied as bonding material in electronic packaging technologies but are harmful to the environment and human body have been prohibited by many countries [1, 2]. Accordingly, lead-free solder systems such as Sn-Cu, Sn-Ag-Cu, and Sn-Bi have been well studied in recent twenty years, but there are still some inevitable drawbacks which hinder the large-scale replacement of tin-lead solder in all areas. For instance, (i) the wettability of Sn-Cu solder is poor, and it does not have an excellent matching soldering flux; (ii) Sn-Ag-Cu solder has a high soldering temperature; it is also easy to have the tin whisker and metal compounds coarsening problem; (iii) Sn-Bi solder has the disadvantages such as brittleness, poor processing property, and bad electrical or thermal conductivity [3]. Therefore, other new lead-free bonding materials, which promise almost the same packaging temperature as tin-based solders without these disadvantages, are needed urgently. Meanwhile, in order to satisfy the electronic components' requirements for high-performance and high-reliability because of the harsh operational environment [4],

the mechanical and electrical performance of the joint should be good.

Silver nanoparticles, which are easily sintered together at low temperature, could be applied as an ideal lead-free alternative. The high surface energy reduces the connection temperature to 200~300°C and the high melting point (960°C) of silver makes it possible for high-temperature packaging applications. Furthermore, the voids in the connectional silver layer throughout the joint decrease the elastic modulus, which enhance the reliability [5]. Currently, some researchers have already used silver nanoparticle sintering paste to connect Cu substrate coated Ag/Ni, Ag, Cu, or Au/Ni with shear strength of 17~40 MPa [6-8].

Although there are a few reported researches about silver nanoparticles sintering paste, it still needs to be well improved for outstanding performance. The characteristics of silver nanoparticles such as morphology, dispersion, and diameter distribution significantly influence sintering process. Therefore, the preparation of silver nanoparticles with good dispersibility, uniform particle size, and without agglomeration is prerequisite for lead-free packaging applications.

In this paper, silver nanoparticles were prepared by aqueous reduction method, using AgNO₃, NaBH₄, and

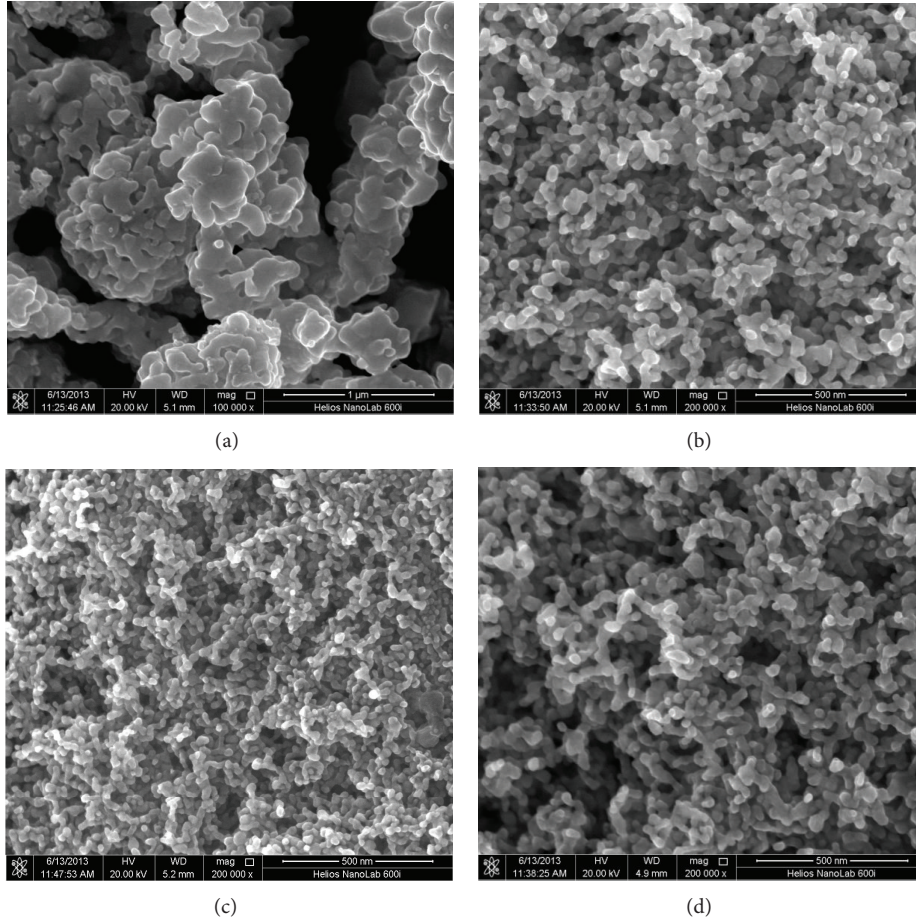


FIGURE 1: The SEM images of silver nanoparticles with different concentration of PVP: (a) 1:0; (b) 1:2; (c) 1:4; (d) 1:6.

polyvinylpyrrolidone (PVP) as raw materials. After preparation, we explored the influence of PVP concentration and reaction temperature on particle size, morphology, and polymerization degree of the nanosilver.

2. Experimental

We used the nanosilver sintering paste which was prepared by nanoparticles to connect oxygen-free copper pad; then we observed and analyzed the microstructure and morphology of the sintering interface. Detailed steps are as follows. Firstly, AgNO_3 was dissolved in deionized water with stirring. Secondly, PVP of different quality was, respectively, added into AgNO_3 solution at room temperature to obtain oxidation liquid. At the same time, we put NaBH_4 powder into NaOH solution in low concentration and stirred slowly to get colorless reducing solution. Thirdly, we mixed the oxidation liquid and reducing solution on the electric magnetic agitation apparatus with the instillment method at uniform speed of 30 drops per minute and at the constant temperature which was set beforehand. The stirring time was 30 minutes. Finally, we washed the silver nanoparticles colloid using centrifuge machine after aging to make it isolated and reduce the content of PVP. The concentration of raw material is shown in Table 1.

TABLE 1: The concentration of raw material.

Raw material	AgNO_3	NaBH_4	NaOH
Concentration mol/L \times mL	$1 \times 10^{-2} \times 25$	$1 \times 10^{-2} \times 75$	0.0125×100

After preparation, the morphology of silver particles and statistics of the particle size were acquired by the use of scanning electron microscope (SEM) and software named Nano Measurer 1.2.

The copper substrate was cut into 6×6 mm or 12×12 mm squares, and the surface was pretreated. Firstly, we immersed it in 98% ethanol for ultrasonic for 10 min, and after drying we soaked it in 5% dilute hydrochloric acid for 5 min to remove surface oxide. Finally, we washed the sample with distilled water and made it dry. When we prepared the water-based sintering paste, sintering particles must be dispersed uniformly in aqueous solution containing PVP using ultrasonic device, and then polyethylene glycol was added gradually to increase system viscosity. The sintering paste composition is shown in Table 2. Besides, the sinter condition is 10 MPa, 200°C , and 30 min.

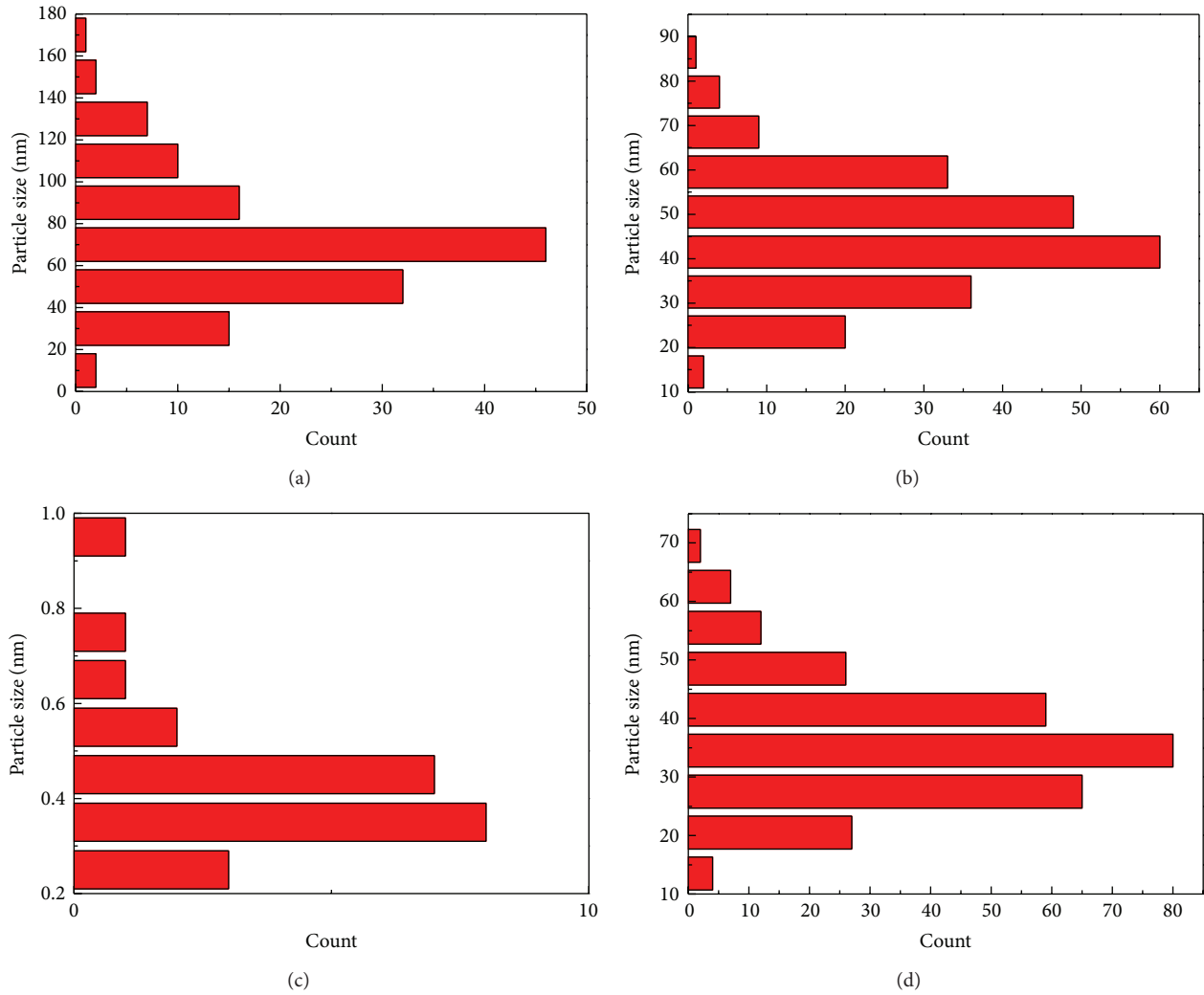


FIGURE 2: The particle diameter distribution range of silver nanoparticles with different concentrations of PVP: (a) 1:0; (b) 1:2; (c) 1:4; (d) 1:6.

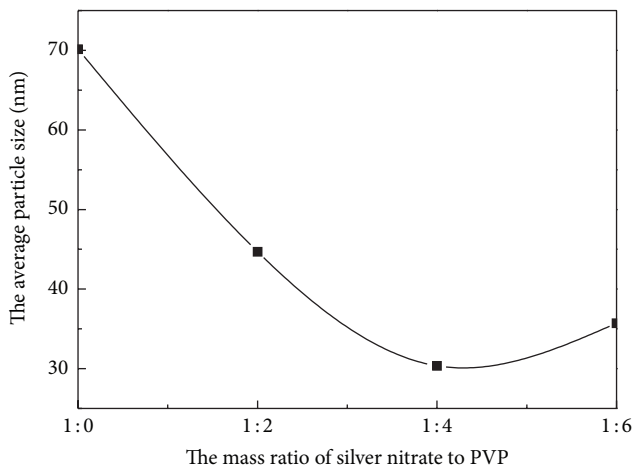


FIGURE 3: The relation of average silver nanoparticles particle diameter with the concentration of PVP.

TABLE 2: The component of soldering paste.

Silver nanoparticles	Water	PVP	Polyethylene glycol
85.0%	3.0%	0.001%	12.0%

3. Results and Discussion

3.1. The Influence of PVP Concentration on Silver Nanoparticles. Silver nanoparticles were synthesized by aqueous reduction. Their scanning electron microscopy (SEM) images with the increasing concentration of PVP are shown in Figure 1 and the statistics of particle size are shown in Figure 2; besides, the curves of average silver nanoparticles size are shown in Figure 3. From Figure 1(a) and Figure 2(a), we observed the silver nanoparticles in various shapes and serious agglomeration phenomenon when the mass ratio of AgNO_3 to PVP was 1:0, and the average particle size was

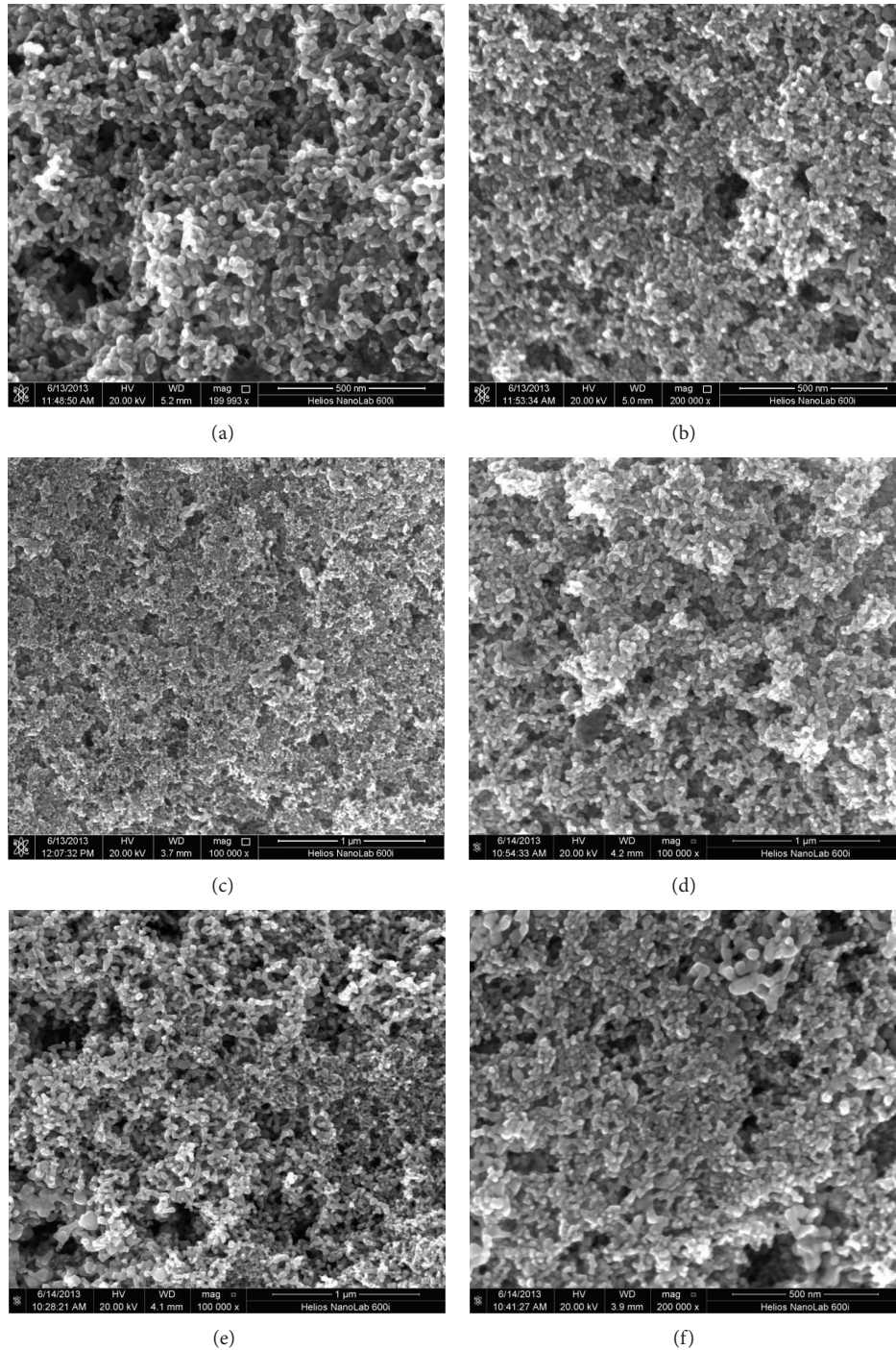


FIGURE 4: The SEM images of silver nanoparticles with different temperatures: (a) 5°C; (b) 20°C; (c) 30°C; (d) 40°C; (e) 55°C; (f) 70°C.

70.1 nm; when the mass ratio of AgNO_3 to PVP comes to 1:2, the shape and agglomeration of the particles were significantly improved, and the average particle size was 44.7 nm. When the mass ratio of AgNO_3 to PVP was 1:4, most of nanoparticles were spherical ones with average diameter of 30.3 nm, which dispersed well in the solution. When the mass ratio of AgNO_3 to PVP is 1:6, the morphological regularity, dispersion, and agglomeration of the particles were deteriorated, and the average particle size was 35.7 nm. As

shown in Figure 3, particle size decreased at first and then increased accompanied with PVP concentration; meanwhile, the average particle size (30.3 nm) was the smallest when the mass ratio of AgNO_3 to PVP was 1:4. PVP is applied as dispersant and adsorbed on the surface of silver nanoparticles formerly on the coordinate bond. This effect provides the space steric hindrance and stabilizes the colloid system [9, 10]. Therefore appropriate concentration of PVP can prevent the silver nanoparticles particles agglomeration, but if the

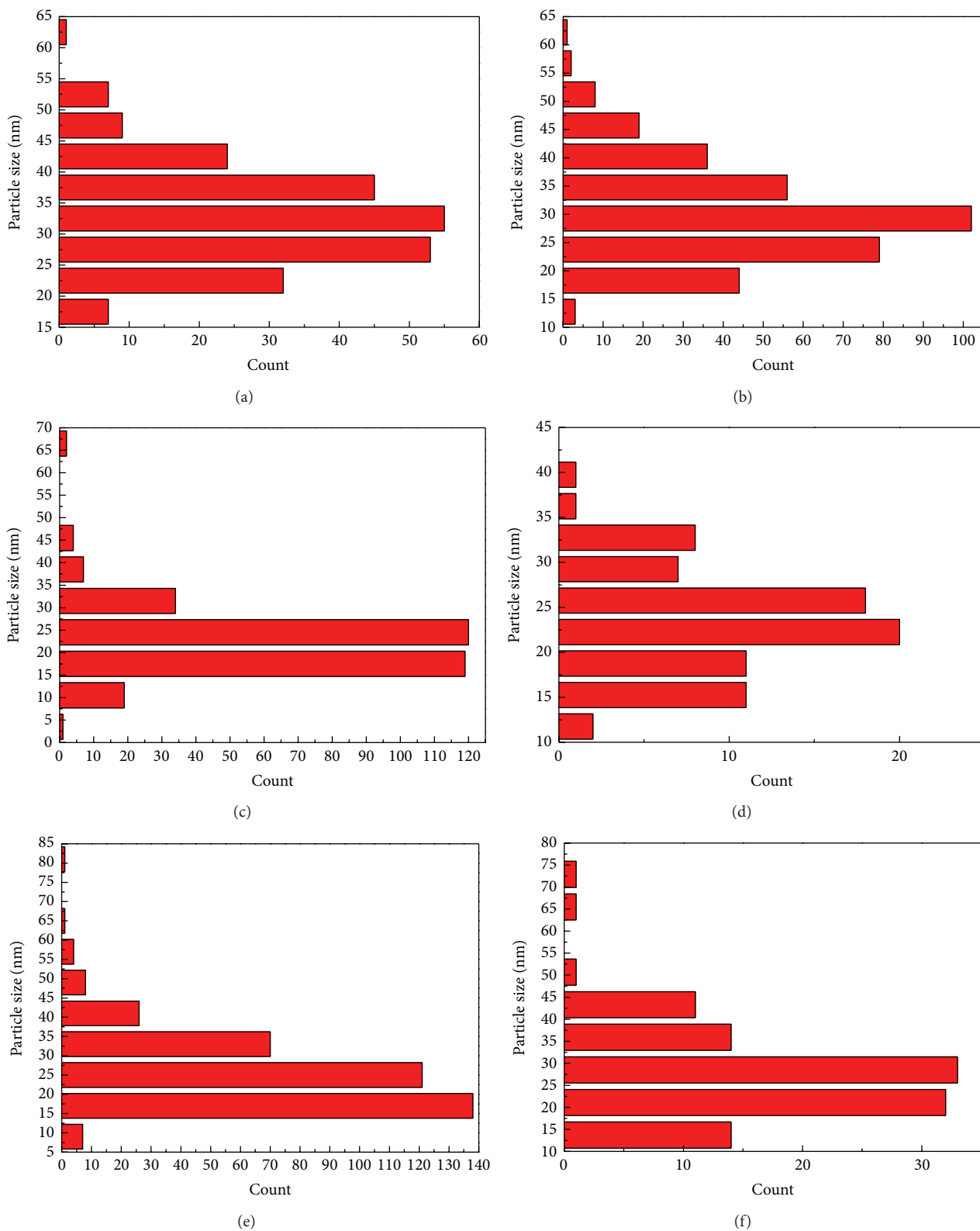


FIGURE 5: The particle diameter distribution range of silver nanoparticles with different temperatures: (a) 5°C; (b) 20°C; (c) 30°C; (d) 40°C; (e) 55°C; (f) 70°C.

concentration of PVP is too high, the thick polymer layers on particles contact mutually producing connection and exacerbating the agglomeration of silver nanoparticles.

3.2. The Influence of Temperature on Silver Nanoparticles. Silver nanoparticles were synthesized at different temperatures, with the uniform mass ratio of AgNO_3 to PVP (1:4). Scanning electron microscopy images are shown in Figure 4, and statistics of silver nanoparticle size are shown in Figure 5. Figure 6 displays the average size of particle synthesized at different temperatures. At 5°C , nanoparticle agglomeration was remarkable, while the structural regularity and the dispersion of particles were at moderate level, and the average particle size was 38.1 nm. At 20°C , agglomeration trend of silver nanoparticles weakened; meanwhile the structural regularity degree and the dispersion of particles improved, and the average particle size was 30.3 nm. Few of the AgNPs prepared at 30°C agglomerated with each other and the particle size also demonstrated excellent monodispersity. Especially particles within the scope of the average particle size were concentrated, and the average particle size was 22.4 nm. If the reaction temperature rose to 40°C , agglomeration phenomenon of silver nanoparticles was ordinary; however the structural regularity degree and the dispersion of particles were preferable, and the average particle size was 23.3 nm. When the temperature increased to 55°C , agglomeration phenomenon of silver nanoparticles was relatively serious, and the structural regularity degree and the dispersion of particles were poor, and the average particle size was 25.4 nm. Finally, when the temperature was 70°C , agglomeration phenomenon of silver nanoparticles was the worst, and obviously the structural regularity degree and the dispersion of particles were much worse, and average particle size was 28.5 nm.

As the temperature increased, the average particle size of silver nanoparticles also had the tendency of increasing at first and then decreasing, and the increase in amplitude was smaller at high temperature period as we can see in curves of each group's average particle size in Figure 6. Moreover, when the reaction temperature was 30°C , the particle size demonstrated excellent monodispersity. Besides, the reaction rate was also confirmed to be influenced by the reaction temperature. If the temperature was lower than the critical reaction temperature, it would not react as fully as the reaction at higher temperature. When the temperature increased but is still in the range of low temperature, the surface diffusion made neck formed between particles, leading to the nondensification structure. However if the reaction temperature was exorbitant, nucleation velocity of silver nanoparticles was inferior to the speed of growing up leading to the increase of silver size.

3.3. Tissue Morphology Analysis of Silver Nanoparticles Sintering Paste Sintering to Connect Copper. Silver nanoparticles prepared at 20°C with the condition that AgNO_3/PVP mass ratio was 1:4 were used to sinter, and the morphology of joint is shown in Figure 7. The base metal was tightly bonded together with sintered AgNPs. Moreover, through the

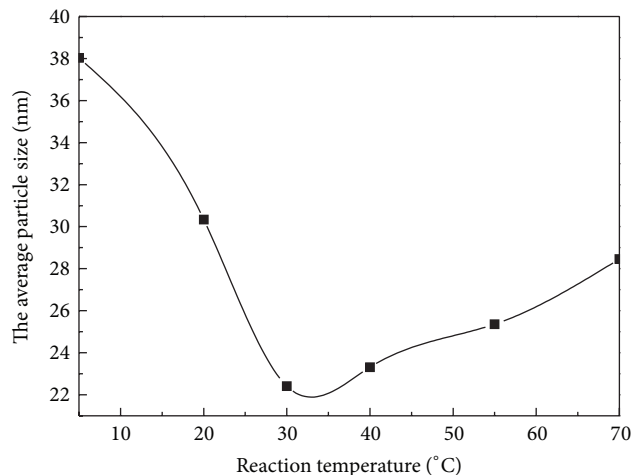


FIGURE 6: The relation of average silver nanoparticles particle diameter with the temperature.

lining scanning analysis shown in Figure 7(c), the transition gradient of silver and copper content indicated the mutual diffusion, which formed a thin layer of solid solution on the interfaces.

The joint featured porosity characteristics were shown in Figure 7(b). By analysis, we indicated that the emergence of void owed to the silver nondensification diffusion of nanoparticles at low temperature [11]. Densification behavior depends on the sintering temperature. At high temperature, grain boundary and crystal lattice diffusion lead to the formation of densification structure. As temperature rose, surface diffusion consumed a part of energy surrounding the low-temperature zone; as a consequence, the energy was not high enough to drive subsequent densification diffusion at high temperature. In other words, surface diffusion occurs at low temperature and acts the nondensification behavior.

4. Conclusion

- (1) Large-scale silver nanoparticles with average diameter of 22.4 nm were successfully prepared by aqueous reduction method. It is indicated that the average diameter of nanoparticles firstly decreased and then increased as the PVP/AgNO_3 mass ratio or reaction temperature was raised. Nanoparticle size could be well controlled by adjusting both PVP concentration and reaction temperature. It is investigated that optimal AgNO_3/PVP mass ratio was 1:4 and reaction temperature was 30°C to minimize the average diameter of nanoparticles with favorable monodispersity, while the agglomeration was remarkably avoided.
- (2) Sound low-temperature sintering bonding joints were achieved using the silver nanoparticle paste under the pressure of 10 MPa at 200°C for 30 min. Porous sintering morphology as well as limited diffusion at the interface between silver and copper was confirmed.

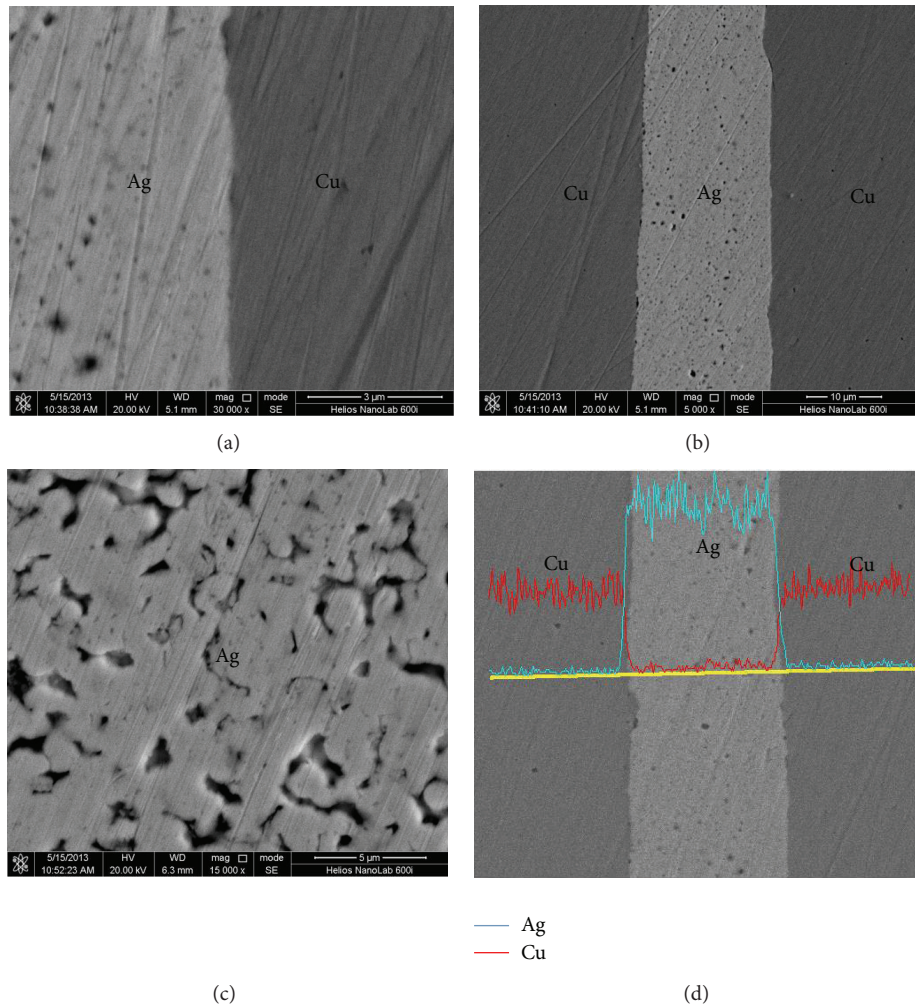


FIGURE 7: The low-temperature sintering bonding using silver nanoparticle paste: (a) the interface of welding joint; (b) the microstructure of joint; (c) the sintered microstructure of silver nanoparticles; (d) the energy spectrogram across the joint.

Conflict of Interests

The authors declare that they have no conflict of interest regarding the publication of this paper.

Acknowledgment

The research is partially supported by “National Natural Science Foundation of China (NSFC, Grant nos. 51275135 and 51321061).”

References

- [1] Y. Li, K.-S. Moon, and C. P. Wong, “Electronics without lead,” *Science*, vol. 308, no. 5727, pp. 1419–1420, 2005.
- [2] M. Li, C. Wang, H. Bang, and Y. P. Kim, “Development of a fluxless soldering method by ultrasonic modulated laser,” *Journal of Materials Processing Technology*, vol. 168, no. 2, pp. 303–307, 2005.
- [3] X. P. Zhang, L. M. Yin, and C. B. Yu, “Electronic and photonic packaging research on lead-free solder and its application progress,” *Journal of Materials Research*, vol. 22, no. 1, pp. 1–9, 2008.
- [4] Q. L. Ceng, X. L. Gu, X. B. Zhao et al., “The research progress of lead-free solder displacing the one with high temperature and high lead,” *Journal of Electronic Components and Materials*, vol. 27, no. 8, pp. 16–19, 2008.
- [5] M. Scott, “The latest development of nano silver powder in the electronics industry,” *Regeneration and Utilization of Non-Ferrous Metal*, vol. 12, pp. 36–37, 2004.
- [6] Y. Akada, H. Tasum, T. Yamaguchi, A. Hirose, T. Morita, and E. Ide, “Interfacial bonding mechanism using silver-metal-organic nanoparticles to bulk metals and observation of sintering behavior,” *Materials Transactions*, vol. 49, no. 7, pp. 1537–1545, 2008.
- [7] J. Yan, G. S. Zou, J. Li et al., “The sintering properties of nano-silver sintering paste and the research on its using for copper connecting,” *Journal of Materials Engineering*, no. 10, pp. 5–8, 2010.
- [8] K. Qi, *Nano-silver sintering paste sintering at low temperature and the research on bonding reliability [Dissertation]*, Tianjin University Institute of Chemical Industry, Tianjin, China, 2007.

- [9] J. G. Bai, T. G. Lei, J. N. Calata, and G.-Q. Lu, "Control of nanosilver sintering attained through organic binder burnout," *Journal of Materials Research*, vol. 22, no. 12, pp. 3494–3500, 2007.
- [10] J. Jiu, T. Araki, J. Wang et al., "Facile synthesis of very-long silver nanowires for transparent electrodes," *Journal of Materials Chemistry A*, vol. 2, pp. 6326–6330, 2014.
- [11] W. Z. Zhang, X. L. Qiao, and J. G. Chen, "Research progress on the controlled preparation of silver nano-materials," *Rare Metal Materials and Engineering*, vol. 37, no. 11, pp. 2059–2064, 2008.

Research Article

Variable Optical Attenuator Based on Long-Range Surface Plasmon Polariton Multimode Interference Coupler

Xiaoqiang Sun, Ying Xie, Tong Liu, Changming Chen, Fei Wang, and Daming Zhang

State Key laboratory on Integrated Optoelectronics, Jilin University, Changchun, Jilin 130012, China

Correspondence should be addressed to Fei Wang; wang_fei@jlu.edu.cn

Received 28 February 2014; Accepted 2 April 2014; Published 22 April 2014

Academic Editor: Tong Zhang

Copyright © 2014 Xiaoqiang Sun et al. This is an open access article distributed under the Creative Commons Attribution License, which permits unrestricted use, distribution, and reproduction in any medium, provided the original work is properly cited.

The fabrication and characterization of a thermal variable optical attenuator based on long-range surface plasmon polariton (LRSP) waveguide with multimode interference architecture were investigated. The surface morphology and waveguide configuration of Au stripe were studied by atomic force microscopy. The fluctuation of refractive index of poly(methyl-methacrylate-glycidyl-methacrylate) polymer cladding was confirmed to be less than 3×10^{-4} within 8 h curing at 120°C. The end-fire excitation of LRSP mode guiding at 1550 nm along Au stripe indicated that the extinction ratio of attenuator was about 12 dB at a driving power of 69 mW. The measured optical rise time and fall time are 0.57 and 0.87 ms, respectively. These favorable properties promise potentials of this plasmonic device in the application of optical interconnection.

1. Introduction

Surface plasmon polariton (SPP) is a wave of longitudinal charge oscillations of the conduction electrons at the metal surface. It leads to a transverse magnetic (TM) polarized optical surface waves that propagate along the interface between a metal and a dielectric. SPP has high confinement and sensitivity; however, it decays exponentially into both media with a small penetration depth due to the internal damping in metal, which limits the propagation distance [1–3]. The attenuation can be significantly reduced by changing a metal-dielectric interface to a symmetrical structure and constructing metal waveguides with finite width and thickness. This will result in the propagation of a low-loss fundamental symmetric mode and an increase in the propagation length, known as the long-range SPP (LRSP) [4]. The field distribution over the LRSP waveguide cross-section can extend several micrometers into the cladding, which is close to that of a single mode fiber and facilitates the optical excitation. Research works about the LRSP waveguide applications for integrated optical components, such as S-bends, Y-junctions, multimode interference (MMI) couplers, and Mach-Zehnder interferometers (MZIs), have been reported [5–10].

Owing to the symmetry request, the exciting of LRSP is highly sensitive to interface condition, especially the consistency of refractive index between materials on both sides of the metal stripe. Since the optical property of dielectric such as refractive index will change when it is heated due to the thermo-optic (TO) effect, the light propagating along LRSP waveguide will show mode-extinction due to the generated radiation loss. TO modulators, switches, and variable optical attenuators (VOAs) operating in this mode have been realized [10–13]. In these works, the metal stripe both routes the optical signal and acts as the heating element by applying a current through it to affect the effective refractive index of the LRSP mode via TO effect, which may increase the insertion loss [14, 15]. This effective modulating of core layer is undoubtedly an advantage of plasmonic devices and favorable for attenuation applications. However, if the thin metal waveguide is used as a heater simultaneously, when the electrical power was applied on the metal stripe, the induced temperature close to 100°C may lead to metal stripe deformation that results from the thermal expansion difference between the metal and polymer cladding and worsens when the temperature increases beyond glass transition temperature of polymer [10, 15, 16]. Except for the refractive index variation of the claddings surrounding the metal layer,

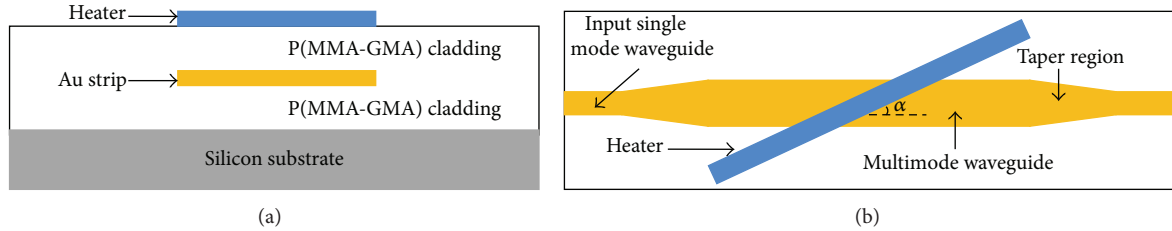


FIGURE 1: Schematic diagram of (a) cross-sectional view and (b) top view of VOA based on LRSPP waveguide.

the temperature dependent dielectric coefficient of metal may influence the mode characteristics, too [17]. Besides, a visible melting of thin metal films at the electrode may happen due to the mass flow caused by the applied direct current of high densities ($>10^8 \text{ A/m}^2$) [18]. And optically noninvasive electrical contacts make the fabrication process more complex. Thus, in the above configurations, the limited physical lifetime of the thin metal waveguide as a heater is inadequate for commercial applications due to its low thickness of less than 30 nm.

In recent years, various attenuators based on different materials have been investigated. A plasmonic waveguide VOA with a cross-section of $190 \text{ nm} \times 190 \text{ nm}$ shows a low polarization dependent loss of 2.5 dB [19]. However, due to the direct current applying on metal stripe, its working reliability faces the same problems mentioned above. A compact VOA based on the cutoff effect of photonic crystal waveguide exhibits a variable attenuation range of 29 dB with a device length of only $16.8 \mu\text{m}$ [20], an electrooptic VOA in silicon-on-insulator achieves a response frequency of about 2 MHz [21], and the monolithic integration of germanium p-i-n photodetector with silicon VOA based on submicrometer Si rib waveguide is demonstrated, too [22]. These works present excellent performance in different aspects. However, techniques of high precise photolithography and etching make the fabrication become very challenging.

Here, we propose a simple VOA structure consisting of a MMI coupler in the form of LRSPP at a wavelength of $1.55 \mu\text{m}$. The index of polymer cladding decreases with its temperature increasing as the upper electrode is heating, so that the effective index of higher-order modes in the waveguide decreases, eventually getting cutoff. The output optical power is then controlled by the generated radiation and mode mismatch to the unheated segments. In this design, the interferential characteristic of MMI waveguide allows a good fabrication tolerance, and the polymer cladding can provide refractive index compatibility with optical fibers, which facilitates optical coupling. Traditional UV photolithography and wet chemical etching techniques imply a low cost fabrication. This proposed that LRSPP based thermal tunable device can be applied in photonic integrated circuit for channel power equalizing in wavelength division multiplex technology [23–25].

2. Thermally Activated LRSPP Attenuator

2.1. Device Architecture. The proposed LRSPP attenuator architecture supported by a silicon wafer consists of a MMI

golden stripe symmetrically sandwiched between polymer claddings. To decrease optical reflection and improve precision, a hyperbolic tapered waveguide with a length of $2050 \mu\text{m}$ is used to connect single mode input/output ports to the MMI section. The coupler is excited with a single Au stripe from the input side. An aluminum heater is aligned above the metal stripe, as shown in Figure 1. The $30 \mu\text{m}$ thick poly(methyl-methacrylate-glycidyl-methacrylate) (P(MMA-GMA)) cladding is on silicon substrate. P(MMA-GMA) material synthesized by ourselves is used in this study due to its stable chemistry properties and relatively low refractive index of about 1.48 at wavelength 1550 nm . The thickness of the Au metal stripe is about 20 nm , which is the compromise of mode confinement and optical propagation loss. The input and output single mode waveguide is designed to have a width of $5 \mu\text{m}$ and a length of 5 mm . The width of MMI waveguide section with centered excitation is $24 \mu\text{m}$. Considering the thermal field distribution across the waveguide and its modulating efficiency, an $8 \mu\text{m}$ wide heater is placed with an optimized angle of $\alpha = 1.5^\circ$ on top cladding, which is a compromise between the power consumption and attenuation range. When the electrical power is applied to the heater, the generated vertical temperature grades in P(MMA-GMA) will introduce index change between the upper and lower claddings by TO effect, and then the light under the heater will be reflected at an angle of 2α with respect to the horizontal axis. Supposing that the angle is larger than the fundamental mode of the MMI coupler, the reflected light will be coupled back into higher-order modes that can be filtered out ultimately by the output tapered region and the single mode waveguide. More light will be reflected with the driving power increasing, which results in a larger attenuation [26].

2.2. Multimode Interference Coupler. MMI couplers commonly include a region of multimode waveguide that couples the optical power from the input ports to output ports. The working principle of MMI couplers depends on self-imaging effect that an interference pattern consisting of a single or multifold reproductions of the input field appears periodically when sufficient modes are excited along the MMI region [27, 28]. The propagation of higher-order modes besides the fundamental mode can couple the input power to the output ports with low insertion losses [29]. Few works based on the self-imaging have been reported in plasmonic devices, though MMI patterns have already been observed with LRSPP waveguides [2].

According to the principle of self-imaging effect, the beat length between two lowest-order modes of LRSPP wave can be described as

$$L_{\pi} = \frac{\pi}{(\beta_0 - \beta_1)} = \frac{\lambda}{2(N_0^{\text{eff}} - N_1^{\text{eff}})}, \quad (1)$$

where λ is the wavelength, β_0 and β_1 are propagation constants, and N_0^{eff} and N_1^{eff} obtained from the calculation of effective index method are effective indices of the zero- and first-order mode, respectively. Due to the symmetry of the input field at coupler entrance, only even eigenmodes can be generated when a single-mode input waveguide is centrally positioned to the MMI section. Optical reflection at the junction between the access waveguides and MMI section is ignored in the calculation.

In this paper, the permittivity of the gold stripe used is $\epsilon = 131.95 + 12.65i$ at a wavelength of $1.55 \mu\text{m}$. At room temperature, refractive indices of Au and silicon wafer are $\tilde{n}_{\text{Au}} = 0.55 + 11.5i$ and $n_{\text{Si}} = 3.5$, respectively [8]. P(MMA-GMA) with a refractive index of 1.4801 and a thickness of $30 \mu\text{m}$ is used here to accommodate LRSPP modes. Considering the attenuation induced by the resistance of metal stripe, single or multifold images of the input electromagnetic field appeared as the periodic maxima will occur periodically in accordance with the property self-imaging effect, and the length of MMI coupler is chosen to be $3000 \mu\text{m}$.

2.3. Thermal Effect. It is well known that the refractive index of a material commonly is a function of its temperature and depends on thermal expansion coefficient. Polymer cladding of P(MMA-GMA) has a negative expansion coefficient, which implies that its refractive index decreases with temperature rising and follows the linear relationship

$$n(T) = n(T_0) + (T - T_0) \left(\frac{dn}{dT} \right), \quad (2)$$

where n is the refractive index, T is the temperature, and dn/dT is referred to as the TO coefficient, which is considered to be a constant when the temperature fluctuates within a certain range. Then, the temperature generated by the applying of electrical power on the heater exhibits a maximum close to the heater and reduces gradually from it. This temperature gradient in P(MMA-GMA) cladding results in a negative gradient of refractive index above the metal stripe and the consequential asymmetry of refractive index breaks the condition for mode interference of LRSPP, leading to the radiation loss of the LRSPP mode. Thus, the optical output of the attenuator would be controlled by varying the temperature gradient formed in the device by electrical heating.

When a certain driving power is applied to the heater, the temperature distribution across the section is shown in Figure 2. The maximal temperature appears close to the heater and drops away from it. Here, the silicon substrate and top surface were assumed to be an efficient heat sink and exposed to still air at room temperature. The temperature dependence of the complex refractive index of gold

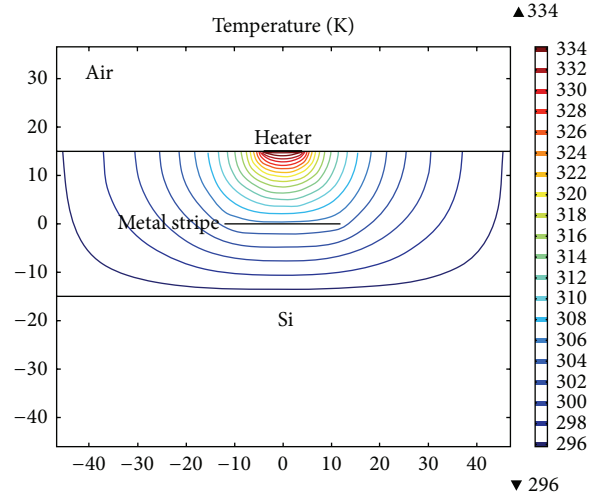


FIGURE 2: Temperature profile in the waveguide when the temperature of heater is 334 K.

$\tilde{n}_{\text{Au}} = n + i\kappa$, $dn/dT = 5 \times 10^{-4}/\text{K}$ and $d\kappa/dT = -1.8 \times 10^{-4}/\text{K}$ is used [30]. The thermal conductivity of P(MMA-GMA) used here is $0.2 \text{ W/m}^2\text{C}$.

In essence, since the effective complex refractive index of metal depending on temperature can be evaluated from a temperature dependent Drude model [31, 32], the role of TO properties of metal in plasmonic structures needs to be considered when investigating the LRSPP mode change in VOA, especially when the temperature is high. The dielectric function of Au is dominated by free-electron contribution that the temperature increasing will lead to an increment of ohmic losses due to the electron-phonon scattering rate, which is similar to the variation of the static resistivity of metals at temperature increasing [33]. This effect benefits the application of plasmonic waveguides as optical attenuators [34, 35]. According to the temperature distribution analysis in Figure 2, the temperature of Au stripe in the waveguide is less than 310 K during working. Hence, the contribution of temperature dependent dielectric coefficient of metal to the mode extinction is not so distinct as those works in [13–15], in which the metal stripe both routes the optical signal and acts as a heating element.

3. Experiments

3.1. Fabrication and Characterization. The optical loss of proposed LRSPP waveguide with symmetrical polymer claddings is induced by different issues, including ohmic loss of metal, scattering loss coming from the imperfect configuration of metal stripe, and intrinsic absorption loss of cladding material. All these loss-inducing factors should be restrained and minimized to eliminate excess optical loss. Here, the same polymer material of P(MMA-GMA) is used as the upper and lower cladding to guarantee the symmetry of waveguide that can reduce the propagation loss effectively. Since LRSPP waveguides with different metal stripe thicknesses and widths can provide various mode

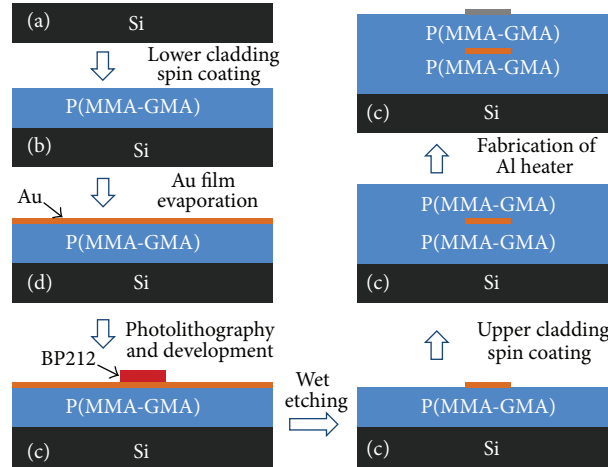


FIGURE 3: Fabrication process of the LRSPP attenuator.

field diameters, claddings are thick enough to fully support the mode field of LRSPP. The deposition techniques and parameters are crucial to obtain high quality thin metal films because discontinuous structure or variations of dielectric constant of thin film may arise from the fabrication and affect the optical characteristics of LRSPP waveguide. Thus, much experimental work has been carried out to determine the optimized technique parameters to ensure the physical quality of LRSPP waveguide, including surface roughness and configuration. Figure 3 presents the schematic diagram of fabrication process.

Firstly, a layer of $15\ \mu\text{m}$ thick P(MMA-GMA) was spin-coated on a silicon wafer at 2500 rpm as the lower cladding. After a subsequent bake at 120°C for 2.5 h, thermal evaporation method was used to deposit high-purity (>99.999%) solid Au thin metal film onto the polymer cladding. A calibrated quartz-crystal microbalance as the thickness monitor was used to keep the deposition at a rate of 0.05 nm/s that is favorable to control the thickness to be about 20 nm. To define waveguide patterns on Au film, a photoresist BP212 (Kempur Microelectronics, Inc., China) was spin-coated and patterned by ultraviolet (UV) photolithography machine (ABM Co. Inc., USA). Wet etching solution of $\text{KI}:\text{I}_2:\text{H}_2\text{O} = 4:1:100$ was used to wipe off metal film without the protection of photoresist. After that, the sample was exposed by UV light and immersed in 1 wt% NaOH solution and then agitated to remove the photoresist introduced in fabrication. Then, the same P(MMA-GMA) material was spin-coated and cured on the Au stripe as upper cladding. In order to avoid the damage on the metal stripe caused by stress build-up when baking the upper cladding, a step heating of 65°C for 20 min, 80°C for 20 min, and 90°C for 3 h was used to release inner pressure and ensure that all solvent had been evaporated from the P(MMA-GMA). Finally, a layer of 400 nm Al film was thermally evaporated and patterned with photolithography. Wet etching was adopted to form a heater on the upper cladding. Before the measurement, the waveguide sample was sliced by a wafer dicing machine DAD-3220 (DISCO Co. Inc., Japan) to minimize the uncertainty of input/output coupling loss.

AFM images were recorded with a multimode scanning probe microscope CSPM5000 (Being Nano-Instrument Ltd., China) that operated in contact mode to examine the detailed morphology of an $8\ \mu\text{m}$ wide Au stripe on a $20 \times 20\ \mu\text{m}^2$ area, as shown in Figure 4. The surface scan exhibits a thickness of about 20 nm with a smooth surface, as shown in Figure 4(a). No obvious evaporation spits or metal wing along the edge of stripe is observed, which proves the effectiveness of photolithography and etching. Steep side wall shown in Figure 4(b) provides a good mode field control that will be discussed in Section 4.

3.2. Measurement. The schematic diagram of transmission characteristics measurement setup of LRSPP attenuator is shown in Figure 5. The fiber tips need to be cleaned and checked to ensure that no damage is on their facets. The end-fire excitation of LRSPP mode guiding at telecommunication wavelengths along thin Au stripes with finite width embedded in dielectric has been experimentally proved [7]. Then, the light at 1550 nm from a tunable laser source TSL-210 (Santec Co., Japan) was perpendicularly polarized to the waveguide plane by passing through a polarization controller and then launched into the waveguide to excite LRSPP mode. A standard SM fiber was used to couple the output signal to an optical power meter or the photoreceiver. The output fiber alignment was optimized with a five-axis position control to maximize the optical output of LRSPP mode, so did the input fiber alignment, until the best condition was achieved, as shown in Figure 5(a). The far-field output of Au stripe waveguide was monitored by an infrared (IR) camera through 200 magnifications, as shown in Figure 5(b). To study the dynamic performance, the attenuator was fixed on a thermoelectric controller, temperature of which can be maintained at a constant value of about 25°C . The electrical current was introduced to the heater with microprobes. The time response of VOA was observed and recorded through an oscilloscope.

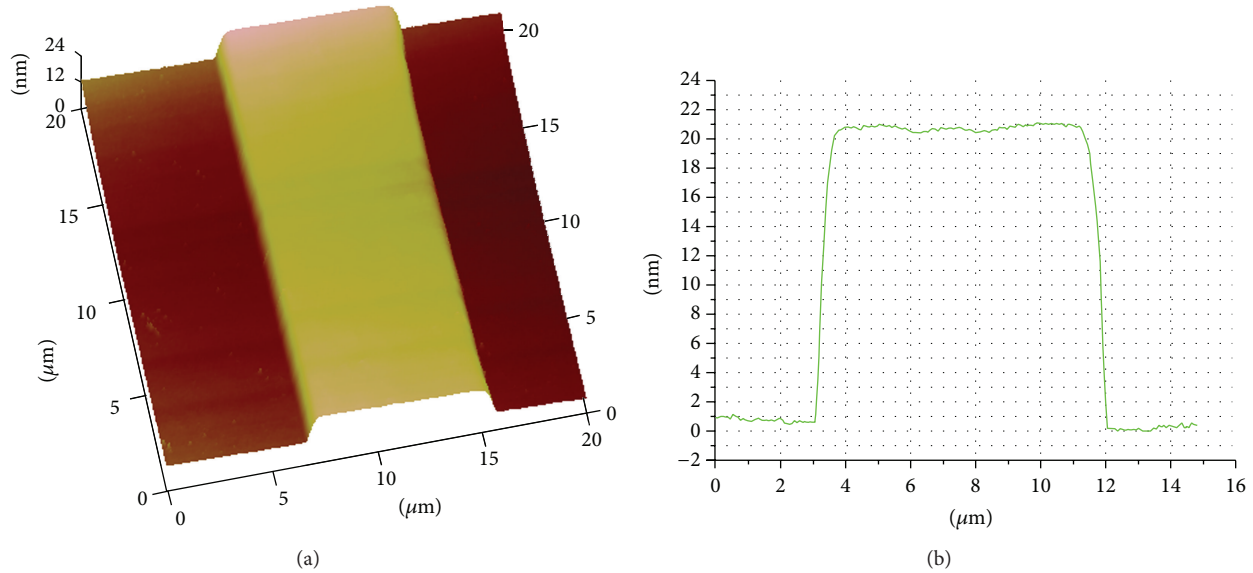


FIGURE 4: AFM images of the evaporated Au stripe on P(MMA-GMA) lower cladding (a) three-dimensional configuration of Au stripe and (b) line scan across the Au stripe.

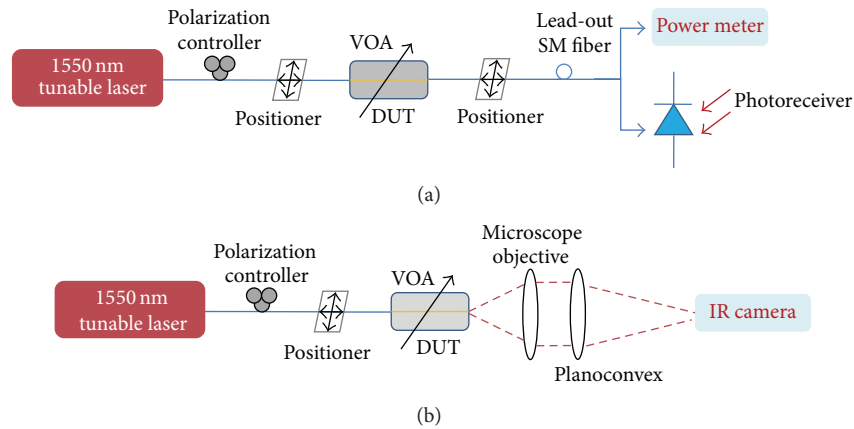


FIGURE 5: Schematic setup for measuring (a) insertion loss and time response and (b) far-field output pattern of VOA.

4. Results and Discussion

4.1. Refractive Index of Polymer Cladding. Comparing with higher index cladding materials, polymer with lower refractive index can decrease the propagation loss of LRSPP due to its less mode binding. As an optical signal transmission medium, P(MMA-GMA) material synthesized by ourselves is used in this study. Its number average molecular weight M_n and weight average molecular weight M_w are 64547 and 413466, respectively. By cut-back method, the propagation loss of a fabricated rectangular P(MMA-GMA) waveguide is less than 3 dB/cm [36]. According to the analysis in Section 3, refractive index matching of the upper and lower cladding layers is critically required due to the symmetrical condition of LRSPP waveguide. Or else, the optical mode will radiate, resulting in a large attenuation [2, 37]. Moreover, the mode field of LRSPP is designed to accommodate that of a single mode optical fiber which expands to nine micrometers or

even larger; thus the refractive index of cladding should be well controlled surrounding the Au stripe. However, the P(MMA-GMA) lower cladding experienced a second thermal curing in photolithography process and the upper cladding formation, which may change its refractive index. Therefore, the optical stability of P(MMA-GMA) should be confirmed experimentally. Figure 6 shows the refractive index of polymer cladding as a function of curing time measured by an M-2000UI ellipsometer (J. A. Woollam CO., Inc.). Typical refractive index of the film is 1.4802 for TM polarization at 1550 nm after 3 h baking. Considering the uncertainty of the measurement, no refractive index change larger than 3×10^{-4} is observed with 8 h baking at 120°C, which proves the thermal stability of cladding. This result is the average of 3 different samples and convinced to be within the uncertainty of measurement. Thus, thermal curing material P(MMA-GMA) and the fabrication process can guarantee equal refractive indices for both claddings.

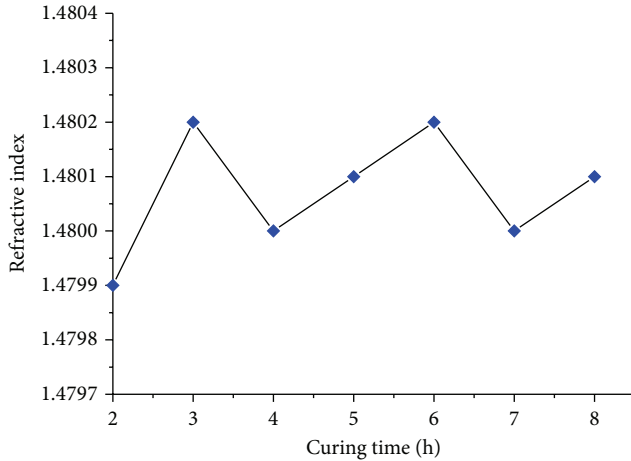


FIGURE 6: Experimental P(MMA-GMA) refractive index change with the curing time.

4.2. Insertion Loss. When the heater is working, the optical power at the output port is monitored with the infrared camera or the optical power meter aligned with IR camera removed to determine the optical extinction ratio of VOA. The optical attenuation of VOA based on LRSPP waveguide can be described as the light expelled from plasmonic waveguide with reducing the RI around Au stripe. Because of the negative thermo-optic coefficient of P(MMA-GMA) cladding, the LRSPP mode will be cut off when the electrical power is applied on the heater. The intensity distribution of the fundamental LRSPP mode at $1.55 \mu\text{m}$ is shown in Figure 7. Because of the distinguish index difference between the gold and polymer cladding, no significant mode mismatch induced loss is observed. With the applied electrical power increasing, the optical output changes from nonradiative mode in Figure 7(a) to radiative mode in Figures 7(b)–7(e) and finally extinguished in Figure 7(f). As shown in Figures 7(b)–7(e), the optical power radiates in all directions from the Au stripe to polymer claddings.

The optical output power as a function of the driving power is described in Figure 8. The extinction ratio of attenuator is about 12 dB at a driving power of 69 mW. Compared with other VOAs based on TO effect, it can be seen that, for a 3 mm long LRSPP based in-line extinction modulator, a power consumption of about 48 mW is needed to achieve the same optical attenuation, which is comparable with that of this work [10]. For polymeric waveguide VOAs, the power consumptions are both about 17 mW, which is lower than that in this paper due to the large TO coefficient of polymers [38, 39]. This relatively high power consumption is mainly due to the thick polymer cladding that extends the distance of thermal diffusion. To establish the same temperature difference between the upside and underside of Au stripe, more power is needed.

As shown in Figure 8, the measured optical signal attenuation is not so remarkable, which is attributed to the following reasons. Firstly, the optical field extending to surrounded

polymer claddings leads to a large mode size, though the LRSPP modes are controlled on the metal surface. The optical modulation induced by effective refractive index changing is unable to block all optical signal propagation. Secondly, the design of heater is supposed to be optimized. There exist different manners of heater placement on the MMI waveguide, and different heater dimensions will lead to various optical attenuations. If the heater design in this paper was further optimized, we believe the attenuation characteristic can be improved. In fact, the process induced fabrication errors, such as scattering caused by surface roughness of Au stripe, is also an origin of low attenuation. Thus, a moderate optical attenuation is obtained in this work.

The insertion loss variation as driving power is over 70 mW can be explained that some higher-order modes are excited as the LRSPP mode propagates from the input single mode waveguide to the MMI coupler, which is due to the limited length of tapered region. This may result in multimode interference in the MMI waveguide region. Therefore, the insertion loss varies sinusously as the driving power is larger than 70 mW, which weakens the mode reflection and leading to the restoration of output power.

4.3. Time Response. The response times are measured by an oscilloscope through collecting the output optical power with a butt-coupled single mode fiber, which is connected to an optical power meter. A 100 Hz square waveform drive current is applied on the heater. Since the rising edge of drive current induces mode cutoff, the thermal rise time which follows the rising edge of the drive current corresponds to the optical fall time, and vice versa. When the attenuator is subjected to a square waveform drive current, the rise and fall times are defined as the time that the detected optical power increases from 10 to 90% or decreases from 90 to 10% of its peak value, respectively.

Figure 9 shows the time response of VOA. The measured optical rise time and fall time are 0.57 and 0.87 ms, respectively. The fall time is much longer than the rise time, which is usually observed in thermo-optic attenuators. This can be explained that the temperature change in upper cladding that impacts the optical characteristic of LRSPP mode is fast due to the relatively short diffusion path existing between the heater and Au stripes when injecting the driving current, while the optical rise time is decided by thermal fall time which corresponds to the cooling process that restores the refractive index symmetry of polymer claddings after turning off the drive current. Because the heat accumulated in $30 \mu\text{m}$ thick claddings must diffuse from the optical region to the heat sink of silicon substrate with little heat evacuating through the air, this process is slower than the construction of temperature asymmetry in polymer claddings. Thus, the thermal rise time is faster than the optical fall time. However, the speed of TO effect can be increased remarkably when P(MMA-GMA) with a low thermal conductivity of $0.2 \text{ W/m}^\circ\text{C}$ is replaced by materials

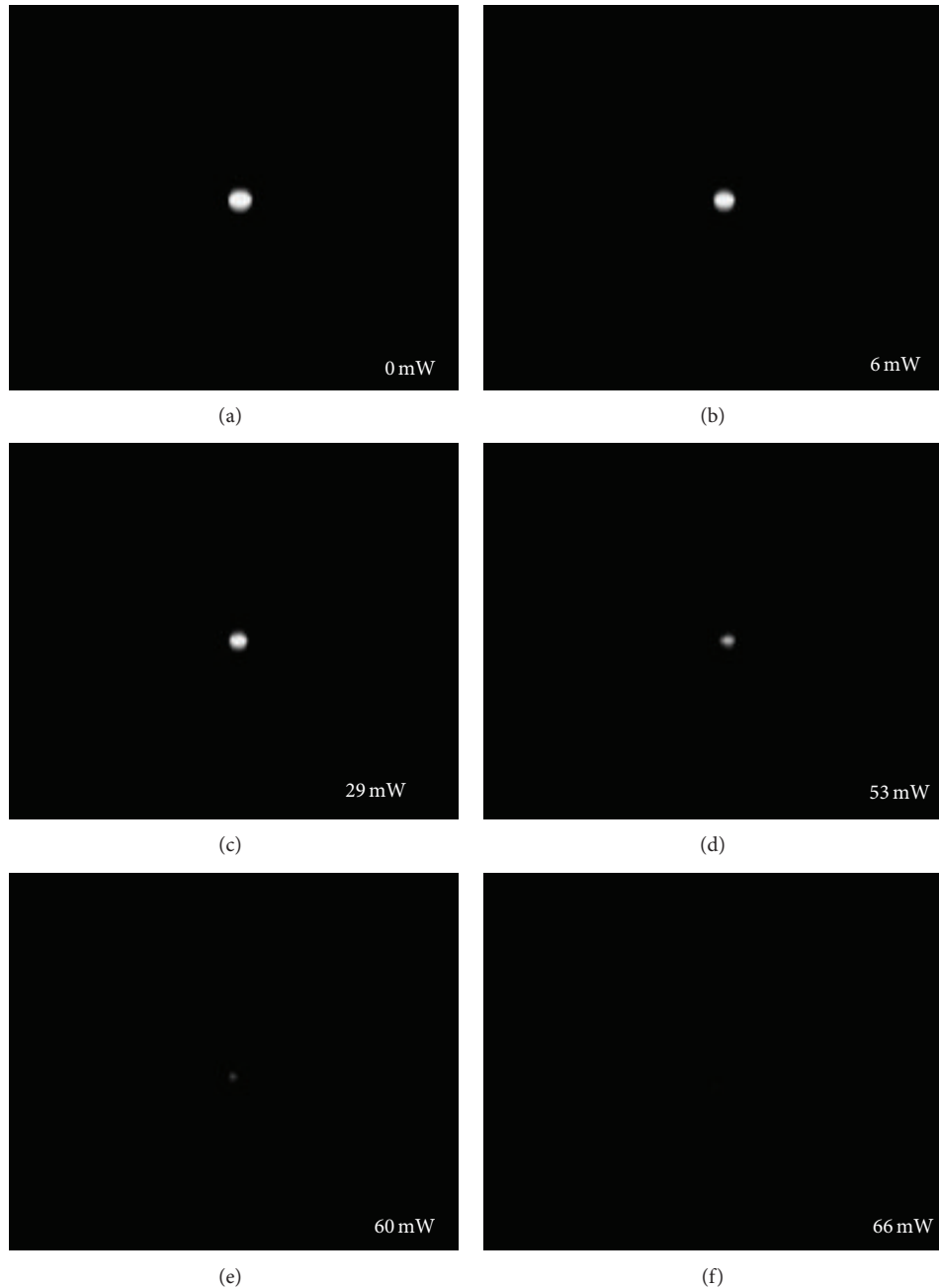


FIGURE 7: The intensity distribution of fundamental LRSP mode at $1.55 \mu\text{m}$ captured by IR camera with different electrical driving power of (a) 0 mW, (b) 6 mW, (c) 29 mW, (d) 53 mW, (e) 60 mW, and (f) 66 mW applied on the heater.

with higher thermal conductivity. Thus, it is convincing that the time response of this kind of VOA can be significantly improved and has a promising future for the application in optical communication systems.

5. Conclusions

A thermo-optic attenuator based on LRSP waveguide was investigated. Our investigations of morphological and structural characteristics of Au stripe after etching show that

no obvious evaporation spits or metal wing exists along the edge of stripe and the steep side wall provides good mode field control proved by IR photos of field patterns. The refractive index symmetry of waveguide is guaranteed by polymer cladding of P(MMA-GMA). Variable optical attenuation is realized by the thermo-optic effect induced LRSP mode radiation at telecommunication wavelength. The fabrication technology based on true planar processing and favorable performance suggests potential integration with other photonic devices.

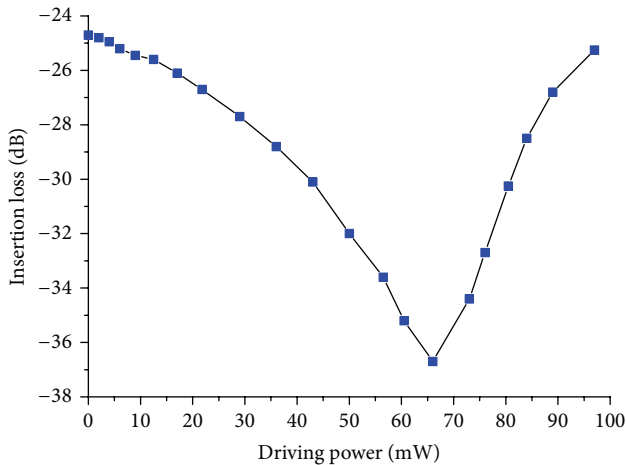


FIGURE 8: Experimental attenuation characteristic versus electrical power.

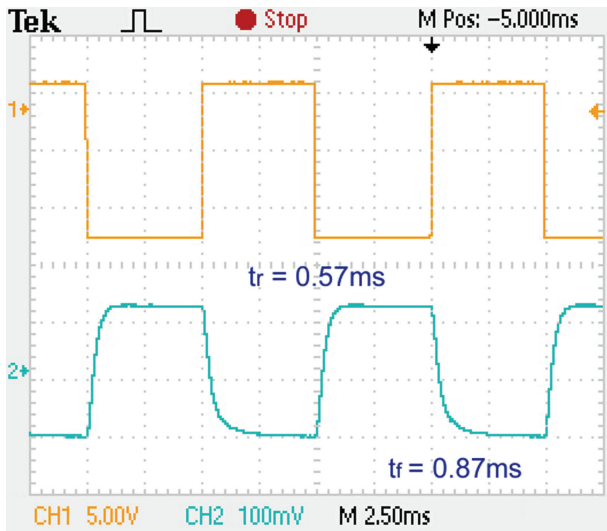


FIGURE 9: The response time of VOA is measured to be 0.57 ms for heating and 0.87 ms for cooling at 100 Hz for a fixed driving power.

Conflict of Interests

The authors declare that there is no conflict of interests regarding the publication of this paper.

Acknowledgments

This work is supported by the National Natural Science Foundation of China (nos. 61177027, 61107019, 61205032, and 61261130586), Program for Special Funds of Basic Science & Technology of Jilin University (nos. 201100253 and 201103071), and China Postdoctoral Science Foundation (no. 2012M510900).

References

- [1] T. Nikolajsen, K. Leosson, I. Salakhutdinov, and S. I. Bozhevolnyi, "Polymer-based surface-plasmon-polariton stripe waveguides at telecommunication wavelengths," *Applied Physics Letters*, vol. 82, no. 5, pp. 668–670, 2003.
- [2] A. Boltasseva, T. Nikolajsen, K. Leosson, K. Kjaer, M. S. Larsen, and S. I. Bozhevolnyi, "Integrated optical components utilizing long-range surface plasmon polaritons," *Journal of Lightwave Technology*, vol. 23, no. 1, pp. 413–422, 2005.
- [3] J. Takahara and M. Miyata, "Mutual mode control of short- and long-range surface plasmons," *Optics Express*, vol. 21, no. 22, pp. 27402–27410, 2013.
- [4] J. Lee and M. A. Belkin, "Widely tunable thermo-optic plasmonic bandpass filter," *Applied Physics Letters*, vol. 103, no. 18, Article ID 181115, 2013.
- [5] A. Khan, O. Krupin, E. Lisicka-Skrzek, and P. Berini, "Mach-Zehnder refractometric sensor using long-range surface plasmon waveguides," *Applied Physics Letters*, vol. 103, no. 11, Article ID 111108, 2013.
- [6] T. Zhang, G. Qian, Y.-Y. Wang et al., "Integrated optical gyroscope using active Long-range surface plasmon-polariton waveguide resonator," *Scientific Reports*, vol. 4, article 3855, 2014.
- [7] R. Charbonneau, P. Berini, E. Berolo, and E. Lisicka-Skrzek, "Experimental observation of plasmon-polariton waves supported by a thin metal film of finite width," *Optics Letters*, vol. 25, no. 11, pp. 844–846, 2000.
- [8] R. Charbonneau, C. Scales, I. Breukelaar et al., "Passive integrated optics elements based on long-range surface plasmon polaritons," *Journal of Lightwave Technology*, vol. 24, no. 1, pp. 477–494, 2006.
- [9] Y.-J. Tsai, A. Degiron, N. M. Jokerst, and D. R. Smith, "Plasmonic Multi-Mode Interference Couplers," *Optics Express*, vol. 17, no. 20, pp. 17471–17482, 2009.
- [10] T. Nikolajsen, K. Leosson, and S. I. Bozhevolnyi, "In-line extinction modulator based on long-range surface plasmon polaritons," *Optics Communications*, vol. 244, no. 1-6, pp. 455–459, 2005.
- [11] T. Nikolajsen, K. Leosson, and S. I. Bozhevolnyi, "Surface plasmon polariton based modulators and switches operating at telecom wavelengths," *Applied Physics Letters*, vol. 85, no. 24, pp. 5833–5835, 2004.
- [12] G. Gagnon, *Thermo-optic variable optical attenuators using plasmon polariton waveguides [M.S. thesis]*, University of Ottawa, Ottawa, Canada, 2004.
- [13] G. Gagnon, N. Lahoud, G. A. Mattiussi, and P. Berini, "Thermally activated variable attenuation of long-range surface plasmon-polariton waves," *Journal of Lightwave Technology*, vol. 24, no. 11, pp. 4391–4402, 2006.
- [14] C. Chiu, E. Lisicka-Skrzek, R. N. Tait, and P. Berini, "Fabrication of surface plasmon waveguides and devices in Cytop with integrated microfluidic channels," *Journal of Vacuum Science and Technology B*, vol. 28, no. 4, pp. 729–735, 2010.
- [15] H. Fan, R. Buckley, and P. Berini, "Passive long-range surface plasmon-polariton devices in Cytop," *Applied Optics*, vol. 51, no. 10, pp. 1459–1467, 2012.
- [16] J. Gosciniak and S. I. Bozhevolnyi, "Performance of thermo-optic components based on dielectric-loaded surface plasmon polariton waveguides," *Scientific Reports*, vol. 3, article 1803, 2013.

- [17] S. Talukder, P. Kumar, and R. Pratap, "Electric current-Induced mass flow in very thin infinite metallic films," *IEEE Transactions on Electron Devices*, vol. 60, no. 9, pp. 2877–2883, 2013.
- [18] S. Kaya, J.-C. Weeber, F. Zacharatos et al., "Photo-thermal modulation of surface plasmon polariton propagation at telecommunication wavelengths," *Optics Express*, vol. 21, no. 19, pp. 22269–22284, 2013.
- [19] K. Leosson, T. Rosenzweig, P. G. Hermannsson, and A. Boltasseva, "Compact plasmonic variable optical attenuator," *Optics Express*, vol. 16, no. 20, pp. 15546–15552, 2008.
- [20] Q. Zhao, K. Cui, X. Feng, F. Liu, W. Zhang, and Y. Huang, "Variable optical attenuator based on photonic crystal waveguide with low-group-index tapers," *Applied Optics*, vol. 52, no. 25, pp. 6245–6249, 2013.
- [21] Y.-J. He, F. Li, and Y.-L. Liu, "Silicon-on-insulator based electro-optic variable optical attenuator with a series structure," *Chinese Physics Letters*, vol. 22, no. 1, pp. 95–98, 2005.
- [22] S. Park, T. Tsuchizawa, T. Watanabe et al., "Monolithic integration and synchronous operation of germanium photodetectors and silicon variable optical attenuators," *Optics Express*, vol. 18, no. 8, pp. 8412–8421, 2010.
- [23] J. Lee, F. Lu, and M. A. Belkin, "Widely-tunable optical bandpass filter based on long-range surface plasmon polaritons," in *Plasmonics: Metallic Nanostructures and Their Optical Properties X*, vol. 8457 of *Proceedings of SPIE*, 2012.
- [24] D. Kalavrouziotis, S. Papaioannou, G. Giannoulis et al., "0.48Tb/s (12x40Gb/s) WDM transmission and high-quality thermo-optic switching in dielectricloaded plasmonics," *Optics Express*, vol. 20, no. 7, pp. 7655–7662, 2012.
- [25] J. Jiang, C. L. Callender, S. Jacob et al., "Long-range surface plasmon polariton waveguides embedded in fluorinated polymer," *Applied Optics*, vol. 47, no. 21, pp. 3892–3900, 2008.
- [26] Y. O. Noh, M.-S. Yang, Y. H. Won, and W.-Y. Hwang, "PLC-type variable optical attenuator operated at low electrical power," *Electronics Letters*, vol. 36, no. 24, pp. 2032–2033, 2000.
- [27] O. Bryngdahl, "Image formation using self-imaging techniques," *Journal of the Optical Society of America*, vol. 63, no. 4, pp. 416–419, 1973.
- [28] R. Ulrich, "Image formation by phase coincidences in optical waveguides," *Optics Communications*, vol. 13, no. 3, pp. 259–264, 1975.
- [29] L. B. Soldano and E. C. M. Pennings, "Optical multi-mode interference devices based on self-imaging: principles and applications," *Journal of Lightwave Technology*, vol. 13, no. 4, pp. 615–627, 1995.
- [30] M. Rashidi-Huyeh and B. Palpant, "Counterintuitive thermo-optical response of metal-dielectric nanocomposite materials as a result of local electromagnetic field enhancement," *Physical Review B*, vol. 74, no. 7, Article ID 075405, 2006.
- [31] S. K. Özdemir and G. Turhan-Sayan, "Temperature effects on surface plasmon resonance: design considerations for an optical temperature sensor," *Journal of Lightwave Technology*, vol. 21, no. 3, pp. 805–814, 2003.
- [32] C. S. Moreira, A. M. N. Lima, H. Neff, and C. Thirstrup, "Temperature-dependent sensitivity of surface plasmon resonance sensors at the gold-water interface," *Sensors and Actuators B*, vol. 134, no. 2, pp. 854–862, 2008.
- [33] X.-Y. Zhang, T. Zhang, A.-M. Hu, X.-J. Xue, P.-Q. Wu, and Q.-Y. Chen, "Tunable microring resonator based on dielectric-loaded surface plasmon polariton waveguides," *Journal of Nanoscience and Nanotechnology*, vol. 11, no. 12, pp. 10520–10524, 2011.
- [34] K. Leosson, T. Nikolajsen, A. Boltasseva, and S. I. Bozhevolnyi, "Long-range surface plasmon polariton nanowire waveguides for device applications," *Optics Express*, vol. 14, no. 1, pp. 314–319, 2006.
- [35] X.-Y. Zhang, A. Hu, T. Zhang, X.-J. Xue, J. Z. Wen, and W. W. Duley, "Subwavelength plasmonic waveguides based on ZnO nanowires and nanotubes: a theoretical study of thermo-optical properties," *Applied Physics Letters*, vol. 96, no. 4, Article ID 043109, 2010.
- [36] X. Fei, N. Fu, Y. Wang et al., "Synthesis and characterization of crosslinkable Poly(MMA-co-GMA) and its application in arrayed waveguide grating," *Chemical Journal of Chinese Universities*, vol. 27, no. 3, pp. 571–574, 2006.
- [37] P. Berini, "Long-range surface plasmon-polariton waveguides in silica," *Journal of Applied Physics*, vol. 102, no. 5, Article ID 053105, 2007.
- [38] Y.-O. Noh, C.-H. Lee, J.-M. Kim et al., "Polymer waveguide variable optical attenuator and its reliability," *Optics Communications*, vol. 242, no. 4–6, pp. 533–540, 2004.
- [39] M.-C. Oh, S.-H. Cho, Y.-O. Noh, H.-J. Lee, J.-J. Joo, and M.-H. Lee, "Variable optical attenuator based on large-core single-mode polymer waveguide," *IEEE Photonics Technology Letters*, vol. 17, no. 9, pp. 1890–1892, 2005.

Research Article

Si₃N₄-SiC_p Composites Reinforced by *In Situ* Co-Catalyzed Generated Si₃N₄ Nanofibers

Juntong Huang,^{1,2} Zhaohui Huang,¹ Shaowei Zhang,²
Minghao Fang,¹ and Yan'gai Liu¹

¹ School of Materials Science and Technology, China University of Geosciences (Beijing), Beijing 100083, China

² College of Engineering, Mathematics and Physical Sciences, University of Exeter, Exeter EX4 4QF, UK

Correspondence should be addressed to Zhaohui Huang; huangjl18@cugb.edu.cn and Shaowei Zhang; s.zhang@exeter.ac.uk

Received 20 December 2013; Accepted 6 March 2014; Published 3 April 2014

Academic Editor: Qin Chen

Copyright © 2014 Juntong Huang et al. This is an open access article distributed under the Creative Commons Attribution License, which permits unrestricted use, distribution, and reproduction in any medium, provided the original work is properly cited.

Si₃N₄-SiC_p composites reinforced by *in situ* catalytic formed nanofibers were prepared at a relatively low sintering temperature. The effects of catalyst Co on the phase compositions, microstructures, and physicochemical-mechanical properties of samples sintered at 1350°C–1450°C were investigated. The results showed that the catalyst Co enhanced the nitridation of Si. With the increase of Co addition (from 0 wt% to 2.0 wt%), the apparent porosity of as-prepared refractories was initially decreased and subsequently increased, while the bulk density and the bending strength exhibited an opposite trend. The Si₃N₄-SiC_p composites sintered at 1400°C had the highest strength of 60.2 MPa when the Co content was 0.5 wt%. The catalyst Co facilitated the sintering of Si₃N₄-SiC_p composites as well as the formation of Si₃N₄ nanofibers which exhibited network connection and could improve their strength.

1. Introduction

Because of its high strength, good excellent thermal shock resistance and remarkable erosion, and corrosion resistance, Si₃N₄-SiC_p composite refractories have been widely used in metallurgical and chemical industry as advanced refractories and high-temperature structural materials. In particular, as a large and medium-sized blast furnace refractory, it played a pivotal role in prolonging the lifespan of blast furnace in the past few decades [1–4].

Traditional technique to manufacture Si₃N₄-SiC_p composite refractories is usually through *in situ* nitridation reaction of Si powders and SiC particles/powders at high-temperature in tunnel kiln. It usually suffers some quality problems of “black” and “sandwich” due to an incomplete nitridation in the preparation process, thus affecting their applications. Furthermore, because the formation of Si₃N₄-SiC_p composite refractories was achieved by vapor reaction, there still exist some technical problems such as high porosity and high nitridation temperature. In addition, the bond between matrix and aggregate needs to be further

strengthened, and the strength as well as thermal shock resistance of the products needs to be further improved.

In past few years, controlling microstructural development to optimize materials' mechanical properties has been the focus of intensive research [5–9]. The previous studies show that single or mixed additives such as Y₂O₃, MgO, Al₂O₃ + Y₂O₃, and Al₂O₃ + ZrO₂ are useful for enhancing the mechanical properties of Si₃N₄-SiC_p composite refractories [10–13]. However, the nitrided temperature was higher than 1450°C, and the increase rate of strength was lower. With the development of nanotechnology [14–16], nanofibers/wires, having larger interfacial areas, the excellent mechanical and thermal properties make them ideal reinforcements for improving the strength and toughness of materials. Previous efforts have been mainly devoted to introduce the second nanofiber/wire-phase to matrix [17–21], although the increasing interest has emerged recently in *in situ* formation of nanofibers/wires in matrix [22–24].

Because of their characteristics to easily lend and take electrons from other molecules, transition metals are good metal catalysts. Recently, we have investigated the effect

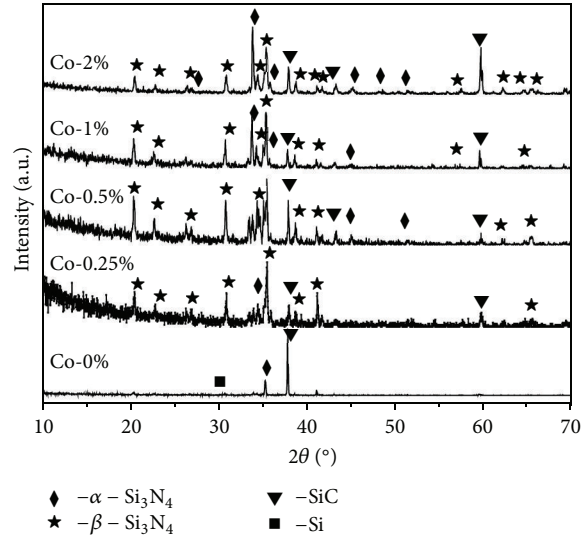


FIGURE 1: XRD patterns of Si_3N_4 - SiC_p composite refractories with various contents of Co nitrided at 1400°C .

of transition metal Co on the direct nitridation of silicon (Si) powders and morphologies of the nitridation products [25], showing primarily that Co played an important role in accelerating the Si nitridation as well as the *in situ* growth of α - Si_3N_4 nanorods/fibers. These results provided a guide for fabricating SiC-based composite refractories reinforced by *in situ* generating Si_3N_4 nanorods/fibers. A large number of pores in the refractories are benefit for the growth of one dimension nanostructures. Therefore, in this work, the transition metal Co was introduced as a catalyst into the raw materials of Si powders and SiC particles to prepare *in situ* formed Si_3N_4 with nanostructures bonded SiC refractories by nitridation reaction. The effects of Co contents on the phase compositions, microstructures, and properties of products sintered at 1350°C – 1450°C were investigated. The catalyst Co facilitated the formation of Si_3N_4 nanofibers and improved the strength of Si_3N_4 - SiC_p composites. This work provided a new insight into the nitride bonded composites reinforced by such *in situ* catalytic formed nanofibers.

2. Experimental Procedure

Si powders (>99 wt.%, 325 mesh, Aldrich Chemical Company, Inc., UK), Co powders (99.8 wt.%, $<2\ \mu\text{m}$; Sigma-Aldrich, Co., UK), SiC particles (98 wt.%, Aldrich Chemical Company, Inc., UK) with three gradation of $38\ \mu\text{m}$, $125\ \mu\text{m}$, and $380\ \mu\text{m}$ were used as raw materials to prepare the Si_3N_4 - SiC_p composite refractories. N_2 (99.99%) and polyvinyl alcohol (PVA) (concentration = 8 wt.%) were used as reactive gas and binder, respectively. The components of the samples investigated in this work are listed in Table 1.

The mixtures of Si and Co powders, in a batch of 100 g, were dry-milled by corundum balls in a corundum jar for 0.5 h with 300 r/min and then mixed with different gradation of SiC particles for 1 h with 100 r/min. The final mixtures (designated as S1, S2, S3, S4, and S5, resp.) with 5 wt.% PVA were molded into a shape of $6\ \text{mm} \times 6\ \text{mm} \times 45\ \text{mm}$ by

TABLE 1: The components of Si_3N_4 - SiC_p specimens (wt.%).

Samples	Si	SiC (wt.%)			Co extra-added (wt.%)
		380 μm	125 μm	38 μm	
S1	20	44	16	20	0
S2	20	44	16	20	0.25
S3	20	44	16	20	0.50
S4	20	44	16	20	1.00
S5	20	44	16	20	2.00

uniaxial pressing at 50 MPa in a steel die and then compacted at 200 MPa by cold isostatic pressing. After drying at 80°C for 6 h, the specimens were put in a corundum porcelain boat and then into an alumina-tube furnace. Finally, they were, respectively, heated at 1350°C , 1400°C , and 1450°C for 5 h in flowing nitrogen.

After *in situ* nitriding reaction sintering, the phase compositions of products were determined by X-ray diffraction (XRD; XD-3, Purkinje General, $\text{CuK}\alpha_1$ radiation, $\lambda = 1.5406\ \text{\AA}$). The density and apparent porosity of the sintered samples were investigated by the Archimedes' method. The bending strength of the samples was measured by a three-point bending test with a 30 mm span at a crosshead speed of 0.5 mm/min at room temperature (i.e., 22°). The microstructure of the samples was observed by scanning electron microscopy (SEM; JSM-6460, Japan) with an energy dispersive spectroscopy detector (EDS; INCAX-Sigh, Oxford, UK).

3. Results and Discussion

3.1. Phase Composition and Microstructure of Products. A slight difference existed in the products of samples nitrided at different temperatures. Basically, at 1350°C and 1400°C , some residual Si remained in the sample without Co, while

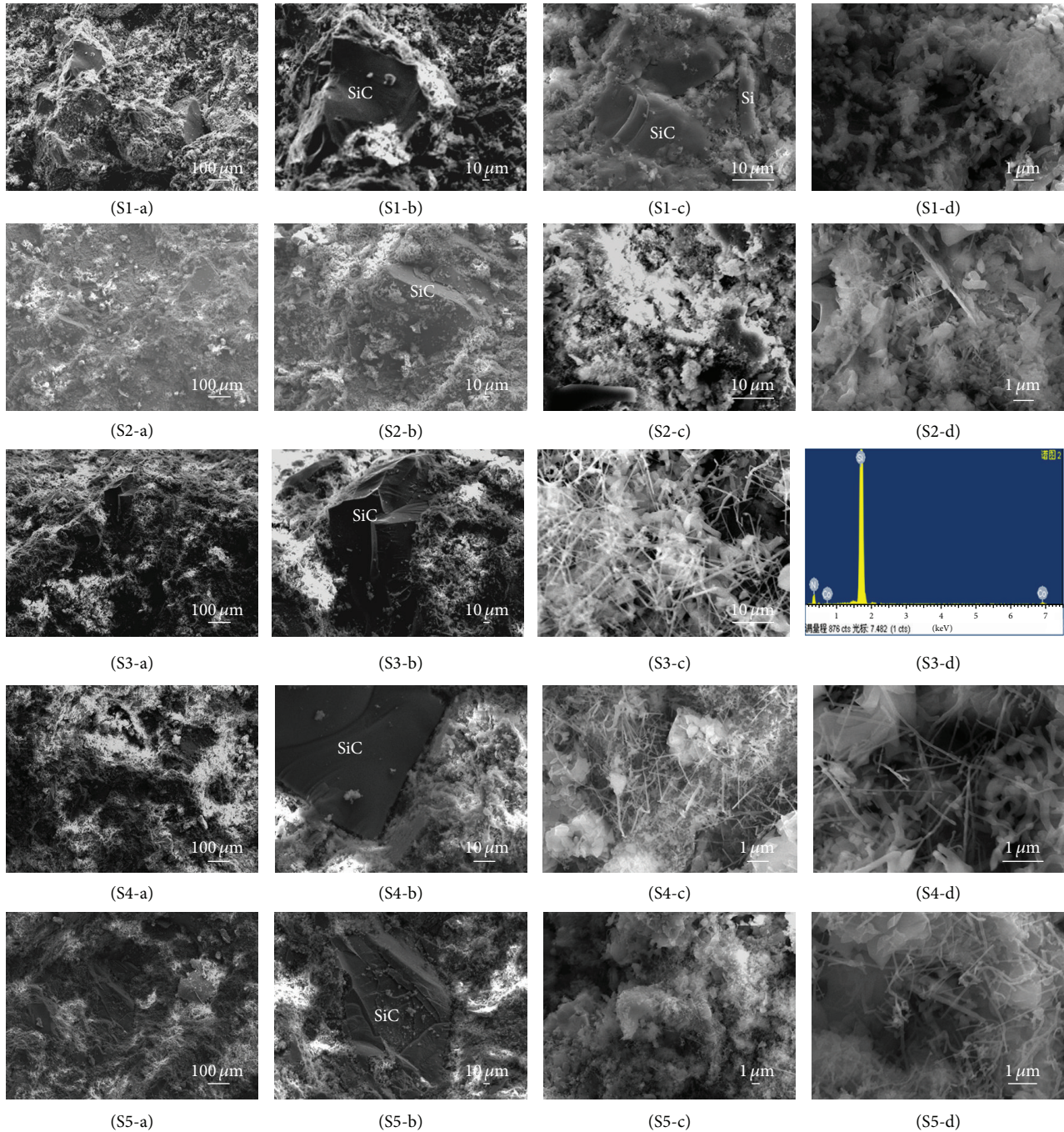


FIGURE 2: SEM images and EDS pattern of the fracture of $\text{Si}_3\text{N}_4\text{-SiC}_p$ composite refractories with various contents of Co nitrided at 1400°C .

it disappeared in the sample with Co added. And when the temperature was increased to 1450°C , the Si powders were fully nitrided. Figure 1 shows the XRD patterns of the samples nitrided at 1400°C . The main crystalline phase was SiC, and Si was nitrided and transformed to $\alpha\text{-Si}_3\text{N}_4$ with $\beta\text{-Si}_3\text{N}_4$ as a minor phase in the products with Co, whereas some unreacted silicon remained when it was without Co.

SEM images and EDS pattern of fracture samples with various contents of Co nitrided at 1400°C are shown in

Figure 2, indicating that the $\text{Si}_3\text{N}_4\text{-SiC}_p$ composite refractories were mostly well sintered. SiC particles were closely wrapped by Si_3N_4 matrix, and some regions had a few pores. Some small dense particles with relatively smooth fracture surface were seen in the products without Co. They must be silicon particles (Figure 2(S1-c)), identified by the EDS (not shown here) along with the XRD result (Figure 1). It is well known that the nitridation of silicon particles proceeded from the surface to the centre, *via* [N] diffusion. In the case

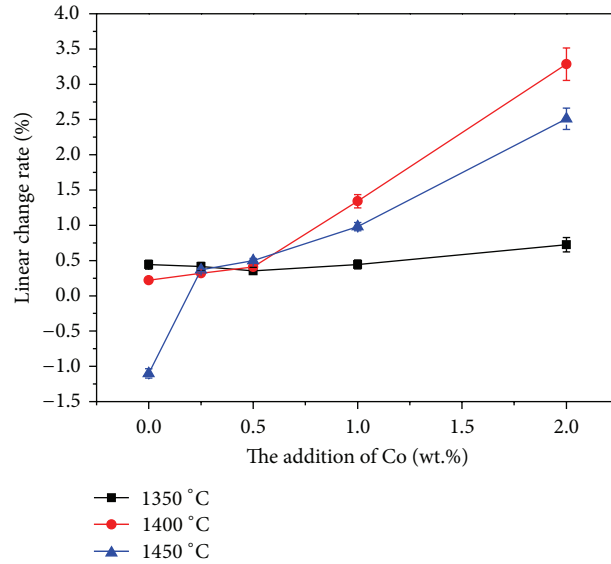


FIGURE 3: Linear change rates of $\text{Si}_3\text{N}_4\text{-SiC}_p$ composite refractories with various contents of Co nitrided at different temperatures.

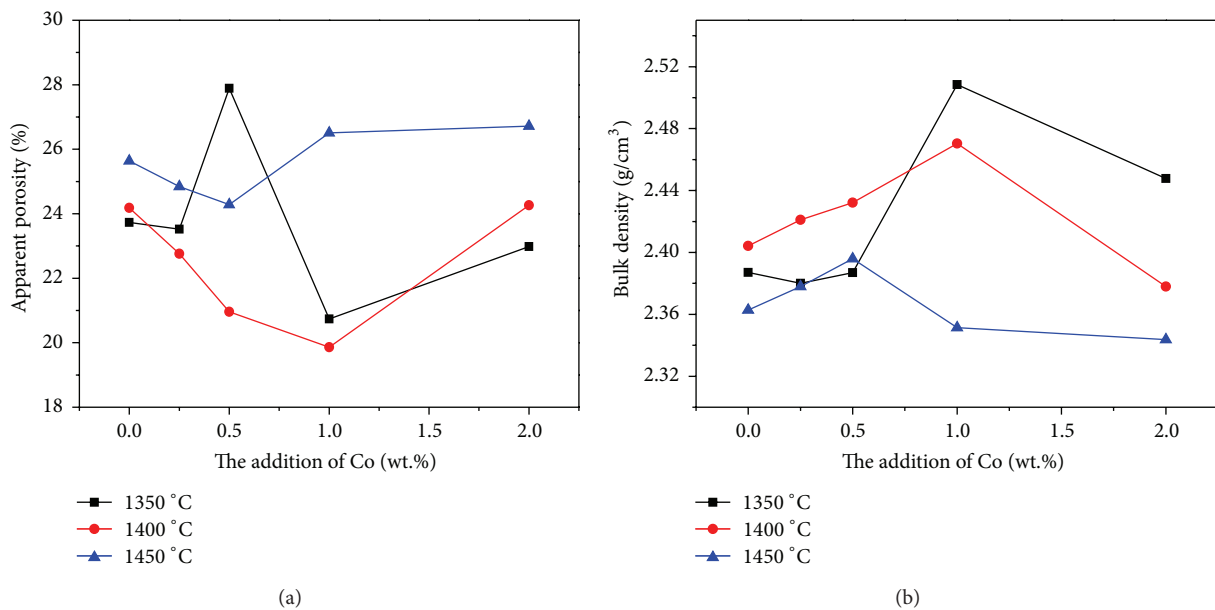


FIGURE 4: (a) Apparent porosity and (b) bulk density of $\text{Si}_3\text{N}_4\text{-SiC}_p$ composite refractories with various contents of Co nitrided at different temperatures.

of no Co, the “black” phenomenon could still appear in the product. When adding Co, the Si was fully nitrided in the product, and the quantity of nanofibers was enhanced. Those nanofibers exhibited network connection, which could improve strength of samples. EDS analysis (Figure 2(S3-d)) reveals that those nanofibers were composed of Si_3N_4 phase, containing a small amount of Co. The formation of as-formed Si_3N_4 nanofibers was through well-established VLS mechanism [26, 27].

3.2. Physicochemical Properties of As-Prepared $\text{Si}_3\text{N}_4\text{-SiC}_p$ Composite Refractories.

The linear change rates of $\text{Si}_3\text{N}_4\text{-SiC}_p$

composite refractories nitrided at different temperatures are shown in Figure 3. After nitridation at 1350°C, linear change rate of the samples was almost 0.5%, revealing that slight expansion occurred during the nitridation process. At 1400°C, the linear change rate was 0.25% in the case of Co absent and slightly increased but also less than 0.5% in the case of adding Co (≤ 0.5 wt.%), whereas it continued to increase when Co was higher than 1.0%. After nitriding at 1450°C, the linear change rate of the sample without Co was -1.1% , implying the sample being shrunk. It should be due to the increasing of temperature so that the external force required for the sintering process was improved, which

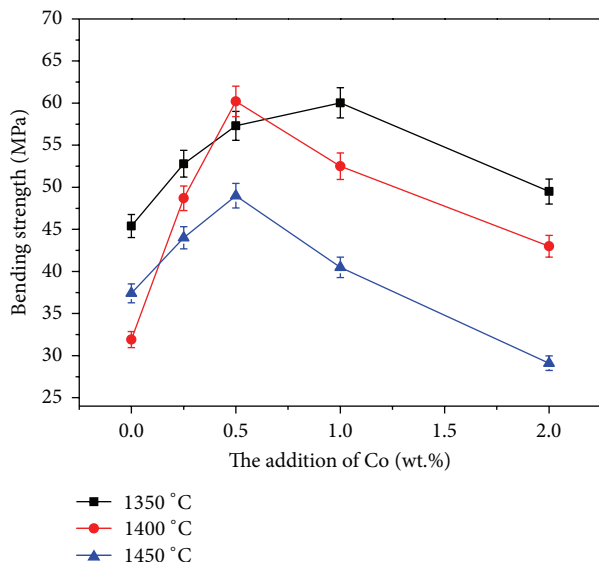


FIGURE 5: The bending strength of $\text{Si}_3\text{N}_4\text{-SiC}_p$ composite refractories with various contents of Co nitrided at different temperatures.

promoted the migration of solid-gas interface in the samples during the sintering process and the removal of the more pores. However, the expansion formed after fully nitridation of silicon was not enough to offset the shrinkage from the removal of the pores, resulting in the final shrinkage of samples. The samples with Co at this high temperature had a bit of expansion. When the Co was ≤ 0.5 wt.%, the linear change rate of the samples was maintained at 0.5%, whereas it was increased with Co > 0.5 wt.%.

The apparent porosity and bulk density of $\text{Si}_3\text{N}_4\text{-SiC}_p$ composite refractories nitrided at different temperatures are shown in Figure 4. After nitriding at 1350°C , the apparent porosity of sample without Co was 23.7%, which was larger than those with Co. At 1400°C , the sample without Co had a large apparent porosity of 25.3%, and it was initially decreased and subsequently increased with the increase of Co. It reached at the smallest value (19.8%) when the content of Co was 1%. When the nitriding temperature was elevated to 1450°C , it was reduced to 24.8% in the sample without Co, and its change trend in the samples with Co was the same as that at 1400°C . The bulk density of the samples under different conditions had an opposite trend, compared to the apparent porosity. As can be seen from the results, the sample with Co content of 0.5 wt.%–1.0 wt.% had the minimum apparent porosity and maximum bulk density.

3.3. Bending Strength of As-Prepared $\text{Si}_3\text{N}_4\text{-SiC}_p$ Composite Refractories. The bending strength of $\text{Si}_3\text{N}_4\text{-SiC}_p$ composite refractories with various contents of Co at different temperatures is shown in Figure 5, indicating that it was initially increased and subsequently decreased with the increasing of Co. At 1350°C , it was 45.4 MPa in the case of without Co and reached the highest strength when 1.0 wt.% Co content was added and then decreased with the increasing of Co content. At 1400°C , it had been reduced to 31.9 MPa when

it was without Co, lower than that at 1350°C . It should be relative to the increased apparent porosity rate at 1400°C . As the Co content was 0.5%, the highest strength of 60.2 MPa was achieved. Although the variation tendency at 1450°C was similar to 1400°C , the bending strength of samples became lower. The initially improved strength with the increasing of Co content should be attributed to the increasing content of nanofibers. However, when the Co exceeded a certain amount, the overmuch nanofibers lead to an expansion of the samples, and an evaporation of Si facilitated by the formation of Co-Si liquid phase resulted in an increase in porosity. As is well known, the quantity, shape, size, and distribution of pores generated during the sintering process have a significant impact on the fracture strength of materials. The strength-porosity dependence can be approximated by the following exponential equation [28]:

$$\sigma = \sigma_0 \cdot \exp(-np), \quad (1)$$

where σ_0 is the strength of a nonporous structure, σ is the strength of the porous structure at a porosity p , and n is a constant. Generally, the bending strength of inorganic nonmetallic materials decreases with the increase of the porosity. In this work, the strength-porosity relationship of the sintering samples could comply with it. Based on the results, we concluded that it was necessary to add catalyst for enhancing nitridation of silicon, facilitating the sintering as well as improving the strength of $\text{Si}_3\text{N}_4\text{-SiC}_p$ composite refractories. Herein, the Co content of 0.5% and the temperature of 1400°C were the optimal experimental conditions.

4. Conclusions

In this research, we produced *in situ* Cocatalytic nitrided $\text{Si}_3\text{N}_4\text{-SiC}_p$ composite refractories at a relatively low sintering temperature using Si and SiC_p as raw materials. The cobalt facilitated the nitridation of Si to form Si_3N_4 grain and nanofibers. At 1350°C and 1400°C , the sample without Co still had unreacted Si, whereas the samples with Co were fully nitrided. With the increase of Co addition (from 0 wt% to 2.0 wt%), the liner change rate of as-prepared refractories was increased, and their apparent porosity was initially decreased and subsequently increased, while the bulk density and the bending strength exhibited an opposite trend. The as-prepared $\text{Si}_3\text{N}_4\text{-SiC}_p$ composite refractories had the highest strength of 60.2 MPa when the Co content was 0.5 wt.%. The addition Co accelerated the formation of Si_3N_4 nanofibers exhibiting network connection and promoted the sintering of $\text{Si}_3\text{N}_4\text{-SiC}_p$ composite refractories, thus improving their strength.

Conflict of Interests

The authors declare that there is no conflict of interests regarding the publication of this paper.

Acknowledgment

This work was financially supported by National Natural Science Foundation of China (Grant no. 51032007).

References

- [1] Z. H. Huang, W. Pan, L. H. Qi, and H. Z. Miao, "Erosive wear behavior of reaction sintered Si_3N_4 - SiC_p composite ceramic in liquid-solid flow," *Key Engineering Materials*, vol. 280–283, pp. 1317–1318, 2005.
- [2] Z. Yi, Z. Xie, J. Ma, Y. Huang, and Y. Cheng, "Study on gelcasting of silicon nitride-bonded silicon carbide refractories," *Materials Letters*, vol. 56, no. 6, pp. 895–900, 2002.
- [3] A. A. Nourbakhsh, F. Golestani-Fard, and H. R. Rezaie, "Influence of additives on microstructural changes in nitride bonded SiC refractories," *Journal of the European Ceramic Society*, vol. 26, no. 9, pp. 1737–1741, 2006.
- [4] D. C. Loriz and T. R. Holmes, "Development and properties of silicon carbide refractories for blast furnace use," in *Applications of Refractories: Ceramic Engineering and Science Proceedings*, vol. 7 of no. 1-2, chapter 9, Wiley, 2008.
- [5] I.-W. Chen and A. Rosenflanz, "A tough SiAlON ceramic based on α - Si_3N_4 with a whisker-like microstructure," *Nature*, vol. 389, no. 6652, pp. 701–704, 1997.
- [6] Z. Shen, Z. Zhao, H. Peng, and M. Nygren, "Formation of tough interlocking microstructures in silicon nitride ceramics by dynamic ripening," *Nature*, vol. 417, no. 6886, pp. 266–269, 2002.
- [7] J. Huang, H. Zhou, Z. Huang, G. Liu, M. Fang, and Y. Liu, "Preparation and formation mechanism of elongated (Ca, Dy)- α -Sialon powder via carbothermal reduction and nitridation," *Journal of the American Ceramic Society*, vol. 95, no. 6, pp. 1871–1877, 2012.
- [8] J. Z. Yang, Z. H. Huang, M. H. Fang, Y. G. Liu, J. T. Huang, and J. H. Hu, "Preparation and mechanical properties of Fe/Mo-Sialon ceramic composites," *Scripta Materialia*, vol. 61, no. 6, pp. 632–635, 2009.
- [9] J. Huang, H. Zhou, Z. Huang, G. Liu, M. Fang, and Y. Liu, "Effect of Y- α -Sialon seeding and holding time on the formation of elongated Ca-Dy- α -Sialon prepared via carbothermal reduction and nitridation," *Journal of the American Ceramic Society*, vol. 95, no. 5, pp. 2777–2781, 2012.
- [10] K. H. Jack, "Sialons and related nitrogen ceramics," *Journal of Materials Science*, vol. 11, no. 6, pp. 1135–1158, 1976.
- [11] Z. H. Huang, J. T. Huang, M. H. Fang et al., "The effects of SiC_p addition on the z-value and mechanical properties of α -Sialon- SiC_p refractories," *Journal of the Ceramic Society of Japan*, vol. 120, no. 10, pp. 1–6, 2012.
- [12] L. Fa, Z. Dongmei, Z. Hua, and Z. Wancheng, "Properties of reaction-bonded SiC/ Si_3N_4 ceramics," *Materials Science and Engineering A*, vol. 431, no. 1-2, pp. 285–289, 2006.
- [13] A. K. Gain, J. Han, H. Jang, and B. Lee, "Fabrication of continuously porous SiC- Si_3N_4 composite using SiC powder by extrusion process," *Journal of the European Ceramic Society*, vol. 26, no. 13, pp. 2467–2473, 2006.
- [14] J. T. Huang, Z. H. Huang, Y. G. Liu et al., " β -Sialon nanowires, nanobelts and hierarchical nanostructures: morphology control, growth mechanism and cathodoluminescence properties," *Nanoscale*, vol. 6, pp. 424–432, 2014.
- [15] J. T. Huang, Y. G. Liu, Z. H. Huang et al., " $\text{Ni}(\text{NO}_3)_2$ -assisted catalytic synthesis and photoluminescence property of ultra-long single crystal Sialon nanobelts," *Crystal Growth and Design*, vol. 13, no. 1, pp. 10–14, 2013.
- [16] J. T. Huang, S. W. Zhang, Z. H. Huang et al., "Catalyst-assisted synthesis and growth mechanism of ultra-long single crystal α - Si_3N_4 nanobelts with strong violet-blue luminescent properties," *CrystEngComm*, vol. 14, no. 21, pp. 7301–7305, 2012.
- [17] Q. Fu, B. Jia, H. Li, K. Li, and Y. Chu, "SiC nanowires reinforced MAS joint of SiC coated carbon/carbon composites to LAS glass ceramics," *Materials Science and Engineering A*, vol. 532, pp. 255–259, 2012.
- [18] H. Kiyono, Y. Miyake, Y. Nihei, T. Tumura, and S. Shimada, "Fabrication of Si_3N_4 -based composite containing needle-like TiN synthesized using NH_3 nitridation of TiO_2 nanofiber," *Journal of the European Ceramic Society*, vol. 32, no. 7, pp. 1413–1417, 2012.
- [19] A. K. Kothari, S. Hu, Z. Xia, E. Konca, and B. W. Sheldon, "Enhanced fracture toughness in carbon-nanotube-reinforced amorphous silicon nitride nanocomposite coatings," *Acta Materialia*, vol. 60, no. 8, pp. 3333–3339, 2012.
- [20] A. J. Rodriguez, M. E. Guzman, C. Lim, and B. Minaie, "Mechanical properties of carbon nanofiber/fiber-reinforced hierarchical polymer composites manufactured with multi-scale-reinforcement fabrics," *Carbon*, vol. 49, no. 3, pp. 937–948, 2011.
- [21] J. Dusza, G. Blugan, J. Morgiel et al., "Hot pressed and spark plasma sintered zirconia/carbon nanofiber composites," *Journal of the European Ceramic Society*, vol. 29, no. 15, pp. 3177–3184, 2009.
- [22] J. Lee, D. Choi, C. Kim, S. Lee, and S. Choi, "Growth of silicon carbide nanowires on porous silicon carbide ceramics by a carbothermal reduction process," *Journal of Ceramic Processing Research*, vol. 8, no. 2, pp. 87–90, 2007.
- [23] X. H. Zhang, J. X. Gao, C. Q. Hong, J. C. Han, and W. B. Han, "Observation of SiC nanodots and nanowires in situ growth in SiOC ceramics," *CrystEngComm*, vol. 15, pp. 7803–7807, 2013.
- [24] S. Zhu, H. Xi, Q. Li, and R. Wang, "In situ growth of β -SiC nanowires in porous SiC ceramics," *Journal of the American Ceramic Society*, vol. 88, no. 9, pp. 2619–2621, 2005.
- [25] J. T. Huang, S. W. Zhang, Z. H. Huang, M. H. Fang, Y. G. Liu, and K. Chen, "Co-catalyzed nitridation of silicon and in-situ growth of α - Si_3N_4 nanorods," *Ceramic International*, 2014.
- [26] J. T. Huang, Z. H. Huang, S. Yi, Y. G. Liu, M. H. Fang, and S. W. Zhang, "Fe-catalyzed growth of one-dimensional α - Si_3N_4 nanostructures and their cathodoluminescence properties," *Scientific Reports*, vol. 3, article 3504.
- [27] S. Huang, Z. Huang, M. Fang, Y. Liu, J. Huang, and J. Yang, "Nd-sialon microcrystals with an orthogonal array," *Crystal Growth and Design*, vol. 10, no. 6, pp. 2439–2442, 2010.
- [28] K. Ishizaki, S. Komarneni, and M. Nanko, *Porous Materials: Process Technology and Applications*, Kluwer Academic Publishers, Dordrecht, The Netherlands, 1998.